3-21-2013

Novel Test Fixture for Characterizing Microcontacts: Performance and Reliability

Benjamin F. Toler

Follow this and additional works at: https://scholar.afit.edu/etd

Part of the Electronic Devices and Semiconductor Manufacturing Commons

**NOVEL TEST FIXTURE FOR CHARACTERIZING MICROCONTACTS:
PERFORMANCE AND RELIABILITY**

THESIS

Benjamin F. Toler, First Lieutenant, USAF

AFIT-ENG-13-M-47

**DEPARTMENT OF THE AIR FORCE
AIR UNIVERSITY**

AIR FORCE INSTITUTE OF TECHNOLOGY

Wright-Patterson Air Force Base, Ohio

AFIT-ENG-13-M-47

**NOVEL TEST FIXTURE FOR CHARACTERIZING MICROCONTACTS:
PERFORMANCE AND RELIABILITY**

THESIS

Presented to the Faculty

Department of Electrical Engineering

Graduate School of Engineering and Management

Air Force Institute of Technology

Air University

Air Education and Training Command

In Partial Fulfillment of the Requirements for the

Degree of Master of Science in Electrical Engineering

Benjamin F. Toler, BS and BSEE

First Lieutenant, USAF

March 2013

**DISTRUBUTION STATEMENT A.
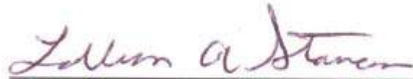APPROVED FOR PUBLIC RELEASE; DISTRIBUTION UNLIMITED**

NOVEL TEST FIXTURE FOR CHARACTERIZING MICROCONTACTS:
PERFORMANCE AND RELIABILITY

Benjamin F. Toler, BS and BSEE
First Lieutenant, USAF

Approved:

_____
Ronald A. Coutu, Jr., Ph.D., P.E. (Chairman)

1 Mar 13
Date

_____
Lavern A. Starman, Ph.D. (Member)

1 mar 2013
Date

_____
Derrick Langley, Capt, USAF, Ph.D. (Member)

1 Mar 2013
Date

AFIT-ENG-13-M-47

Abstract

Reliable microelectromechanical systems (MEMS) switches are critical for developing high performance radio frequency circuits like phase shifters. Engineers have attempted to improve reliability and lifecycle performance using novel micro-contact metals, unique mechanical designs and packaging. Contact resistance can evolve over the lifetime of the micro-switch by increasing until failure. Based on contact design and choice of materials, the contact resistance can stay low for an extended period of performance. This work shows the fabrication of micro-contact support structures and test fixture which allow for micro-contact testing, with an emphasis on the fixture's design to allow the determination and analysis of the appropriate failure mode. Two of these structures are designed to repeat Holm's cross bar experiment while the other is made for examining thin film development. The other effort of this investigation is the development of a micro-contact test fixture which can measure contact force and resistance directly and perform initial micro-contact characterization, and two forms of lifecycle testing for micro-contacts at rates up to 3 kHz. In this work, two different designs of micro-contact structures are fabricated and tested, with each providing advantages for studying micro-contact physics. Three functioning fixed-fixed Au micro-contact support structures with contact radii of 4, 6, and 10 µm and two functioning fixed-fixed Ag micro-contacts were tested using the µN force sensor at cycle rates up to 3 kHz. Of the five tested micro-contacts, only one remained functional after being cycled nearly 10.2 million times, at which point the closed contact resistance was 14.43Ω. This particular contact reached the -0.5 dB attenuation RF criteria for failure at 5.6 million cycles. The change in resistance of the micro-contact over 10.2 million cycles indicates the possibility of the development of a frictional polymer.

iv

Acknowledgments

Benjamin F. Toler

Table of Contents

List of Figures

4

7

List of Tables

NOVEL TEST FIXTURE FOR CHARACTERIZING MICROCONTACTS: PERFORMANCE AND RELIABILITY

I. Introduction

1.1 Micro-Contact Properties and Operation

Low current micro-electrical contacts have a range of existing and potential applications. The MEMS application is normally exhibited in what is referred to as a MEMS relay or MEMS switch, where a low force actuator is used to switch the micro-contact surfaces. In this research, the goal is to focus on low power applications with both dc and ac signals. A particular emphasis is provided on the application to Megahertz and Gigahertz, radio frequency systems. Radio frequency microelectromechanical system (RF MEMS) switches can be used in mobile phones and other communication devices [1]. Often, micro-switches are used in phase shifters and impedance tuners and filters. Phase shifters, impedance tuners, and filters are control circuits found in many communication, radar and measurement systems [2]. MEMS switches offer lower power consumption, better isolation, and lower insertion loss compared to conventional field-effect transistor and PIN diode switches, however, with lifetimes near 10^7 actuations, MEMS switch reliability is a major area for improvement for large-volume commercial applications [3]. The integrated circuit community is struggling to develop the future generations of ultralow-power digital integrated circuits and is beginning to examine micro switches [4].   Low power consumption, isolation, and reduced insertion loss are achieved by the mechanical actuation of the switch which physically opens or closes the circuit.

1.2 Problem Statement

To enhance reliability, circuit designers need simple and accurate behavioral models of embedded switches in CAD tools to enable system-level simulations [5]. The most common method for studying the reliability and performance of micro-contacts is to use electrostatically actuated micro-contacts and cycle them at high rates (in kHz range) until failure. Considering the average number of cycles required for a micro-contact to reach failure can be beyond 10^7 cycles, the high cycle rate is a necessity for obtaining any sort of useful failure mode information from a micro-contact within a reasonable time frame [6]. A tradeoff to this method is the use of electrostatic actuation. When using electrostatic actuation to open and close the micro-contact, the contact force must be then calculated based on the properties of the micro-contact and the applied actuation voltage. Applied micro-contact force is a key requirement for the determination of the effective contact area as well as a potential influence on the development of a failure mode. As a result of using electrostatic actuation, there is a variance in the applied contact force which makes the investigation into influence of contact force on failure modes difficult.

To examine the nature of contact force on the performance and reliability of micro-contacts, researchers have employed the use of a modified Atomic Force Microscope (AFM) micro-contact testing rate of ~0.5 Hz in order to apply a known contact force [7]. Again considering the potential lifetime of a micro-contact being greater than 10^7 cycles, the modified AFM setup could require, if running continuously, in excess of 230 days for a micro-contact to reach failure [6]. There is a need for micro-contact characterization system which can apply a known contact force and permit further study into the performance and reliability of micro-contacts.

11

1.3 Motivation

Motivation for this research comes from the need to enhance a fundamental component of many RF systems which are used in defense technologies. The research presented in this work focuses on the fabrication and development of a micro-contact test fixture and micro-contact support structures. The test fixture and micro-contact support structures enable lifecycle testing of micro-contacts for the study of micro-contact reliability as well as the underlying physics of micro-contact failure modes. By characterizing the physics of micro-contact failure modes, engineers will be able to advance technologies using micro-contacts and integrate them into new advanced systems.

1.4 Micro-Contact Test Fixture Solution

The efforts of this research focused on developing a micro-contact test fixture capable of lifecycle testing as well as the fabrication and testing of micro-contact structures. First, the types of failure modes micro-contacts experience were investigated in order to determine the types of lifecycle testing required by the micro-contact test fixture. Research was then performed to make the appropriate micro-contact test fixture. The micro-contact test fixture was fabricated and the automation software programmed. Studies to verify micro-contact test requirements were performed.

1.5 Micro-Contact Support Structure Solution

As mentioned previously, this research focused on the design, fabrication, and testing of micro-contact structures. First, research into the types of failures micro-contacts experience has been performed. This research was used to develop a micro-contact structure suitable for diagnosing the micro-contact failures after lifecycle testing. The data gathered

on the properties of the materials was used and calculations were performed to determine the appropriate thickness of the layers needed. Analytical methods were used to characterize the behavior and physical phenomena of the micro-contact structures. The designed micro-contact structure was then fabricated and tested using the micro-contact test fixture.

1.6 Summary

Accurate predictors for the lifetime performance of micro-contacts are needed by engineers to enhance future technology. In order to develop accurate predictors, micro-contact physics and phenomena must be studied over the micro-contact's lifecycle. Proper characterization of the experienced failure mode by the micro-contact is vital to determine if material properties or environmental factors limit the reliability of the micro-contact. An investigation was performed to determine the requirements for a micro-contact structure suitable for the study of micro-contact physics and a micro-contact test fixture capable of lifecycle testing of micro-contact structures. The next section of this document provides a review on the relevant micro-contact knowledge areas, these include, design, resistance modeling, contact materials, performance and reliability.

II. Literature Review

2.1 Chapter Overview

A review of electrostatically actuated, low current, micro-contacts is presented. Innovations in relevant micro-contact areas are highlighted, these include, design, resistance modeling, contact materials, performance and reliability. For each area the basic theory and relevant innovations are explored. A brief comparison of actuation methods is provided to show why electrostatic actuation is most commonly used for designers. An examination of the important characteristics of the contact interface such as modeling and material choice is discussed. Micro contact resistance models based on plastic, elastic-plastic, and elastic deformations are reviewed. Much of the modeling for contact micro-switches centers on surface roughness. Surface roughness and its effect on contact resistance is stressed when considering contact resistance modeling. Finite element models and various approaches for describing surface roughness are compared. Different materials to include gold, carbon nanotubes, composite gold-carbon nanotubes, ruthenium and ruthenium composites, as well as tungsten have been shown to enhance contact performance and reliability with distinct tradeoffs for each. Finally, a review of physical and electrical failure modes witnessed by researchers are detailed and examined.

2.2 Contact Resistance

For DC micro-switches, resistance modeling requires knowledge of the surface of the two contact materials as well as their material properties. Though contaminants can have a major impact on micro-contact resistance, they are not initially considered for the description and determination of micro-contact resistance. Holm first identifies this in his example of

contact resistance using two cylinders in contact at their bases [8]. Despite the surfaces of the cylinder bases appearing similar, they are actually very different. When two surfaces meet, and because no surface is perfectly smooth, asperity peaks or "a-spots", from each surface meet at the interface and form contact areas. Asperities have been described as "small cold welds providing the only conducting paths for the transfer of electrical current" [9]. Figure 1 shows a graphical representation of apparent contact area, contacting a-spots, and the effective radius of the actual conducting area. The effective area is used for making simplified contact resistance calculations. Holm also investigated contact resistance changes due to plastic and elastic deformation of a-spots; which greatly affects the interface of the contact areas. Resistance for the cylinders then, is simply the measured voltage between the two rods divided by the current flowing through them.
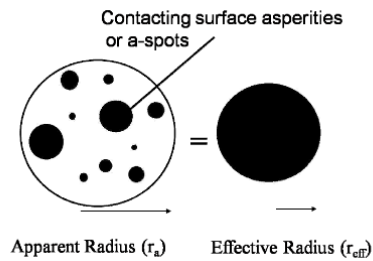
Figure 1 A-spots as an effective radius [10]

Majumder *et al.*, modeled micro-contact resistance with three steps [12]. First, determine the contact force, as a function of applied gate voltage, available from the mechanical design of the electrostatically actuated micro-switch. Second, determine the effective contact area at the interface as a function of contact force [12]. Finally, determine the contact resistance as a function of the distribution and sizes of the contact areas. Majumder *et al.*, like Holm, also noted that the surface profile of the contact interface is

sensitive to plastic and elastic deformation. He also investigated ballistic electron transport

using Sharvin's equation.

Elastic modeling is accurate for extremely low values of contact force (a few mN)

where surface asperities retain their physical forms after the contact force is removed.

Elastic-plastic deformation occurs at the boundary between the permanent plastic

deformation and the temporary elastic deformation. Under plastic deformation, permanent

surface change occurs by the displacement of atoms in asperity peaks whereas neighboring

atoms are retained under elastic deformation [13].

Asperity contact area under elastic deformation is given by [14]:

$$A = \pi R \alpha \tag{1}$$

where A is contact area, R is asperity peak radius of curvature, and α is asperity

vertical deformation. Hertz's model for effective contact area for elastic deformation as:

$$r_{eff} = \sqrt[3]{\frac{3 F_{cE} R}{4 E'}} \tag{2}$$

where E' is the Hertzian modulus derived from:

$$\frac{1}{E'} = \frac{1 - v_1^2}{E_1} + \frac{1 - v_2^2}{E_2} \tag{3}$$

with E_1 as the elastic modulus for contact one, v_1 is Poisson's ratio for contact one,

E_2 as the elastic modulus for contact two, v_2 is Poisson's ratio for contact two [12, 15].

Majumder *et al.* then related the contact area radius to contact force by:

$$F_{cE} = \frac{4}{3} E' \alpha \sqrt{R \alpha}. \tag{4}$$

To account for the asperity contact area and force under plastic deformation, the

model from Abbot and Firestone that assumes sufficiently large contact pressure and no

material creep is used [16]. Single asperity contact area and effective contact area are defined using (5) and (6) [15]:

$$A = 2\pi R\alpha \tag{5}$$

$$r_{eff} = \sqrt{\frac{F_{cP}}{H\pi}} \tag{6}$$

where H is the Meyer hardness of the softer material [15], A is contact area, R is asperity peak radius of curvature, and α is asperity vertical deformation [15]. The effective contact area radius is then related to contact force by [8]:

$$F_{cP} = HA. \tag{7}$$

While plastic and elastic definitions are helpful, a thorough description of deformation cannot be provided without considering the elastic plastic transition between the two kinds of deformation. Elastic-plastic material deformation asperity contact area is given as:

$$A = \pi R\alpha(2 - \frac{\alpha_c}{\alpha}) \tag{8}$$

where α_c is the critical vertical deformation, where elastic-plastic behavior begins [15]. Effective contact area is given by:

$$r_{eff} = \sqrt{\frac{F_{cEP}}{H\pi\left[1.062 + 0.354\left(\frac{2}{3}K_Y - 3\left(\frac{\alpha_c}{\alpha}\right)\right)\right]}} \tag{9}$$

where K_Y as the yield coefficient. Inclusion of Chang's force equation and rigorous mathematical manipulation provides the relationship between contact area and contact force [14]:

$$F_{cEP} = K_H A \qquad (10)$$

with K_H is a hardness coefficient. Equations (5), (6), and (10) provide the relationship between contact force and effective conducting area. It is important to note that contact force directly influences the effective conducting area and will also impact contact resistance by default.

For the standard test configuration, resistance can be modeled as shown in Figure 2 where R_c represents contact resistance, R_{cf} represents the resistance due to contaminate films, R_{sh} is sheet resistance, and R_{par} is the parasitic resistance from solder connections, clip leads, wires, etc [17]. This R_{sh} and R_{par} can be eliminated if the experiment is set up using a four wire cross bar configuration [8].

Figure 2 Standard test configuration resistance model [17]

Based on the effective conducting area and how it compares with the mean free path of an electron, current flow is described as ballistic, quasi-ballistic, or diffusive [10].
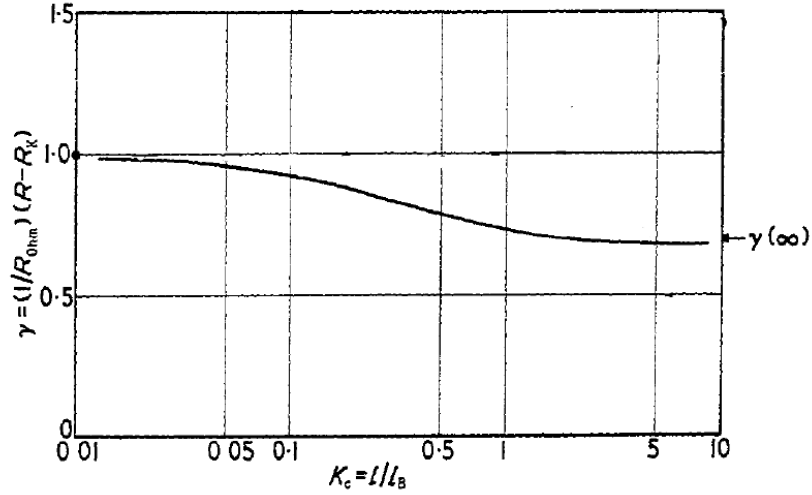
Figure 3 A Plot of Wexler's Gamma Function [18]

Previously, Wexler derived an interpolation for contact resistance between ballistic

and diffusive transport regions [15, 18]:

$$R_W = R_S + \Gamma(K)R_c \tag{11}$$

where $\Gamma(K)$ is a slowly varying Gamma function of unity order [18], R_S is the

Sharvin resistance, and R_c is the constriction resistance based on diffusive electron transport.

Figure 3 shows a plot of Wexler's Gamma function. The semi-classical approximation for

resistance when electrons exhibit ballistic transport behavior is the Sharvin resistance

formula shown as   [15].

$$R_S = \frac{4\rho K}{3\pi r_{eff}}. \tag{12}$$

Wexler's model was improved to generate a new micro-contact resistance model for

elastic deformation based on contact resistance considering elastic deformation and diffusive

electron transport as well as a contact resistance model considering elastic deformation and

ballistic electron transport, shown by (13) [10].

19

$$R_{WE} = R_{cBE} + \Gamma(K)R_{cDE} \qquad (13)$$

where R_{WE} is the Wexler resistance (using Mikrajuddin's *et al.*'s derived gamma function) for elastic material deformation [15]. In this instance, $\Gamma(K)$ is not the slowly varying Gamma function of unity order but has been replaced by Mikrajuddin *et al.*'s well behaved Gamma function describing complete diffusion:

$$\Gamma(K) \approx \frac{2}{\pi} \int_0^\infty e^{-Kx} Sinc(x)dx. \qquad (14)$$

Figure 4 shows a plot Mikrajuddin *et al.*'s derived gamma function which describes electron flow as a function of the Knudsen number K, which is calculated by the effective radius and the electron's elastic mean free path. The significance of Mikrajuddin *et al.*'s result is that it describes situations for complete diffusive electron transport or complete ballistic electron transport whereas Wexler's original derivation included all higher order effects (e.g. electron spin and electron distribution).
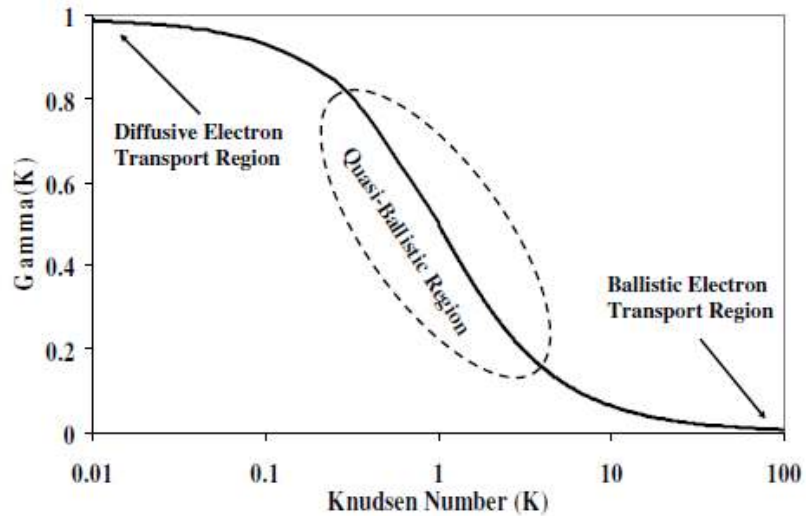
Figure 4 A plot of Mikrajuddin et al.'s derived Gamma function [10]

Continuing this work, Coutu *et al.* further developed a model for contact resistance in the plastic-elastic mode by considering the contact resistance equation based on ballistic electron transport and elastic-plastic material deformation [15] (shown in (15)) and contact resistance based on diffusive electron transport and elastic plastic material deformation (shown in (16)) [10].

$$R_{cBEP} = \frac{4\rho K}{3\pi} \sqrt{\frac{H\pi\left[1.062 + 0.354\left(\frac{2}{3}K_Y - 3\left(\frac{\alpha_c}{\alpha}\right)\right)\right]}{F_c}} \tag{15}$$

$$R_{cDEP} = \frac{\rho}{2} \sqrt{\frac{H\pi\left[1.062 + 0.354\left(\frac{2}{3}K_Y - 3\left(\frac{\alpha_c}{\alpha}\right)\right)\right]}{F_c}} \tag{16}$$

With (15) and (16) the new model for contact resistance for elastic-plastic deformation is then [10]:

$$R_{WEP} = R_{cBEP} + \Gamma(K)R_{cDEP}. \tag{17}$$

Convergence of electrical current flow lines from a distance far from the constriction and the subsequent spreading out of the current from the constriction is known as constriction resistance or commonly contact resistance [8, 19]. The spreading resistance inherently affects contact resistance. To model spreading resistance, Karmalkar *et al.* developed a simple closed-form model to predict accurate and complex calculations of circular and rectangular contact spreading resistances [20]. The method was to solve the three dimensional Laplace equation

$$\nabla^2 \psi = 0 \tag{18}$$

subject to the appropriate boundary conditions in several iterations to consider changing geometries. Holm, by contrast, represented spreading resistance as a 5% increase

in constriction resistance [8]. By interpolating the results of the different geometric solutions, the resistance average was calculated [20]. Experimental tests revealed close (within 2%) agreement with standard numerical analysis software. Their study found that the developed model accurately predicts all the trends of resistance, to include a significant variation as a function of the smaller electrode location, dependence on the electrode separation-to-width ratio, and saturation with increase in the larger electrode area for both equipotential and uniform current density boundary conditions [20].

When considering micro-contacts, surface contamination has severe negative impacts for electrical contacts by physically separating the conductive electrode surfaces [21]. Based on thickness and composition, the adsorbed contaminants can increase contact resistance by orders of magnitude [21]. When left exposed to the ambient lab air, device surfaces can be covered with various contaminants which will affect conductivity [22]. This concept was experimentally verified by Lumbantobing *et al.* where during cyclical contact loading, electrical contact resistance was erratic due to the strong dependence of contact resistance on an insulating thin film at the contact interface [23].

2.3 Micro-Contact Resistance Modeling

Timsit explored the effect of constriction resistance on thin film contacts [19]. He postulated that the spreading resistance of an asperity in a thin film will be drastically different than of an asperity in bulk material due to the different boundary conditions [19]. This convergence is visually represented in Figure 5.
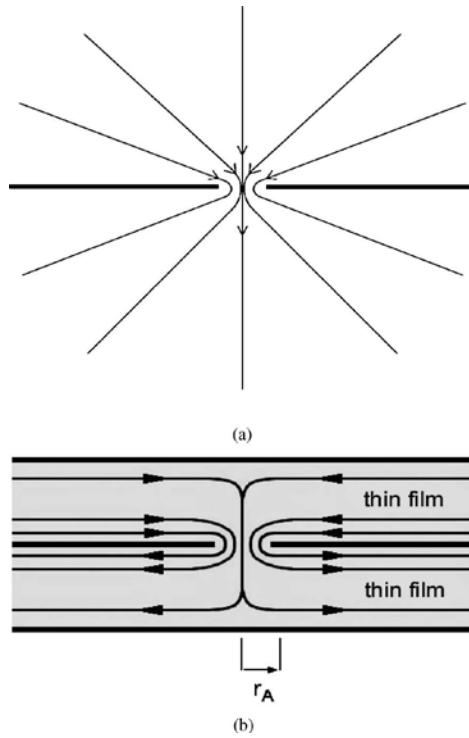
Figure 5 (a) Spreading of current streamlines in two "bulk" conductors in contact over a circular spot of radius a. (b) Spreading of current streamlines near a constriction between two thin films. [19]

His study revealed that the contact resistance for a contact with two identical films can be immediately calculated as twice the spreading resistance [19]. Also, the constriction resistance between two films of the same thickness L in contact over a constriction of radius a deviates greatly from the classical expression $p/2a$ for two contacting bulk solids wherever $a/L \geq 0.02$ [19]. A counter-intuitive discovery was shown revealing that spreading resistance in a radially-conducting film initially decreases with decreasing film thickness [19]. This is counter-intuitive because the resistance of a solid conductor increases with decreasing thickness [19]. Lumbantobing *et al.* experienced reduced electrical contact resistance on a contact with a native oxide during cyclic contact loading and attributed the reduced resistance to the local rupture of the film, resulting in asperity nanocontacts that reduced the resistance [23]. They also found that the nearly uniform thickness of the native

oxide film predicted in their experiment illustrated the durability and robustness of oxide thin film under the tested loading conditions.

To examine contact resistance models based on thin films, Sawada *et al.* performed a current density analysis of thin film effects in the contact area on a light emitting diode (LED) wafer [24]. By using a unique setup using an indium bump to mate with a gallium phosphorous wafer, the team was able to examine and image current flow through the contact. Imaging was possible because the current flow was causing optical emission in the wafer. The images and results showed that the current flow in the contact was located primarily around the perimeter of the contact. The use of imaging enabled greater insight in determining actual micro-contact area. The research showed that classical theory for contact resistance was sufficient provided the conducting film was sufficiently thick (200µm) [24]. In comparison with Timsit's model for the constriction resistance of thin films, the results were in agreement. However, if the film thickness is 50µm or less, the value of the contact resistance is greater than the bounds of the classical theory.

Timsit's results are very similar to those published by Norberg *et al.* whereby contact resistance in thin films was approximated by empirical modifications of Holm's classical relation:

$$R_s = \frac{\rho}{2a} \tag{19}$$

where ρ is the resistivity of the conducting material and a is the radius of the constriction [8, 25]. However, Norberg *et al.* approximated constriction resistance for more complex geometries and the effects of bulk resistance being isolated from constriction resistance [19].

Timsit also examined the major electrical conduction mechanisms through small constrictions and concluded that the onset of the Sharvin resistance, which stems from ballistic electronic motion in a constriction, eventually invalidates the basic assumptions of classical electrical contact theory [26]. He reported through the use of a simple a-spot model and quantum mechanics that the cooling of a small a-spot due to heat loss by the surrounding electrically-insulating films is not sufficiently large enough to have an impact or account for the breakdown of classical theory. The conjecture is proposed that for metal atomic scale constrictions, a single atom corresponds to a single conductance channel which implies that the conductance would not decrease smoothly as the mechanical contact load is decreased [26]. Rather, the conductance will drop in well-defined steps since the number of contacting atoms is decreased by discrete units of one or a few at a time [26, 27]. The thin film work of Timsit, Norberg, and Sawada provide necessary insight for future micro-contacts study since the thin films studied are on the same order as films routinely used to fabricate MEMS switches.

Assumptions about asperity size and quantity greatly impact contact resistance calculations. While most contact resistance models consider only single "small" constrictions, the typical rough surface may include many small contacts of varying sizes. However, quantum effects may be present with sufficiently small contacts. To investigate the quantum and size dependent contact mechanisms of the asperity sizes on typical surfaces, Jackson *et al.* examined the effect of scale dependent mechanical and electrical properties on electrical contact resistance between rough surfaces [28]. Beginning with classical contact mechanics, they used established multi-scale models for perfectly elastic and elastic-plastic contacts for the purpose of predicting electrical contact resistance between surfaces with

multiple scales of roughness. They then examined scale dependent strength of the materials tin and gold and found that the yield strength varies by over two orders of magnitude as the contact diameter changes. Lastly, using an iterative multi-scale sinusoidal method to calculate the average radius of a contact at given scales, an analytical model of electrical contact resistance was developed.

Poulain *et al.* examined quantized conductance with micro-contacts by breaking contact in such a way that the dimensions of the conducting members of the micro-contact were much smaller than the mean free path of the electron [29]. The team found that by using a micro-switch and a nanoindentor, they were able to witness quantized conductance plateaus before separation of the two contact members. The conditions for observing the quantized conduction phenomena are a switch opening at an extremely low speed and a current limitation near 150μA [29]. Upper and lower micro-contacts made of Au/Au as well as micro-contacts made of Ru/Ru were tested. Independent of the contact material, the quantized conductance behavior was witnessed. The plateaus were consistent with theoretical predictions for quantum ballistic transport in atomic-sized contacts. The work showed that the metallic bridge formed during contact separation, in the last stage of break, consists of only a few atoms and is similar to a nanowire or waveguide that reveals the wave character of the electrons [29]. The team observed that reproducibility of the results is difficult due to the fact that the elongation of the atomic-sized bridge is difficult to control and is strongly related to atomic arrangements [29].

While dealing with the quantum theory to describe current flow through nano scale asperities is being explored, some researchers are developing methods to simulate electrical contact resistance of ohmic switches with Finite Element Modeling (FEM). Pennec *et al.*

26

examined the impact of surface roughness on the electrical contact resistance under low actuation forces (from a few tens of micronewtons to 10mN) [30]. An important aspect of their work was to clearly define the surface roughness of the contact. Common practice is to take the average radius of curvature of the asperities which is determined by a measurement of the surface profile [31]. The drawback to this common method is that the determination of the average radius is subjective to the scale of the observation, and is also limited by the measurement resolution [32, 33, 34]. In order to clearly define the surface roughness of the contact, three methods were examined: statistical, fractal, and deterministic [30]. A statistical approach is based on a stochastic analysis which can be limited to the resolution of the measuring instrument [30]. A fractal method, on the other hand, random surface texture is characterized by scale-independent fractal parameters [30].

The deterministic approach was chosen due to its closest representation of the actual surface [30, 35]. Deterministic methods capture discrete data points for real heights on the surface which avoids assumptions of the micro geometry of the a-spots [30]. Kogut states that even though there are several methods to model contacting rough surfaces, the most convenient one is the probabilistic approach [35]. This approach replaces the two rough surfaces by a smooth surface in contact with an equivalent rough surface, replacing asperities with simple geometric shapes, and assuming a probability distribution for the asperity parameters [36]. The probabilistic model was developed by Greenwood and Williamson and was developed for elastic contacts [11].
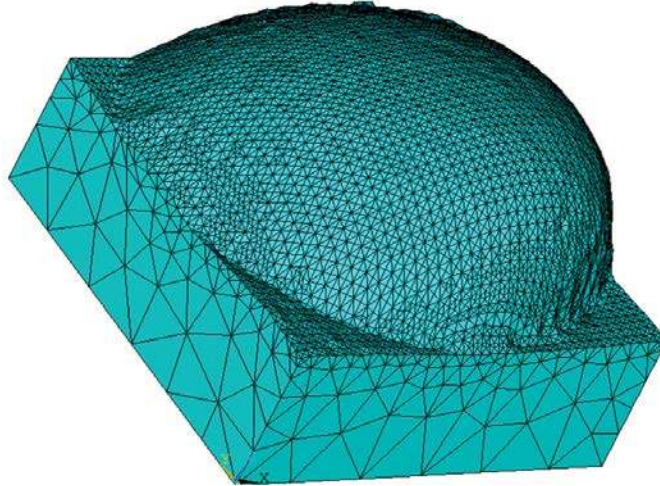
Figure 6 Geometry of finite element mesh in rough contact bump [30]

As shown in Figure 6, using an AFM, the team was able to capture 3-D data points of contact bumps and apply a low resolution mesh in order to quickly determine the effective contact area under 100μN of force [30]. By stepping up the resolution for the effective contact area to the effective computation memory limits, Pennec *et al.* were able to model a contact resistance in agreement with literature [30]. While their method did not take into account contaminant films, the results show that including the fine-scale details of the surface roughness must be taken into account when calculating contact resistance [30]. However, while AFM's can achieve 1nm resolution of surfaces, the number of contact elements and definition of elastic-plastic materials in the model can prevent the calculations from succeeding due to computer memory limitations [30]. Conclusive evidence is given that reducing the sampling interval from 1nm to 10nm is sufficient for the calculation of electrical contact resistance.

Proponents of fractal models, Rezvanian *et al.* believe that the random and multiscale nature of the surface roughness can be better described by fractal geometry [12, 37]. Fractal based models have been developed by a number of researchers but lack considerations for

28

elasticity [38, 39]. Persson *et al.* developed a novel fractal method which is not dependent on fractal roughness and is not scale dependent like the Greenwood model [40, 41]. The disadvantage is that this method is exclusive to fractal surfaces [42].

Similar in nature, Jackson *et al.* considered multi-scale roughness, or the description of the surface, to be sinusoids stacked into layers to represent the rough surface [43]. While quantitative discrepancies exist between the statistical methods and layered sinusoids, the team was able to show qualitative similarities for both elastic and elastic-plastic deformation [43]. In fact, until higher force loads are reached, the model is very much in agreement with standard methods [43]. At higher loads where the contact radius is large compared to the asperity tip radius, the models differ greatly [43]. This method of stacking sinusoids however is not limited to contact resistance but is also employed to model adhesion [44]. Where the classical approximation for area is a simplified model that typically bundles asperities into a few, the stacked sinusoids allow for a more practical representation of a multiscale surface [44].

So far, it is apparent that the surface of the physically connecting electrodes is a key factor for the determination of electrical contact resistance. Modifications to the surface via a thin film from adsorbed contaminants from either ambient air or hermetic environments will greatly decrease the conductivity of the contact. To improve electrical conduction between contacts, Jackson *et al.* have tried to reduce the contact resistance by applying an anisotropic conductive thin film [45]. These films are typically an epoxy that is doped with conductive metal particles [45]. While classical electrical resistance theory falls short for accurately predicting the contact resistance with an insulating thin film, a model is proposed by Jackson and Kogut to consider elastic-plastic behavior of the thin film and large

deformations of the conductive particles [45]. While previous anisotropic conductive film models have under predicted electrical contact resistance, a conjecture is made that the difference may be accounted for by the quantum effect of electron tunneling that takes place through the energy barrier imposed by the thin film [45]. This "tunneling" resistance is higher than the constriction resistance [45]. Using empirical models, mechanical and electrical material constants were held constant and the radius of the conductive particles in the film were varied [45]. The results revealed that particle size influenced contact resistance and that the larger radius provided a lower resistance [45].

When it comes to contact resistance modeling, contact material deformation and the effective contact area radius are the two primary considerations [10]. An assumption that individual a-spots are sufficiently close and that a single effective area model is typically made to determine specific electron transport regions by comparing the effective radius and mean free path of an electron [10]. As seen by area models to characterize the surface topology, describing the appropriate effective area for modeling is difficult. From the modeling of the surface using statistical, deterministic, or fractal means to the models of contact resistance based on all the deformation modes, the development of a thin film will widen the variance between simulated and actual results. Contact materials also have an integral role in determining the performance and reliability of micro-switches. Hardness as well as conductivity and other material properties influence the contact resistance. Gold, palladium, and platinum are commonly used [46]. Due to the fact that these materials are very soft and wear easily, other materials such as ruthenium and combination materials have been examined for their effectiveness at lengthening the lifecycle and the performance of the

30

contact. For example, materials such as Au, Ru, Rh, Ni, were compared in mixed

configurations to try and increase reliability [47].

2.4 Beam Modeling

2.4.1 Fixed-Fixed Beam Micro-Contact Support Structure
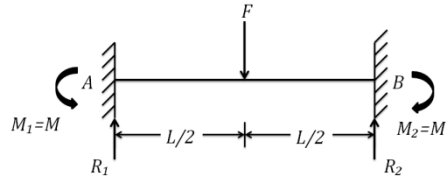
Figure 7 Fixed-Fixed Beam Moment Diagram

In order to determine the force required to make contact using the fixed-fixed beam

micro-contact support structure, the micro-contact support structure is modeled as a simple

fixed-end beam with a concentrated load F at the midpoint. Figure 7 shows the simplified

beam's moment diagram. Because of beam symmetry and the applied load F in the vertical

direction, the moments on either end of the beam are equivalent and lead to:

$$M = \frac{Fx}{2} - M_1 \quad (0 \le x \le \frac{L}{2}).$$

(20)

Mohr's theorems provide the relationship between the moment M, Young's modulus E,

inertia I, and rate of change for deflection δ'':

$$EI\delta'' = M = \frac{Fx}{2} - M_1 \quad (0 \le x \le \frac{L}{2}).$$

(21)

Integrating (21) twice to obtain deflection δ gives:

31

$$EI\delta = \frac{Fx^3}{12} - \frac{M_1x^2}{2} + C_1x + C_2 \quad (0 \le x \le \frac{L}{2}). \tag{22}$$

Boundary conditions and symmetry reveal:

$$C_1 = C_2 = 0 \tag{23}$$

$$M_1 = \frac{FL}{8} = M_2 \tag{24}$$

Substitution of (23) and (24) into (21) provides the deflection equation:

$$\delta = -\frac{Fx^2}{48EI}(3L - 4x) \quad (0 \le x \le \frac{L}{2}). \tag{25}$$

Maximum deflection is found at $x = (\frac{L}{2})$, which reveals:

$$\delta = \frac{FL^3}{192EI} \tag{26}$$

where δ is deflection, F the applied center load, L the length of the beam, E the Young's modulus of the beam material, and I is the moment of inertia [48]. The moment of inertia is given by:

$$I = \frac{wt^3}{12} \tag{27}$$

where w is the width of the beam and t is the thickness of the beam [48]. Further investigation into the required thickness of the beam is performed in chapter 3.

2.4.2 Cantilever Beam Micro-Contact Support Structure

The PolyMUMPs micro-contact support structure is modeled as a simple cantilever beam. With the use of Euler-Bernoulli beam bending theory, the deflection equation for the fixed end cantilever beam is found [49]. Using the method of moments, equation (28) is developed and used to determine the deflection for an intermediately placed load:
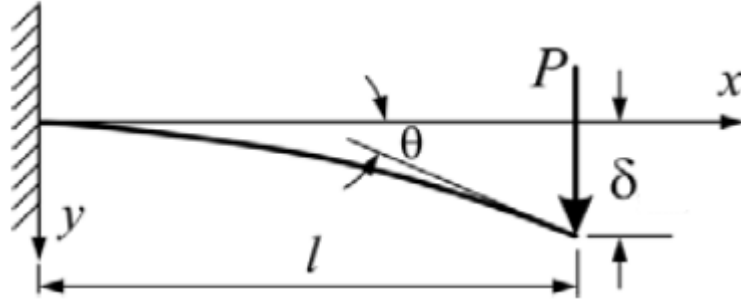
Figure 8 Cantilever Beam Micro-Contact Support Structure Model

$$\delta = \frac{Px^2(3L-x)}{6EI} \tag{28}$$

where δ is deflection, P the applied load, x is the position of the applied load relative to the beam tip, L the length of the beam, E the Young's modulus of the beam material, and I is the moment of inertia [48].

2.5 Device Fabrication

2.5.1 PolyMUMPs Fabrication

The PolyMUMPs process is a three-layer polysilicon surface micromachining process which is available for MEMS engineers to have their designs fabricated; one layer of polysilicon as a ground layer and two mechanical layers [50]. The process itself has seven layers as shown in Figure 9.

33
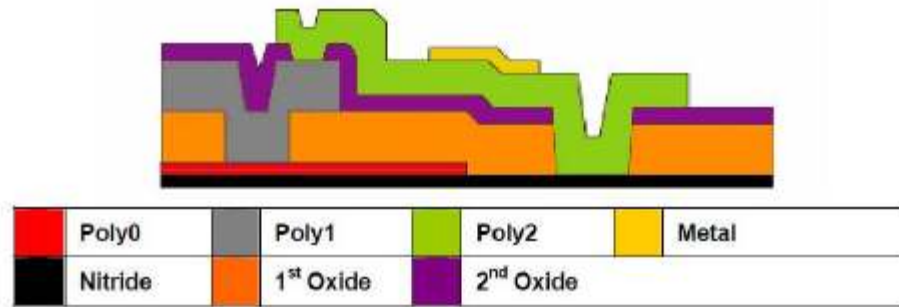
Figure 9 Cross-section of PolyMUMPS seven process layers [50]

Nitride is used as an electrical isolation layer between the polysilicon (poly) layers and the substrate. The oxide layers are used as sacrificial layers while the poly 0 layer is a ground layer and poly 1 and poly 2 are structural layers. The metal layer is a gold layer which is commonly used for electrical contact pads and electrical wiring.

2.5.2 Fixed-Fixed Beam Micro-Contact Support Structure

The fixed-fixed beam micro-contact support structure is fabricated using surface micromachining processes. Surface micromachining involves depositing, patterning, and etching sacrificial and structural layers. A device made via surface micromachining is released when sacrificial layers are removed and the structural layers remain. Figure 10 shows the surface micromachining process used to fabricate the fixed-fixed beam micro-contact structure.

34
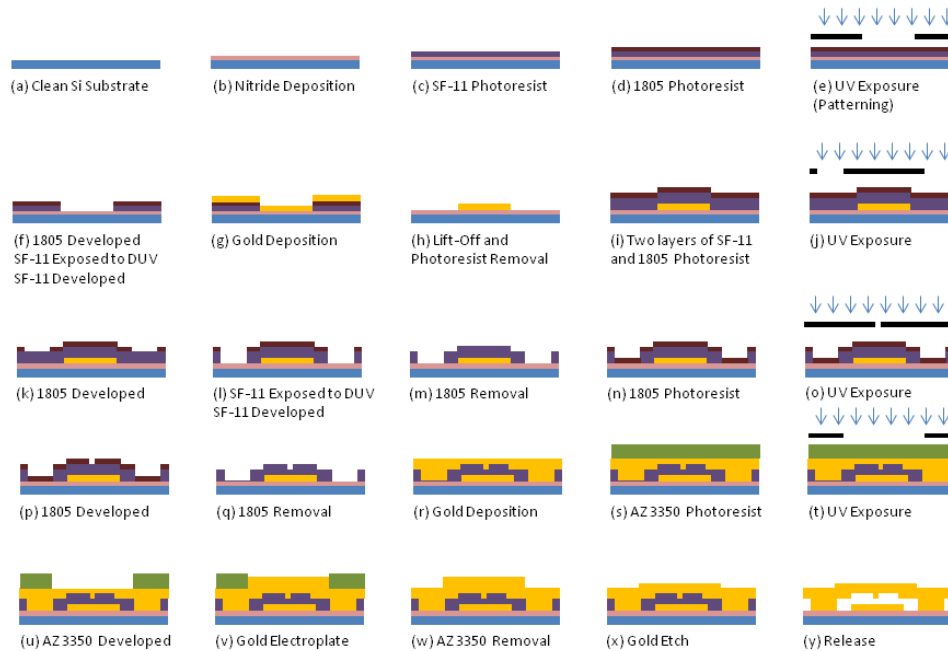
Figure 10 Surface Micromachining Process for Fixed-Fixed Beam Micro-Contact Support Structure

Beginning with (a), a silicon substrate is cleaned before a layer of nitride is deposited

(b). The nitride layer acts as an electrical isolation layer. In (c) and (d), a layer of SF-11

photoresist and 1805 photoresist is established on the surface of the nitride coated wafer.

The 1805 serves as a mask for patterning the layer of SF-11. In (e), the 1805 is patterned by

a mask and exposed to ultraviolet light. The ultraviolet light breaks the chemical bonds of

the photoresist in the exposed areas and allows the exposed 1805 to be developed away (f).

After the 1805 is developed, the exposed SF-11 is subjected to deep ultra violet light (DUV)

which, similar to the 1805, breaks the chemical bonds of the exposed SF-11 and allows the

exposed area to be removed. A gold layer is then deposited in (g). Following deposition, the

remaining gold is lifted off and all photo resist is removed (h). What remains in (h) is the

bottom metal layer of the fixed-fixed beam micro-contact support structure.

35

For the mechanical layer of the fixed-fixed beam micro-contact support structure, two layers of SF-11 and a layer of 1805 photoresist are coated on the wafer. The 1805 is patterned and developed in (j) and (k) and then the SF-11 is exposed to DUV and developed away (l). The 1805 is then removed in (m) and 1805 is placed on the wafer in (n). This allows for the patterning of the micro-contact bump. The 1805 is patterned and developed and the exposed SF-11 is exposed to a partial DUV to establish the micro-contact bump ((o) and (p)). In (q), the 1805 is removed and Au is sputtered in (r) as a seed layer for electroplating. AZ 3350 photoresist is applied in (s) and patterned (t) and developed (u) for electroplating (v). Once the desired amount of Au has been electroplated, the AZ 3350 is removed (w). To remove the seed layer, an Au etch is performed (x). To release the device, the sacrificial SF-11 is removed (y).

2.6 Commonly Used MEMS Designs
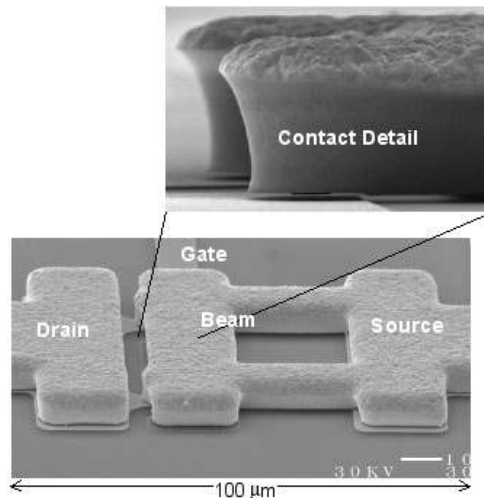
Figure 11 Electrostatic Micro-Switch Example [12]

In terms of design, the most common form of actuation is electrostatic [9]. Figure 11 shows an example of an electrostatic micro-switch. Electrostatic actuation offers the advantage of no power loss when the micro-switch is open. By applying positive voltage to

the actuation electrode, the grounded cantilever beam mechanically actuates and completes the electrical path when making contact to the finger of the signal plane, at which point, the switch is considered closed. To open the switch, the applied voltage is removed. This allows the mechanical restoring force of the beam to become dominant over the electrostatic force and physically open the connection; preventing current flow from continuing on the signal path. Many designs focus on enhancing the performance of the micro-switch by reducing the voltage required to actuate the switch. The electrostatic force is derived by treating the beam and actuation electrode as a parallel plate capacitor. When the beam width is w, the length of the pull down electrode is L, ε_0 is the permittivity of free space, and g is the gap between the beam and the electrode, and then the given capacitance is [51] :

$$C = \frac{\varepsilon_0 A}{g} = \frac{\varepsilon_0 L w}{g}. \tag{29}$$

The disadvantage can be the high actuation voltages required to close the micro-switch. It then follows that the electrostatic force applied to the beam is [51]:

$$F_e = \frac{1}{2} V^2 \frac{dC(g)}{dg} = -\frac{1}{2} \frac{\varepsilon_0 L w V^2}{g^2}. \tag{30}$$

The linear mechanical spring restoring force is represented by Hooke's Law:

$$F_s = -kd = -k\,(g_0 - g) \tag{31}$$

where d is the distance between the beam and electrode, also represented as $(g_0 - g)$ with g_0 representing initial position and g the new position. Also known as a spring constant, the variable k represents the mechanical restoring force of the beam. Equating the electrostatic force, (30) , and the static force, (31), gives:

$$\frac{1}{2} \frac{\varepsilon_0 L w V^2}{g^2} = k \, (g_0 - g) \tag{32}$$

which can be arranged for the pull-in voltage, or the point at which the beam 'snaps' down,

by solving for V at $g = g_0/3$:

$$V_p = \sqrt{\frac{8}{27} \frac{k g_0^3}{\varepsilon_0 L w}}. \tag{33}$$

Other forms of actuation include electrothermal, magnetic, magnetostriction, and piezoelectric [52, 53, 54]. Electrothermal and magnetic actuation both offer the advantages of low control voltages and high contact force but draw high current and dissipate significant levels of power when actuated [55]. Electrothermal also offers the advantage of being bi-directional with the ability to apply high force but its disadvantages include slow actuation (millisecond range) as well as quiescent power loss. A disadvantage also shared by magnetic actuation, quiescent power loss implies the use of power at all times. Hysteresis is another disadvantage of magnetically actuated micro-switches. Comparatively, magnetic actuation also has the advantages of high force actuation, being bi-directional but is also able to attain micro-second switching speeds. Also, due to their fabrication requirements, magnetic actuators are difficult to fabricate. Piezoelectric actuation can provide fast actuation speeds but due to the different layers of material that comprise a piezoelectric material, there is a parasitic thermal actuation caused by a differential thermal expansion of the different layers. Piezoelectric actuation has a disadvantage of 'short throw' or small movement based on the number of stacked layers. Given the low power loss, low insertion loss and high isolation when open, electrostatic actuation is the most commonly used method of MEMS engineers. Mechanical switch design considerations are focused on improving the performance of the

micro-switch through mechanical design innovation. From reducing the actuation voltage to decreasing the switching time, all aspects of performance are focused on the beam geometry. Sometimes this is referred to as "engineering away" shortfalls with the micro-electrical contacts.

2.7 RF Considerations

As stated previously, MEMS switches offer lower power consumption, better isolation, and lower insertion loss compared to conventional field-effect transistor (FET) and PIN diode switches [1]. Table 1 shows a comparison of performance characteristics between FET, PIN diode, and MEMS switches. The qualities of MEMS switches and relatively low cost of manufacturing make them ideal for applications in areas like switching networks, phased arrays, low-power oscillators and amplifiers [1].

Table 1 Performance Comparison of RF MEMS, PIN Diode, and FET [1]

Parameter	RF MEMS	PIN	FET
Voltage (V)	20-80	$\pm$3-5	3-5
Current (mA)	0	3-20	0
Power Consumption	0.05-.1	5-100	0.05-.1
Switching Time	1-300 μs	1-100ns	1-100ns
Cup (series) (fF)	1-6	40-80	70-140
Rs (series) (Ohms)	.5-2	2-4	4.-6
Cutoff frequency (THz)	20-80	1-4	.5-2
Isolation (1-10 GHz)	Very High	High	Medium
Isolation (10-40 GHz)	Very High	Medium	Low
Isolation (60-100 GHz)	High	Medium	None
Loss (1-100 GHz) (dB)	0.05-0.2	0.3-1.2	0.4-2.5
Power handling	<1	<10	<10

The MEMS literature indicates that varying the type of electrical load during testing reveals the physical limitation for micro-switches [56]. Rebeiz states that there is no specific definition for resistive failure however, a good assumption for failure of the micro-switch is

assumed to be when the contact resistance becomes greater than 5Ω, which results in an insertion loss of -0.5dB [1]. As a high-frequency signal passes through a switch, it is attenuated by series resistance and impedance mismatches. This attenuation is power loss through transmission and is known as insertion loss [1]. -0.5dB attenuation results in a power loss of 11%; which is dissipated in the form of heat. Attenuation as a function of resistance can be calculated by simplifying the well known expression:

$$10 \log\left(\frac{P_1}{P_2}\right) dB \tag{34}$$

where $\frac{P_1}{P_2}$ is the power ratio used to calculate power loss [1]. Substituting power in terms of current and resistance provides:

$$10 \log\left(\frac{I_1^2 R_1}{I_2^2 R_2}\right) = x\ dB. \tag{35}$$

Rearranging (34) gives:

$$10 \log\left(\frac{R_1}{R_2}\right) + 20 \log\left(\frac{I_1}{I_2}\right) = x\ dB. \tag{36}$$

With the knowledge that the micro-contact resistance changes over time and the assumption that the currents I_1 and I_2 are equivalent, then the attenuation as a change of resistance becomes:

$$10 \log\left(\frac{R_1}{R_2}\right) = x\ dB. \tag{37}$$

where R_2 is the initial contact resistance and R_1 is the contact resistance after a number of cycles.

According to Rebeiz, the primary cause of micro-switch failure is due to plastic deformation in the contact interface such as "damage, pitting, and hardening of the metal

contact area [which] is a result of the impact forces between the top and bottom metal contacts" [1]. The description relates closely to "cold" switching mechanical failure. "Cold" switching is generally known to be actuating the switch repeatedly without applying RF or DC power during actuations, increasing the probability of mechanical failures such as structural fatigue, memory effect, stiction of the actuators, etc [56]. In "hot" switching, contributors to early micro-switch failure include the mechanical modes and a higher probability of "material transfer high current density in the contact region and localized high-temperature spots" [1].

2.8 Contact Materials for Performance and Reliability

The earlier discussion of micro-contact resistance modeling showed how the material properties of the contact impact the contact resistance. The intrinsic properties of the materials chosen for the contact are important for increasing the lifecycle of the contact. For instance, due to its low electrical resistivity and low sensitivity to oxidation [57], gold is widely employed as a contact material in MEMS [58]. In general, contacts are desired to have excellent electrical conductivity for low loss, high melting point to handle the heat dissipated from power loss, appropriate hardness to avoid material transfer and chemical inertness to avoid oxidation [59]. As will be discussed in the failure modes and reliability section, material transfer can take place less easily with harder materials.

Material hardness is an important property as the surface of the contact will change with actuations over time. As the surface changes, changes to contact resistance occur simultaneously. The surface change can be seen in Figure 12 which shows SEM images of Au-Au contacts after a lifecycle test [3]. Alloys are often created in order to take advantage

41

of material properties to try and minimize the effect of material transfer [3]. As can be seen
in by comparing Figure 12 to Figure 13, Zang *et al.* showed Au-Ni alloy contacts resist
material transfer better than Au-Au contacts [3].
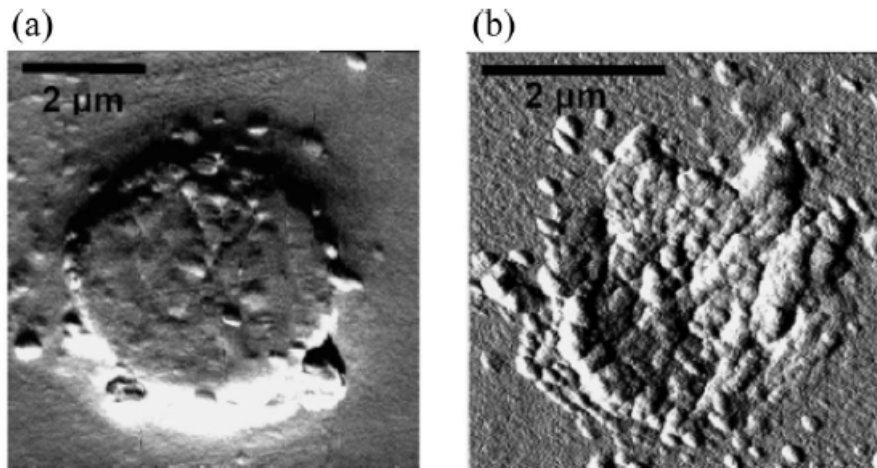
Figure 12 Au on Au contact SEM images of contact surfaces (a) is top electrode (b) is bottom electrode [3]
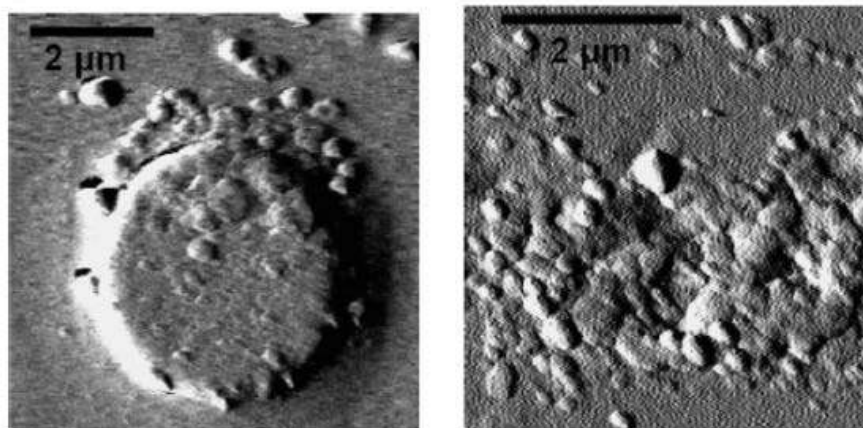
Figure 13 Au-Ni alloy contacts [3]

McGruer *et al.* showed that ruthenium (Ru), platinum (Pt), and rhodium (Rh) were
susceptible to contamination and the contact resistance increased after a characteristic
number of cycles, while gold alloys with a high gold percentage showed no contact
resistance degradation under the same test conditions [3, 60]. Similarly, Coutu *et al.* showed

that alloying gold with palladium (Pd) or Pt extended the micro-switch lifetimes with a small increase in contact resistance [15]. Failure is typically defined as an increase in contact resistance beyond a given tolerance set by the circuit designer. As is shown in Figure 14, contact resistance tends to increase towards the end of a micro-switches lifetime.
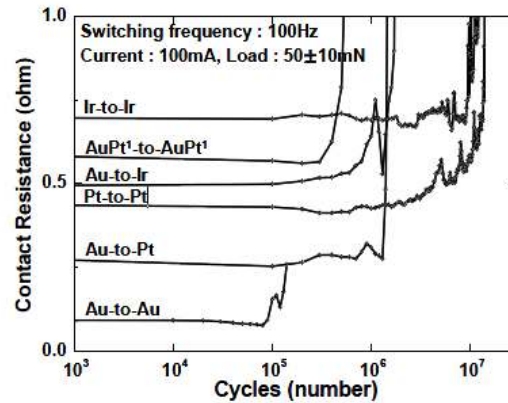
Figure 14 Evolution of contact resistance for hot switching 100mA at a contact force of 50mN [61]

As will be discussed later, frictional polymers are carbon based insulating films which develop over time and increase contact resistance [9]. Despite carbon being a core component to frictional polymers, Yaglioglu *et al.* examined the electrical contact properties of carbon nanotube (CNT) coated surfaces [62]. The high Young's Modulus and potential for low resistance of CNTs makes them suitable candidates for micro-switch contacts. For instance, Au contacts with a substrate coated with tangled single-walled CNTs were shown to have a resistivity between $1 * 10^{-4}$ and $1.8 * 10^{-4}$ Ωm [62]. CNTs have been reported to have an elastic modulus of approximately 1TPa, which is comparable to diamond's elastic modulus of 1.2 Tpa [63]. Yunus *et al.* explored two contact pairs with carbon nanotubes: Au to multiwall carbon nanotubes (MWNTs), where one electrode is Au and the other is MWNTs, and Au to Au/MWNT composite, where the contact interface is Au on Au [64]. Fig. 10 shows an SEM image of the Au/MWNT composite.

43
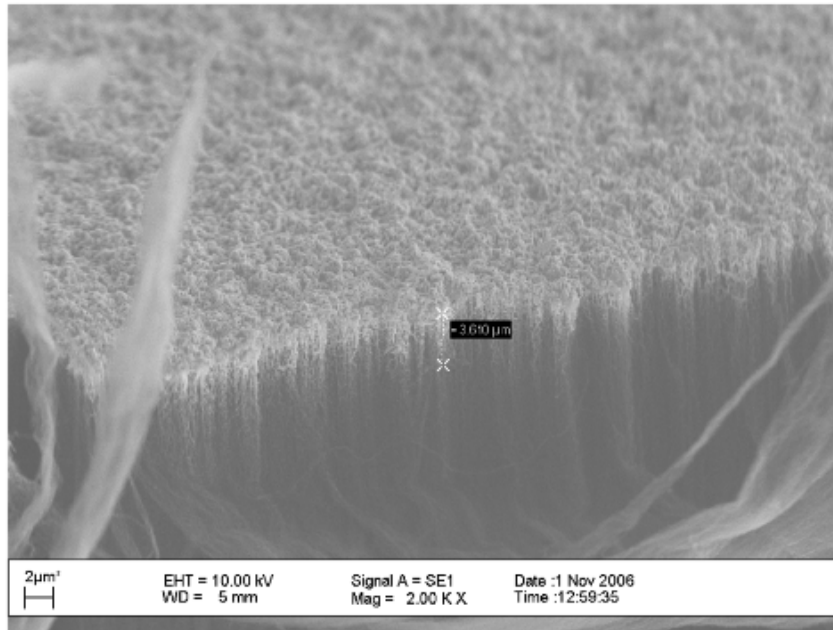
Figure 15 2-4µm of Au coating on MWNT [64]

As shown in Figure 16, it was found that the Au-Au/MWCNT was the better performer than Au-MWCNT in terms of contact resistance [64]. While the MWCNTs did not improve contact resistance, the modulus of the lower contact was enhanced which could lead to greater reliability. The data was collected with a nanoindentor apparatus which cycled for ten repeated operations with a maximum applied load of 1mN [64]. The hardness of each material is also dramatically different, approximately 1TPa for CNT and 1GPa for Au [64]. The CNT structure supporting the Au film acts to allow the Au film to deform elastically under the applied load. In this study, a hard Au coated steel ball is making contact with the softer Au/MWCNT surface. The latter surface deforms to the shape of the steel ball, increasing the apparent contact area. With the Au coated steel ball in contact with the MWCNT surface the conduction path is through the lateral connection of the vertically aligned CNTs; leading to a higher contact resistance, as shown in Figure 16. A disadvantage

to the mechanical design of the switch was discovered to be excessive bouncing on closure; that is, the contact takes time to settle in the closed position.
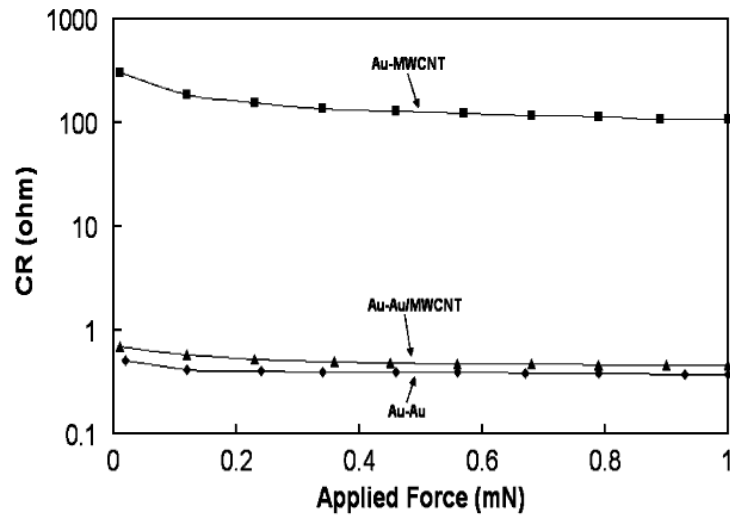
Figure 16 Comparison contact resistance (CR) of Au-MWCNT to Au-Au/MWCNT and Au-Au contacts [64]

A study was conducted by Choi *et al.* to explore the current density capability of a CNT array with an average CNT diameter of 1.2nm, site density of 2CNT/µm, and the number of CNTs for devices with 1µm channel width ranged from one to three [65]. It was reported that a high current density of 330A/cm^2 at 10V bias was successfully transmitted through the contact without any noticeable degradation or failure [65]. A reliability test, as seen in Figure 17, with an input current of 1mA showed repeatable and consistent contact characteristics over a million cycles of operation [65].
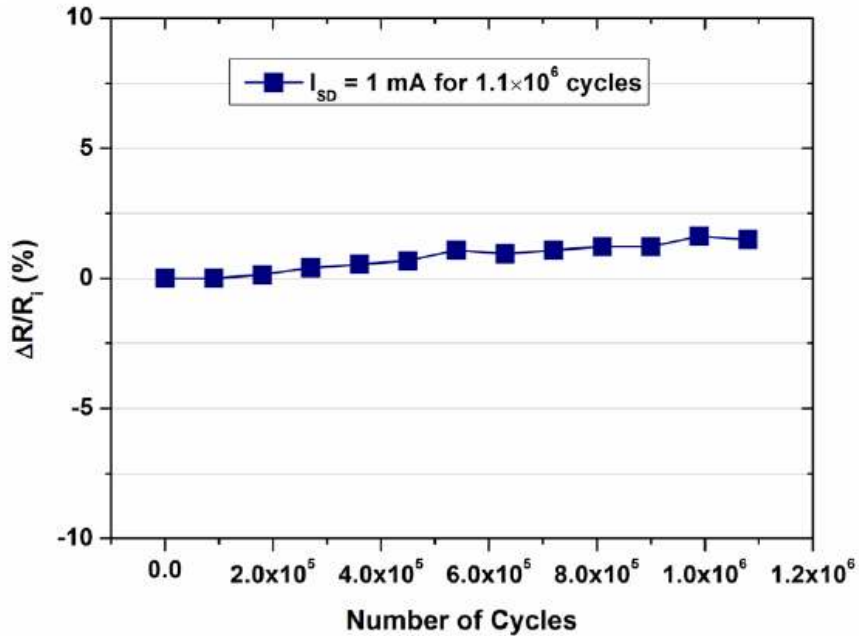
Figure 17 Reliability test results shown the resistance change over 1.1*10^6 cycles at 1mA in non-hermetic environment [65]

It is reported in literature that the small contact area between carbon nanotubes and a metal electrode makes electrical coupling between them extremely difficult [66, 67, 68, 69]. An experiment was performed by Chai *et al*. to verify if a graphite interfacial layer would increase the electrical contact to the CNTs [66]. Graphite was chosen due to its close material properties to the CNTs namely, metal-like resistivity and similar chemical bonding [66]. A common technique for carbon deposition to the CNT contact region is to use the electron beam inside of a scanning electron microscope (SEM) to induce carbon deposition [66]. The technique is reported to successfully form low resistance electrical contact to multiwalled CNTs [70, 71]. Chai's experiment validated that the graphitic carbon interfacial layer did reduce the contact resistance due to the increase in contact area to the CNT [66].

Another metal-coated-contact switch design was explored by Ke *et al.* which used ruthenium (Ru) on the gold (Au) contact surface [72]. In an example of engineering a

46

contact for increased lifetime, an Au contact was coated with Ru, a harder material with relatively low resistivity [72]. The contact resistance and life time of the Ru layered Au switch were compared to the common Au-Au micro-contact switches [72]. The switches demonstrated an increase in lifetime by an order of magnitude as measured in a non-hermetic environment as compared to pure, soft gold contacts as shown in Figure 18 [72]. On the other hand, alloying Au with other metals results in increased hardness, but also an increased resistivity [73]. Atomic-level simulations and experimental observations have shown that the separation of gold contacts leads to considerable material transfer from one side of the contact to the other [74, 75, 76].
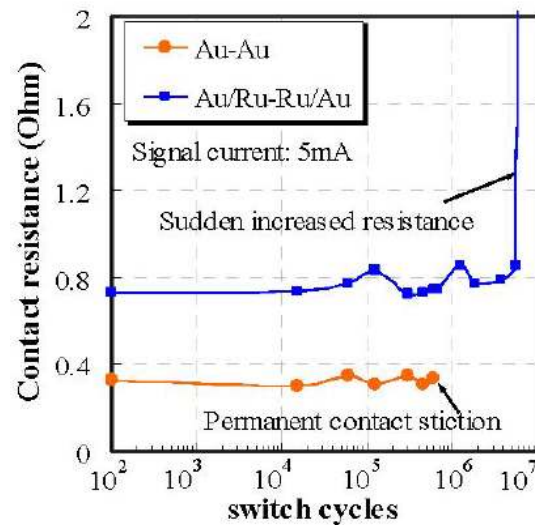
Figure 18 Hot switching life cycle tests for Au-Au switch compared to Au/Ru switch [72]

Broue *et al.* characterized Au/Au, Au/Ru, and Ru/Ru (upper and lower contact materials respectively) ohmic contacts by examining the temperature of the contact in the on-state to determine its performance limitations [47]. For the Au/Au contact, the contact temperature was linear until it seemed to stabilize and fluctuate between 80ºC and 120ºC

after the application of 40mA [47]. This is agreeable with the reported maximum allowable

current for gold contacts of 20 to 500mA [77]. The published softening temperature for gold

contact is ~100ºC, which corresponds to a contact voltage of 70-80mV for a contact near

room temperature [8]. Comparatively, the published temperature for ruthenium contact is

~430ºC, corresponding to a contact voltage of 200mV for contact near room temperature

[77]. The Ru/Ru contact exhibited similar behavior in that it fluctuated about 400ºC after

reaching a critical current level of 30mA [47]. The contact with the best performance was

the Au/Ru combination contact, where the contact temperature increased with the current

level without reaching a maximum [47]. The experiment went as far as to apply 100mA for

all three combinations [47]. An explanation to the difference in performance was offered

that the contact temperature of the Au/Ru contact is more stable because the softening

temperature is theoretically not reached for the same contact current [47].

In the interest of exploring the limitations of Ru, Fortini *et al.* compared how asperity

contacts form and separate in gold and ruthenium [78]. Their technique was to establish an

appropriate interatomic potential in order to apply Molecular dynamics (MD) simulation,

which is a powerful tool for studying adhesion, defect formation and deformation on the

nano-scale level [78]. The MD technique enabled the team to understand the formation and

separation of nanoscale asperity contacts by simulating the motion of the atoms [79]. The

simulations showed that Ru was ductile at T=600K and more brittle at T=300K, where it

separated by a combination of fracture and plasticity [78]. Gold exhibited ductile behavior at

both T=150K and T=300K [78, 80]. The difference in ductile/brittle behavior of the Au and

Ru contacts has consistent with FEM calculations in literature [81].

Other researchers have explored using Tungsten (W) as the contact material. Tungsten was chosen for its hardness and resistance to mechanical stress and physical deformation [82]. Kam *et al.* verified that W is beneficial for improved resistance to wear and micro-welding [83]. A disadvantage of W is its susceptibility to chemically react and form oxides on the surface [82]. It is reported that oxidation of exposed W electrode surfaces occurs if there is any ambient oxygen, which increases the rate of oxidation exponentially with increasing temperature [84]. This was verified by Spencer *et al.*, who studied the oxide layers as they became thicker with exposure time; they offered the theory that the exacerbated rate of oxidation is due to the widening of the oxygen diffusion path as the oxide gets thicker [85]. This thin film of oxide negatively impacts the contact resistance and requires higher contact loading to break through the film and obtain low resistance. The experiments of Chen *et al.* show that W electrodes show an undesirable increase in the on-state resistance over the lifetime of the device [82]. The oxidation of W was sped up by the amount of current flowing through the contact. Energy losses in the form of heat increased the opportunity and rate of thermal oxidation. They offered two solutions to the oxidation problem of W electrodes: either use another material or minimize device exposure to oxygen with a wafer-level encapsulation process [82, 86].

Yamashita *et al.* investigated the use of an anti-stiction coating for ohmic micro-contacts under low loads (0 to 70μN) [87]. The contacts were coated with thiophenol and 2-naphthalenethiol. The coatings successfully prevented the formation of the liquid meniscus, eliminate or reduce the capillary force better than the bare Au surface, and reduce the van der Waals forces [87]. They also noted that increased surface roughness could prevent stiction exponentially by reducing the effective contact area [87]. Increasing surface roughness

would trade performance in terms of lower contact resistance which relies on large effective area of contact for anti-stiction properties. With the coatings applied, contact resistance decreased after 16µN but required at least 4µN of contact force for current to begin to flow [87]. It was found in the study that the contact resistances of the samples deposited with a 100 nm-thick Au layer were slightly smaller than those with a 20nm-thick Au layer despite the larger resistivity value for the thicker layer due to the relationship between surface roughness and resistivity [87, 88]. An answer was offered by Yamashita *et al.* that the contact area between the electrodes was larger for the thicker layer because the electrodes made contact with large crystal grains [87]. Consistent with literature and classical theory, the results showed that contact resistance decreased proportionally with increasing contact force for all samples [87]. Because of increased contact forces, the contact resistance drops with an increase in asperity deformation, which provides a greater contact area as the micro-geometry changes [89, 90]

As expressed earlier, increases in contact area decrease electrical contact resistance. One method to increase contact area was examined by Baek and Fearing using compliant nickel nanowire arrays [91]. The concept is to guarantee an approximate number of contact points for current to flow when the electrode surfaces mate instead of relying on rough approximations for asperity micro-geometry. Since the nanowires are compliant, the effective contact area would increase as contact force is increased overall decreasing contact resistance. The array was employed to achieve a minimum contact resistance of 73mΩ for a contact area of 0.45mm² using an array of compliant nickel nanowire [91]. The wires were fabricated by electrodeposition and porous filters in order to achieve a maximum aspect ratio of 300:1 (60µm x 0.2µm) [91]. Images of the nanowire arrays are shown in Figure 19.
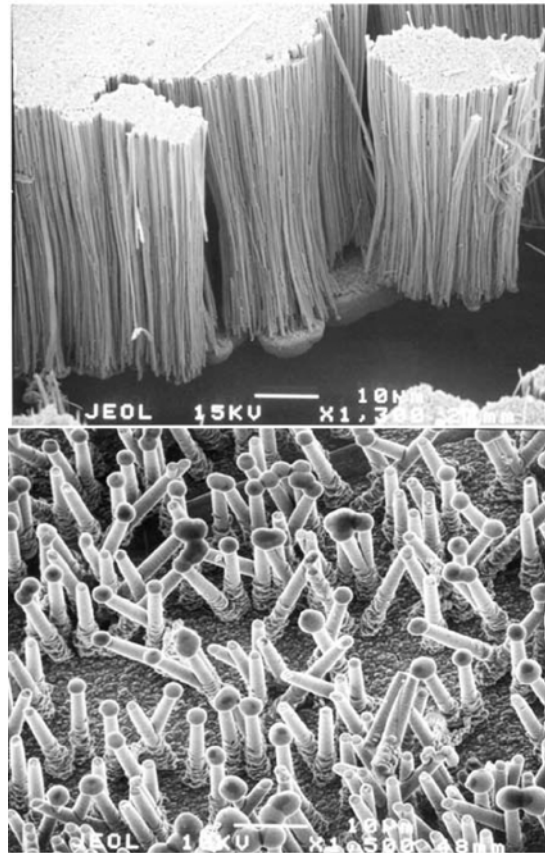
Figure 19 SEM images of nickel nanowires (.2x60μm on top and 2x20μm nickel nanowires with sphere tips) [91]

Regarding the reduction electrical contact resistance for tin contacts, Myers *et al.* proposed a new contact design in order to lower contact resistance which is not limited to tin [92]. The fundamental principles behind the concept was that when the classical Hertzian surface makes contact, the mechanical load is carried by asperities in the center of the contact while the electrical load is distributed by asperities along the outer rim. As oxides and other surface contaminants may appear, the team suggested designing the contact so that the outer rim asperities were the only asperities that would make contact i.e. bearing the mechanical and electrical load; this would allow the asperities to break through any

developed contaminants as well as reduce electrical contact resistance by appropriately applying force along the conducting asperities. This novel concept was simulated to verify that the contact resistance of an outer rim maximum load and current density asperity contact interface design can be significantly lower than a similarly finished Hertzian style contact interface. Based on simulation, the final results revealed that the greatest contact resistance reduction (up to a factor of 2) occurred for a mated tin finished surface.

2.9 Failure Modes and Reliability

There are a number of potential applications for the MEMS relay if the problems identified can be resolved. The target is to actuate billions of switching cycles with low current loading. Typically, designs are for a supply voltage of 4-5 Volts; which is below the minimum voltage required for arcing and a switching current below the minimum arcing current. If the supply current exceeds this minimum, there will be a discharge process which will degrade the switching performance. The lower limits of arcing are not clearly defined and will be influenced by any inductance and capacitance in the circuit. The occurrence of arcing will depend on the contact materials as well as the distance between the upper and lower contacts. At the lower limits of supplied current and voltage, arcing is predicted with a probability function. For switching applications, it is desirable to have no arcing. It was suggested by Jemaa and Hasegawa that for Au contacts the lower limit for no arcing is 80mA, however, these experiments were conducted at a voltage above the minimum arcing voltage [93, 94, 95]. In the context of RF switching, an investigation of the basic switching phenomena is provided by Johler and Miki *et al.*, in these examples, arcing is present between the contacts [96, 97].

Contact bouncing can greatly impact the lifetime and performance of electrical contacts. To that end, Peschot and Poulain *et al.* performed experiments to better explain contact bouncing at the nanometer scale [98]. Using an AFM and a nano-indenter, the researchers controlled micro- contact make and break operations at low values of electrode velocity (few tens of nm/s). They discovered that the electrostatic force overcame the mechanical restoring force of the mobile contact near 10nm. The team analytically ruled out the Casimir force by examining the effective distance for which the quantum electrodynamic force would have effect. It was found that the Casimir force was only dominant in the last few nanometers. The explanation for contact bounce was given as the product of competition between the restoring force of the contact beam and the adhesion force. The adhesion force is considered as contact interactions such as capillary, chemical, and Van der Waals forces [99]. As the contact is made and the voltage between contacts is near zero the competition begins between adhesion force and restoring force. Upon opening of the contact, a potential difference is created and is the electrostatic force; which influences the contact to be made again. The final result revealed that for the given mechanical design of the beam, the velocity of the contact beam has to be higher than 1µm/s in order to avoid bouncing due to the electrostatic force.

To analyze contact bounce, McCarthy *et al.* tried modeling the dynamic behavior of two different electrostatically actuated micro-switch configurations with time-transient finite difference analysis. The two configurations included one switch of uniform width and the other switch of nonuniform width. The model used dynamic Euler-Bernoulli beam theory for cantilevered beams, includes the electrostatic force from the gate, takes into account the squeeze-film damping between the switch and substrate, and includes a simple spring model

of the contact tips [100]. The uniform width switch was modeled using Euler-Bernoulli beam theory with a constant cross-sectional area along the length of the beam. Once the equations of motion were found, a finite difference numerical solution to the resultant differential equation was obtained. The analytical solution was considered impractical due to the non-linearities in the electrostatic force and in the squeeze-film damping. The model expressed the applied voltage as a fraction of the static threshold voltage and the electrostatic force was the force per unit length acting on the beam in the region directly above the gate. Squeeze-film damping pressure, due to the air film between the beam and the substrate, was determined using the simplified form of the Navier-Stokes equation known as the Reynolds equation [100]. The Reynolds equation assumes that the viscous and pressure force in the fluid film dominate the inertial terms [100]. The model of the contact tip is comprised of a simple spring at the free end of the beam. The tip acts as a constraint on the free end of the beam. Once the contact is made, the beam is considered no longer cantilevered, but fixed at one end and spring-supported at the other end [100]. To verify the effectiveness of the model, McCarthy *et al.* fabricated the contacts and tested against the simulation parameters. They chose to neglect bounces greater than 5nm. The impact of contact bounces less than 5nm is dependent on mechanical beam design. The researchers found that applying voltages higher than threshold actuation voltages reduced quantity of contact bounces. There was excellent agreement between theory and experiment with respect to the initial closing time and duration of the first bounce. The work of McCarthy *et al.* is another example of MEMS switch designers attempting to engineer away any reliability problems related to micro-contacts.

"Cold" switching is generally known to be actuating the switch repeatedly without applying RF or DC power during actuations, limiting the switch lifetime to mechanical failures such as structural fatigue, memory effect, stiction of the actuators, etc [56]. Simply put, "cold" switching is powering the circuit off, then actuating the switch off then on, and then powering the circuit back on. To model "cold" switching, the circuit elements would not contain stored energy at the time the switch closes and all energy would dissipate between actuations. This limits the types of failures of micro-switches to purely mechanical failure modes and extends the reliability of the micro-switch. "Hot" switching is considered to be actuating the switch repeatedly while applying RF or DC power during actuations [56]. Zavracky et al reported over $2*10^9$ cycles as the lifetime for Au sputtered contacts that were packaged in nitrogen [6]; a considerable difference compared to the $5*10^8$ cycles Zavracky reported for "hot-switched" contacts. Majumder et al reports greater than 10^7 "hot-switched" cycles and approximately 10^{11} "cold-switched" cycles for micro-switches with a "platinum group" contact metal [101]. Newman et $al.$ also performed lifetime measurements on high-reliability contacts and reported average lifetimes of cold switched contacts at $430*10^9$ cycles [102]. In comparison, the "hot-switched" at 4V, 20mA, Au coated MWCNT surface exhibited $7x10^7$ cycles in initial studies [102, 103].

Toler and Coutu characterized the impact on reliability of external resistive, inductive, and capacitive loads for micro-switches [104]. Certain configurations of loads were determined to enhance micro-switch reliability. Specifically, that an external resistive load in series acts as a current limiter for both "hot" and "cold" switching conditions and reduces the probability of an electrical failure mode thereby enhancing the reliability of the micro-switch. In addition, there is a possibility of increasing the reliability of the switch by

using a higher resistance contact metals with a matching external resistive load. The current limiting effect would restrict temperature and increased hardness of the higher resistance contact metal would most likely extend the reliability of the micro-switch further than a low resistance contact metal. Alternatively, it was found that certain configurations of resistive, inductive, and capacitive loads promote early failure via increased material transfer and current density. An external capacitive load in parallel was determined to be detrimental to micro-switch reliability under "hot" switching conditions since it compounded the current during discharge and raised the probability for increased current density, temperature, and material transfer. For "cold" switching conditions, the discharge of the capacitor essentially continues to provide current through the contact after the signal has stopped transmitting and before the switch opens; effectively turning a "cold" switching condition into a "hot" switching condition and reducing reliability with the increased probability of electrical failure. Lastly, the external inductive load for DC conditions reduced susceptibility of failure via increased current density and temperature by limiting the current at the moment of initial contact in "hot" switching conditions. "Cold" switching conditions for external inductive loads have negligible effect to contact resistance and micro-switch reliability.

As mentioned earlier, stiction or adhesion is a failure mode which is commonly caused by capillary, electrostatic, chemical, and van der Waals forces [99]. The surface of contacts in air can become hydrophilic due to oxidation and formation of a liquid meniscus by water vapor causes stiction [87]. Many researchers have proposed reducing the surface adhesion force by novel switch design, contact materials, and sealing the micro-contacts in inert gases [3, 87, 105, 106, 107, 108]. Adhesion can be described by Hertz, JKR, or DMT theories [109]. Hertz theory, mentioned in the contact resistance modeling section, is

56

traditionally used for modeling elastic adhesion between non-deformable surfaces [109]. For deformable surfaces, JKR or DMT theory is utilized. JKR theory takes into account the surface energy of the contacting interfaces. Comparatively, DMT theory emphasizes the cohesive forces at the contact periphery [109]. The JKR model is valid for "soft" elastic materials with higher surface energy while the DMT model is applicable for "hard" stiff solids with low surface energy [109].

A multiscaled approach was developed by Wu *et al.* in order to predict stiction due to Van der Waals forces [110]. For micro-scale calculations, the unloading adhesive contact-distance curves of two interacting rough surfaces were established from a combination of an asperity model and the Maugis transition theory [110]. The computed unloading distance curves were dependent on the material and surface properties such as roughness discussed earlier in this chapter [110]. The model was then integrated into a macro-model for the ease of finite element analysis [110]. The parameters for the FEM in terms of surface topography and micro-geometry were evaluated from theoretical models, surface energy measurements, or AFM measurements [110]. The key advantage of the model is its ability to account for a wide variety of micro-scale parameters such as surface topography, surface cleanliness, etc. while still enabling complete modeling of the larger MEMS structure using FEM [110]. The disadvantage of this approach is the absence of the effect of capillary forces [110].

Fretting is a form of structural fatigue which is defined as accelerated surface damage occurring at the interface of contacting materials subjected to small oscillatory movements [9]. Braunovic states that the lack of published information of failures due to fretting is because fretting is a "time-related process causing an appreciable effect only after a long period of time as a result of the accumulation of wear debris and oxides in the contact zone"

[9]. However, contact force has significant influence on the contact resistance in fretting conditions. As the force applied on the contact is increased, the contact resistance declines until there is a significant amount of wear debris and oxide to form an insulating layer. As the insulating layer develops, the resistance increases despite larger applications of force. Fretting is a rate dependent phenomenon and the frequency of oscillations will affect the contact resistance.

Another "cold" switch mechanical failure cause is pitting. Pitting and hardening occur when two metals make contact repeatedly at the same location [1]. The repeated actuations create cavities at the surface and are confined to a point or small area [9]. The areas are described as being irregularly shaped and are filled with corrosion products over time [9]. The buildup of corrosion products in conjunction with pitting reduces the area available for current flow and will induce high temperatures at those areas while the switch is closed. The result will be a localized high temperature failure mode as seen in "hot" switching conditions.

According to Kim, the lifetime of a switch is more restricted by "hot"-switching than by "cold"-switching because most of the signals that are transmitted through the switch have high power loads [56]. Electrical failure mechanisms, like temperature, current density, and material transfer are all factors in reliability under "hot" switching [1]. With an emphasis on no arcing, the transfer of material between electrical contacts in MEMS devices below the minimum arcing voltage is known as "fine transfer" [103]. A major consideration in "hot" switching is a large temperature rise which occurs in the contact region due to the small contact area on the a-spots [1]. With a small contact region comes a large contact resistance, which in the case of "hot"-switching will result in large heat dissipation in that area at the

58

time the switch closes. Increased temperature at these localized points may soften the contact metal and lead to bridge transfer. A problem with bridge transfer is that the internal stresses cause the contact metal to shrink and crack [9]. Oxidation then leads to a reduced number of electrical conducting paths thereby leading to overheating and ultimately failure [9].

An increase in current density raises the temperature for the contact areas on the cathode and anode. Concerning the topology of the contact surface, which has asperities, a higher current density will cause high temperature spots at asperities. The relationship between the temperature in the contact and voltage drop across the contact is described as:

$$V_c^2 = 4L(T_c^2 - T_o^2)$$

(38)

where V_c is the voltage drop across the contact, L is the Lorenz constant, T_c is the temperature in the contact, and T_o is the bulk temperature. It is important to note that the relationship between voltage and temperature above does not consider the size effects of the asperities in contact [111]. Examining (38), an increase in current would result in an increase in temperature due to I^2R loss. The resistance is expected to increase because of the metal's positive temperature coefficient of resistance, α. The equation for resistance R_c, at the new temperature T_C is then:

$$R_c(T_c) = R_{co}[1 + \frac{2}{3}\alpha(T_c - T_o)]$$

(39)

but (39) only holds true until a temperature is reached that softening of the metal begins to occur. When the contact metals are softening, the asperities collapse, increasing their areas to facilitate cooling. The collapsing of asperities increases the effective contact area and results in a decrease of the contact resistance. The plastic deformation of the asperities during the contact formation proceeds more rapidly when the softening temperature is reached [78].

This is seen by contact resistance as a function of area:

$$R_c = \frac{\rho}{2}\sqrt{\frac{1}{2R\alpha}} \tag{40}$$

and R is asperity peak radius of curvature and α is asperity vertical deformation [15]. Immediately following initial asperity deformation, contact asperities are susceptible to creep under compressive strain [37]. Creep deformation has been reported by Gregori *et al.* as well as Budakian *et al.* at micro-Newton level contact forces and low current levels [112, 113]. With creep, the contact material deforms and reduces the contact pressure, resulting in increased contact resistance [9].

The softening of the metal at the asperities of the contact reduces the strain hardening of the a-spots and could accelerate the aging of the contact by the activation of thermal failure mechanisms such as bridge transfer [59]. High temperature for the small volumes of material changes the softness of the contact material and promotes bridge transfer. Holm noted that material transfer of very small volumes of material was known originally as fine transfer and said the phenomena is usually called bridge transfer. Bridge transfer is a form of material transfer which reduces the effective area of the asperities and increases the contact resistance [8]. Also, increased temperature decreases the mobility of electrons in a metal, resulting in increased resistivity. If the choice of contact materials is not appropriate, the materials may not be able to conduct away the resistive heat generated by currents passing through surface asperities, the large local temperature increases and will further the probability of bridge transfer [89, 114]. Changes to the surface topology are detrimental to contact resistance. When the contact opens, a newly ruptured bridge can provide better conditions for field emission when the electrodes are in close proximity and a voltage exists

across them. Temperature is an important consideration for contact design. Increased contact temperatures can sometimes activate diffusion and oxidation processes that are driven by elevated temperatures, which ultimately reduces surface conductivity and contact resistance will increase [115, 116].

Dickrell and Dugger simulated a Au-Pt micro-contact using a nanoindentor in order to test and examine the performance of Au-Pt contacts [21]. The experiment showed that the contact experienced a dramatic increase in contact resistance, by orders of magnitude, when hot-switched in both ambient and inert nitrogen environments [21]. The results indicated that arc formation at the time of opening or closing was the cause of increased resistance [21]. Arcing resulted in a decomposition of the surface contaminants and the creation of an insulating surface layer [21].

Considering DC, electromigration is another form of material transfer which causes micro-switch failure [9]. Electromigration is defined as "the forced motion of metal ions under the influence of an electric field" [9]. Atomic flux (J) is given by:

$$J = \frac{D}{kT}J\rho eZ^* \tag{41}$$

$$D = D_o e^{-\frac{Q}{kT}} \tag{42}$$

where D is the diffusion coefficient, J is the current density, ρ is the electrical resistivity and eZ^* is the effective charge, k is the Boltzmann constant, T is the absolute temperature, D_o and Q are the diffusivity constant and activation energy for diffusion, respectively [9]. As shown by (41), atomic flux is directly proportional to current density. Voids form as a result of electro-migration and ultimately cause device failure [9]. Braunovic states that an increase in current density in the a-spots can be substantial and create the right conditions for

electro-migration to occur [9].

Distinct from electro-migration, field emission is also responsible for material transfer phenomena [117]. Field emission is the transfer or emission of electrons induced by an electrostatic field. Literature in this area is limited, however, Poulain *et al.* conducted an investigation into the phenomena using a modified atomic force microscope [117]. The results showed a current increase when the contact gap became smaller than a few tens of nanometers [117]. At that range, the team deduced that the emission of electrons from the cathode follow the Fowler-Nordheim theory and lead to damage on the opposite contact member [117]. The damage to the opposite contact member consists of evaporated anode material caused by impact heating (electrons leaving the anode heat the material and cause evaporation of anode contact material to the cathode interface) [117]. The reported transfer of material due to field emission occurred with an open-circuit voltage across the two contact members at 5V and the test current limited to 1mA when the contact is closed.

For complete integration with CMOS processes, micro-switches need to withstand temperatures of about 400ºC without a change in performance [118]. At high temperatures, cantilever beams normally begin to deflect due to intrinsic stresses in the layered materials making up the beam. Klein *et al.* designed an electrostatically actuated micro-switch based on a tungsten-titanium alloy to reduce the possibility of failure due to temperature and stiction [118]. Klein *et al.* chose tungsten for its high melting point of 3370ºC, which is a good indicator of stability for temperatures a tenth of the melting point value [118]. The tungsten-titanium alloy switches were evaluated to temperatures up to 500ºC and the results indicate that the design is stable with beam deflections of only 8% [118]. Insertion loss was

reported to be slightly higher than compared to more conductive switches but isolation was comparable [118].

No discussion of failure modes is complete without referencing the development of frictional polymers. Metals most susceptible to the development of frictional polymers are the platinum group metals and any other "catalytically active metal" [9]. Holm points out that thin films, like oxides, develop over time on the contact surface and act as insulators, greatly increasing contact resistance [14]. The same is true for micro-switches. Though much smaller than the contacts studied by Holm, the effects of the films which develop on a micro-contact are orders of magnitude greater than those on macro scale contacts. Films on micro-contacts can render the contact useless and disabled. A particularly damaging film is the development of a frictional polymer [9]. Frictional polymers are organic films, sometimes referred to as deposits, that develop on commonly used contact materials when there are low levels of organic vapors or compounds evident in the operating environment of the contact [9]. Crossland and Murphy, however, were able to show that the addition of a non-catalytically active metal, like silver, can significantly reduce the effects of frictional polymerization [119]. Though silver is not considered suitable for MEMS due to tarnishing, their experiment showed that silver must make up 36% or more of the contact materials in order to witness a significant reduction [119].

2.10 Summary

This review provides insight into the properties and concepts necessary for designing micro-electrical contacts for DC and RF MEMS switches. The basic theories behind the aspects of design, contact resistance modeling, contact materials, and failure modes are

discussed and explored. A survey of the challenges for these areas in ohmic contacts is provided. Complete models of contact resistance for various electron transport modes and deformation models are shown. The decision for contact materials is investigated by examining the impact of material properties on the characterization of the contact.

III. Methodology

3.1 Chapter Overview

This chapter describes the research methodology used in order to explore and characterize the physics of the evolution of micro-contacts over their lifetime of performance. Understanding how the physics of the micro-contact interface evolves will enhance micro-contact development time and help predict lifetime performance. Required goals to accomplish this research included: to improve a test fixture to examine lifetime evolution characteristics of a micro-contact; to generate a description of the witnessed micro-contact evolution phenomena; and compare the performance of various micro-contact structures. In reference to improving a micro-contact test fixture, the specific goal was to surpass the currently reported micro-contact testing rate of ~.5 Hz for a modified Atomic Force Microscope (AFM) and achieve a rate more conducive to lifecycle testing [7]. After witnessing the performance evolution of micro-contacts, the specific goal was to find an accurate description for the changing micro-contact interface physical phenomena. Lastly, the specific goal of comparing the performance of various micro-contact structures was to determine the best structure for studying micro-contact physics in order to develop predictors for micro-contact performance based on micro-contact material choice.

3.2 Comparison of Goals to Previous Works

Previous systems employ the use of an AFM to apply a known contact force. However, the AFM limits the rate at which the micro-contacts can be cycled for testing. For this experiment, the use of a dedicated force sensor and piezo electric motor was expected to surpass the rate limitations of the AFM. The ability to apply a known contact force in

addition to known current enables greater accuracy for determining micro-contact resistance and is the reason that AFMs are employed for testing. By using a piezo motor with a high-rate capable force sensor instead of an AFM, there was no expected decrease in micro-contact resistance accuracy. Instead, the rate of micro-contact testing was only limited to the capability of the piezo controller and data acquisition system, which was expected to be around 3kHz.

To witness the evolution of micro-contact performance, micro-contact resistance was examined. Micro-contact resistance is directly impacted by interface changes and is a measurable quantity. In literature, assuming contaminant free surfaces, contact resistance is typically a function of four factors: the total contact area, material hardness, impact velocity, and contact force. A change in any of the aforementioned factors can negatively impact performance. Other reasons for a decrease in performance are described as the development of surface contaminants, from oxide growth to the development of organic films. Thin film development is described as the leading cause for a decrease in micro-contact performance. However, these thin film developments change the performance of the micro-contact by changing the fundamental factors for micro-contact resistance which are effective contact area, material hardness, and underlying physics of conduction. Previously, the development of thin films on micro-contacts was experimentally verified as having an impact on micro-contact resistance. In this research, a systematic approach was taken to examine and describe thin film development as it relates to the evolution of micro-contact performance.

With micro-contact resistance as a valued parameter, the choice of contact material becomes an important determinant for performance. To achieve the specific goal of comparing the performance of various contact material types and develop predictors for

micro-contact performance based on material choice, a repeat of Holm's crossed rod experiment was performed for each material. Holm recorded the contact resistance as a function of applied force for various materials; he also noted that for each material, there was a deviation in contact resistance due to a film on the materials tested. For this research, Holm's experiment was repeated for each material with sufficiently small contact load in order to produce a contact area by elastic loading.

3.3 Test Fixture to Examine Lifetime Performance Characteristics

Examining lifetime performance characteristics of micro-contacts requires a record of applied contact force, current, and contact resistance while dry circuit testing. Dry circuit testing provides for the measurement of contact resistance under very low levels of electrical excitation, with applied currents selected to be too low to cause breakdown of thin oxide films or other contaminates in the contact interface. The use of a four point measurement allows the voltage drop due only to the contact resistance of the sample to be measured. In dry circuit conditions, the current is limited to 100 milliamps and open circuit voltage to 20 mV. As previously mentioned, the test fixture for this research is unique compared to previous setups due to faster rate of cycling micro-contacts with a known force. This setup required the use of an automated data acquisition software program in Lab View and a physical test stand in which to house the sample, force sensor, and motor.

3.3.1 Lab View

There are three types of contact testing which must be performed in order to characterize the evolution of performance for a micro-contact: virgin contact testing, hot switching, and cold switching. Virgin contact testing enables the determination of the

67

appropriate contact force to be applied for reasonably low resistance. The applied contact force determined by the virgin contact test is then used for hot switching and cold switching tests. Hot switching, as mentioned in chapter II, subjects the micro-contact to more failure modes by cycling the micro-contact with constantly applied current. Cold switching, on the other hand, reduces the failure modes to physical failure modes and only applies current during the time that the micro-contact is actuated closed. Combined, the three aforementioned tests can characterize the evolution of micro-contact performance. Appendix A contains screenshots and an explanation of the graphically oriented code.

3.3.2 Virgin Contact Testing

The virgin contact test applies a load to the micro-contact and determines the amount of force needed for the micro-surfaces to be in contact. This applied force, required for a closed connection, is marked as the offset for applied contact force. All force to be applied from the offset is then the true applied micro-contact force. The Lab View program, specifically the virgin contact test, was designed for the user to input a step size in nanometers, a maximum applied force in micro-Newtons, and time interval at each step in milliseconds.

In order to test the micro-contact, the virgin contact test was applied for every cycle where a measurement was required. The user set the appropriate step size, time interval, and maximum applied force and then the system incremented the force sensor in the set step size until the force sensor limit was reached. At each increment, voltage, current, and force are recorded.

3.3.3 Hot-Switch Testing

The hot-switch test applies a given current while actuating the micro-contact open and closed for a given number of iterations. The user is required to input the position of desired contact force, the maximum applied contact force, the number of cycles, the applied current, as well as the number of cycles between measurements. With the given information, the program applies the set level of current and actuates the micro-contact open and closed for the set number of cycles. On the cycle for which a measurement is to be made, the current, voltage, and applied force is recorded and placed in an excel file.

3.3.4 Cold-Switch Testing

Using the information from the virgin contact test, the user may opt to perform a cold-switch test instead of the hot-switch test. Cold-switching, as stated earlier, promotes the failure of the micro-contact by mechanical failures by reducing the probability of electrical failure modes. While the inputs the user must provide are similar to the hot-switch test, the method of test is different in a significant way. For the cold-switch program, the micro-contact is first closed before current is applied. With the contact closed, the desired current level is applied to the micro-contact and the measurement of micro-contact current and voltage is then made. After the measurement of current and voltage, the applied current is then turned off and the micro-contact is opened. These steps are then repeated for the desired number of cycles.

3.3.5 Test Stand

The test stand for this research is made of several components to enable characterization of the performance evolution of a micro-contact over its lifetime. One requirement is the ability for visual confirmation of a force sensor in contact with a micro-contact test structure. Another necessity is an enclosed space for a nitrogen environment in which to test the micro-contact. Two Agilent 34410A multi-meters are used to measure the current and voltage across the micro-contact. An Agilent U3606A current source is required to apply current to the micro-contact structure. A Femto Tools FT-S270 force sensor is used to determine the amount of force applied to the micro-contact test structure. In order to apply force to the micro-contact, a Thorlabs BPC301 piezo motor and controller is needed to move the sensor away and to the micro-contact test structure. An Agilent 33250A waveform generator is programmed to supply the driving signal to the piezo actuator for high cycle rate testing. Micromanipulators are necessary for positioning the force sensor in alignment to the micro-contact test structure. In addition, the micro-contact test structure, which is on a silicon wafer, is placed on a carrier and fixed into place to allow for proper alignment and testing with the force sensor. To integrate these components into one system, a computer with Lab View and a GPIB interface is used.

Beginning with the micro-test structure fixture, a fabricated device on a wafer is glued to a carrier. The micro-contact test structure is then wire bonded to the breakouts of the carrier to make it easier to measure the current and voltage across the contact. This also reduces the probability of physically interacting and changing the surface of the micro-contact test structure by removing the necessity for probes. With the wafer wire bonded to the carrier, the carrier is then placed into the carrier socket which has pins for every wire

70

bond. These pins are wire wrapped separately and the wires are guided outside of the

enclosed test fixture. The carrier socket is fixed vertically into place by a metal bracket

attached to a z-axis micro-manipulator. The manipulator is fixed to the bottom of the

enclosed test fixture to prohibit movement in the x or y axis direction.
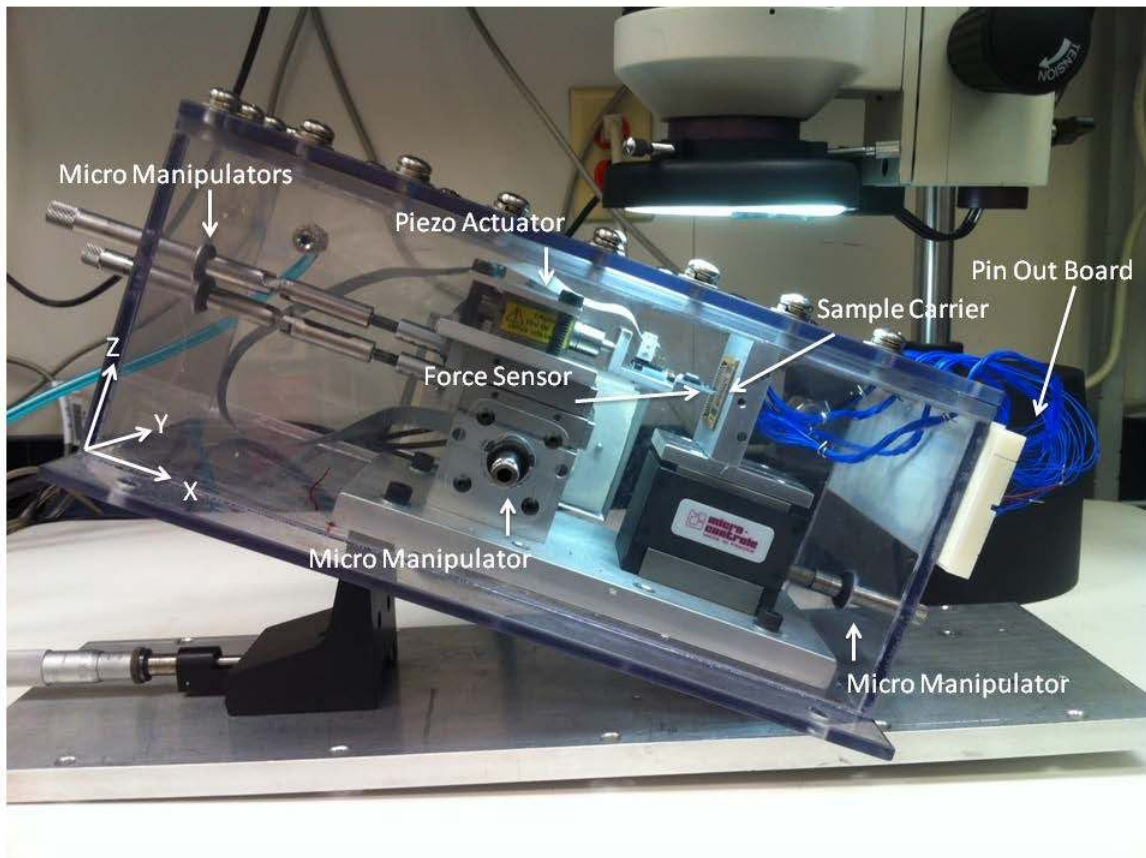
Figure 20 Test Stand

Also fixed to the enclosed test fixture are two x-axis micro-manipulators and one y-

axis micro-manipulator opposite the z-axis micro-manipulator. These x-axis manipulators

are fixed into place to prevent any movement in the y and z axis direction.   The y-axis

micro-manipulator allows for alignment in the y-axis direction. The piezo motor is attached

to the two x-axis and one y-axis micro-manipulators. The piezo motor is fixed into place to

allow movement solely in the x-axis direction. The force sensor is attached to the piezo

71

motor. As shown in Figure 20, the force sensor, piezo motor, and x-axis and y-axis micro-manipulators are stacked to allow the force sensor to be aligned with and actuate the micro-contact test structure in the carrier.

The enclosed test fixture provides the ability to create a nitrogen environment. Testing in a nitrogen environment reduces the opportunity for oxides and other organic films to develop prematurely. The nitrogen environment is created to simulate a hermetic environment that a micro-contact would normally perform in. This test fixture allows for the knobs of all the micro-manipulators as well as the wires attached to the carrier socket to be accessible from outside the fixture as shown in Figure 20.

**3.4 Micro-Contact Support Structures for Lifecycle Testing**

In order to examine micro-contact lifecycle phenomena, two structures were developed which emphasize studying the failure modes of micro-contacts. The first structure emulates Holm's crossed bar experiment by allowing a four-wire measurement, in which current flows strictly through the micro-contact and voltage is measured independently across the micro-contact simultaneously. The second structure was originally designed for electrostatic actuation and takes advantage of the PolyMUMPs fabrication process. Its design proves useful for examining the contact area by allowing the contact to be 'flipped' open.

3.4.1 Fixed-Fixed Beam Micro-Contact Structure

As mentioned previously, the fixed-fixed beam micro-contact structure emulates Holm's crossed bar experiment on the micro-scale. This design allows a four-wire

measurement in which current only flows through the micro-contact interface. Voltage is then measured across the micro-contact via gold traces connected to the anchor of the beam and micro-contact area.

Fixed-fixed beams all with a width of 250 µm are designed in the following lengths: 300 µm, 350 µm, 400 µm, 450 µm, and 500 µm. The beams are designed with a gap of 1 µm between the contact bump and contact pad. Sets of beams in each length are fabricated where the contact bump radius ranges from 2 µm, 4 µm, 6 µm, 8 µm, and 10 µm. Sets of beams are also fabricated for each length and each contact bump radius which vary the number of contact bumps from one bump, two bumps, and three bumps. Figure 21 shows a 3D model of the fixed-fixed beam micro-contact structure.
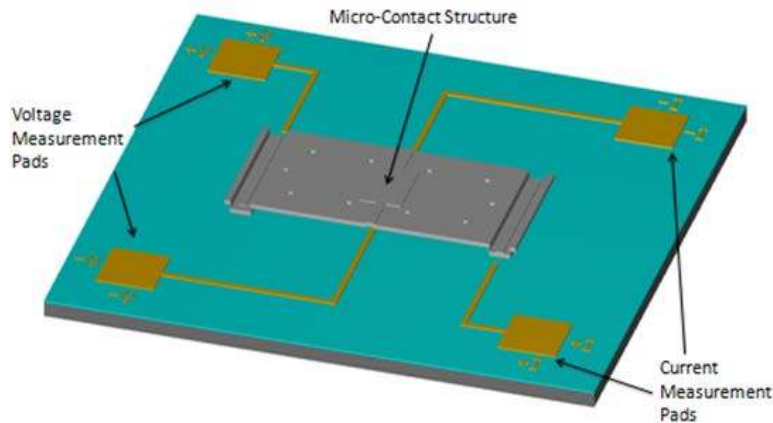
Figure 21 3D model of Fixed-Fixed Beam Micro-Contact Structure

The micro-contact structure is constructed for gold-gold micro-contact and utilizes a structural layer to enhance the micro-contact structure's stiffness and reduce the risk of stiction but can be easily modified to investigate other contact materials. The advantage of the micro-contact structure's architecture is the ability to fabricate structures with different micro-contact materials to investigate the properties and physics of various contact materials

73

and or structural layer materials to increase or decrease the beam stiffness to account for adhesion. In addition to fabricating entirely gold micro-contact support structures, structures using structural layer materials such as silver colloids, molybdenum, and CNTs were fabricated.

Silver colloids were added to the beam structure of the device by 'encasing' them by sputtering a layer of gold for the contact, applying the colloids, and electroplating gold over them. To remove any confusion, the resultant device is not an Ag-Au or alloy type structure; it is an Au structure with encapsulated Ag colloids but for the purposes of this document will be here on referred to as the Ag-Au beam. Figure 22 shows an example diagram of an Ag-Au device cross-section. The silver colloids can, in effect, change the paths of conduction through the beam since the beam is no longer uniform. As seen in the literature review, namely Figure 14, creating a structure with two different metals does not always produce an alloy or composite which has better or even comparable performance as the metals do individually.

Figure 22 Example Diagram of Ag-Au Beam

By itself, silver is a better conductor than gold, both thermally and electrically. After deposition of the colloids, a thermal image was taken to demonstrate the thermal conductivity of Ag colloids. The addition of colloids may not only enhance the thermal conductivity of the micro-contact support structure, which would help maintain lower contact temperatures, but increase the stiffness of the beam which could act as a

74

countermeasure to stiction. Despite silver having a lower resistivity, a potential drawback to the design is the increased resistivity due to the Ag colloids changing the conducting paths of the electrons. As can be seen by Figure 23, the more readily identifiable Ag Colloid groupings or 'clumps' appear as bright white, indicating better thermal conduction than the dark blue nitride coated silicon substrate and Au bottom metal layer.
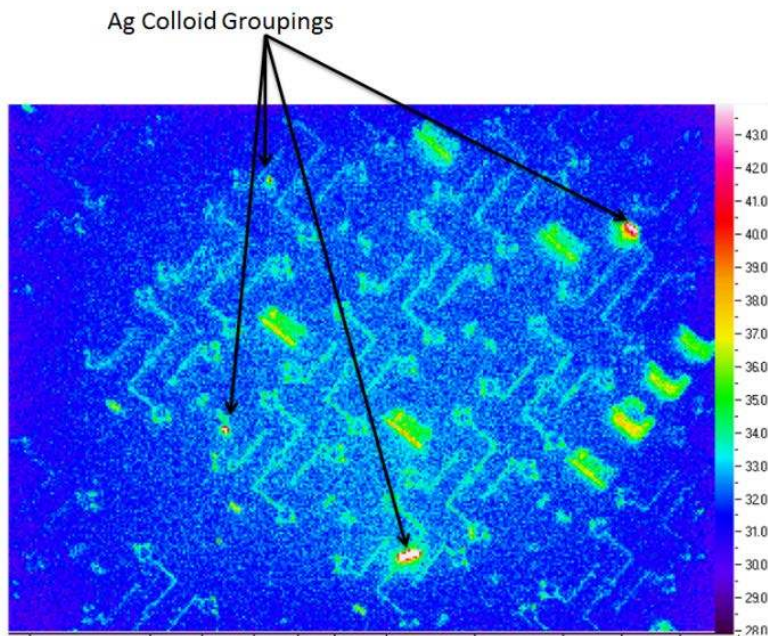
Figure 23Thermal Image of Ag Colloids with sample heated to 60C

Similarly, CNTs are added in the same fashion as the Ag colloids in a separate device. Figure 24 shows the result of thermal imaging a CNT 'covered' sample heated. As was the case for the Ag colloids, the CNT groupings conduct heat better than the other elements in the design. This is evident by the bright green and red spots shown in the figure.
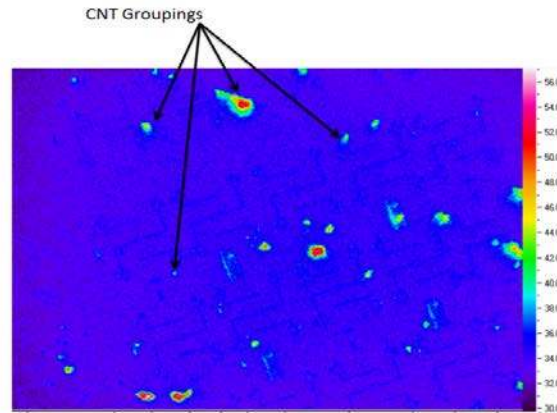
Figure 24 Thermal Image of CNT 'clumps' with sample heated to 60C

In order to calculate the Young's modulus of the multilayer micro-contact structure, the weighted average of each material's Young's modulus was taken where applicable. To determine the appropriate thickness of the micro-contact structure, Table 2 was developed using equation 30 and equation 31 in order to determine the required force to make contact given the 1 µm gap and various lengths and thicknesses of beams.

Table 2 Force Required to Close the 1 µm Gap for fixed-fixed beams of Au

Force (uN) to Close Gap	Lengths (um)				
Thickness (um)	300	350	400	450	500
2.3	142.399	89.674	60.075	42.192	30.758
2.4	161.792	101.887	68.256	47.938	34.947
2.5	182.870	115.160	77.148	54.184	39.500
2.6	205.704	129.540	86.782	60.949	44.432
2.7	230.364	145.069	97.185	68.256	49.759
2.8	256.920	161.792	108.388	76.124	55.495
2.9	285.442	179.753	120.421	84.575	61.655

Table 3 was also developed using equation 30 and equation 31 in order to determine the required force to make contact given the 1 µm gap and various lengths and thicknesses of beams. Knowing the force required to make contact allows for the proper settings in Lab View to be used in order to apply the appropriate amount of contact force.

Table 3 Force Required to Close the 1 µm Gap for fixed-fixed beams of Au-Mo

| Au (um)	Mo (um)	Force (uN) to Close Gap Beam Thickness	Length (um) 300	350	400	450	500
0.2	0.1	0.3	0.64	0.40	0.27	0.19	0.14
0.2	0.2	0.4	1.89	1.19	0.80	0.56	0.41
0.2	0.3	0.5	4.14	2.61	1.75	1.23	0.89
0.2	0.4	0.6	7.67	4.83	3.24	2.27	1.66
0.2	0.5	0.7	12.76	8.04	5.38	3.78	2.76
0.2	0.6	0.8	19.70	12.41	8.31	5.84	4.26
0.2	0.7	0.9	28.78	18.12	12.14	8.53	6.22
0.2	0.8	1.0	40.27	25.36	16.99	11.93	8.70
0.2	0.9	1.1	54.46	34.29	22.97	16.14	11.76
0.2	1.0	1.2	71.64	45.11	30.22	21.23	15.47
0.2	1.1	1.3	92.09	57.99	38.85	27.28	19.89
0.2	1.2	1.4	116.09	73.11	48.98	34.40	25.08
0.2	1.3	1.5	143.93	90.64	60.72	42.65	31.09
0.2	1.4	1.6	175.90	110.77	74.21	52.12	37.99
0.2	1.5	1.7	212.28	133.68	89.55	62.90	45.85
0.2	1.6	1.8	253.34	159.54	106.88	75.06	54.72
0.2	1.7	1.9	299.39	188.54	126.30	88.71	64.67
0.2	1.8	2.0	350.70	220.85	147.95	103.91	75.75
0.2	1.9	2.1	407.55	256.65	171.93	120.76	88.03
0.2	2.0	2.2	470.23	296.12	198.38	139.33	101.57

Figure 25 shows the required force to deflect an Au only fixed-fixed beam with thickness of 2.7 µm and length of 450 µm; the expected thickness of the beam after electroplating, etch back, and release. The force range necessary for contact make is shown on the figure because of the variations in thicknesses possible due to fabrication techniques. For example, electroplating is not uniform across the surface of the wafer but can vary by 300 nm. In addition to variances in electroplated thicknesses, the etching of the gold can vary based on time and agitation of the etchant while the wafer is submerged.
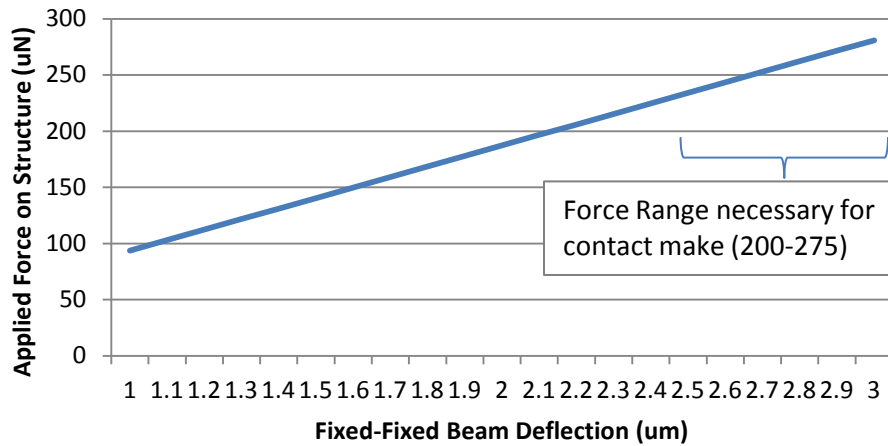
Figure 25 Applied Force on Fixed-Fixed Beam for Contact Make

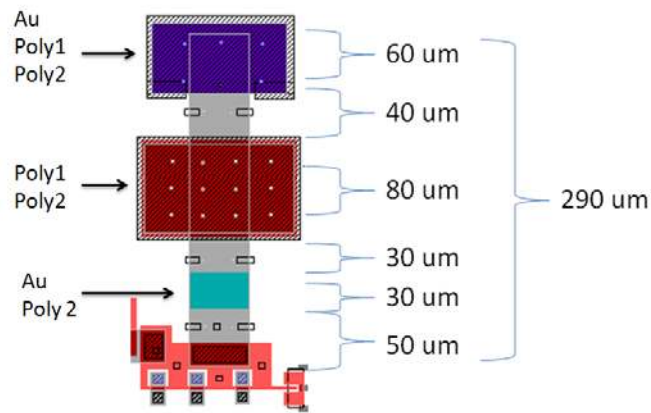### 3.4.2 PolyMUMPs Flip-Switch Micro-Contact Structure

Originally designed for electrostatic actuation, the design is suitable for the study of micro-contact failure modes since the micro-contact can easily be examined by 'flipping' the contact back to the state shown in Figure 26 once the testing is complete. Figure 26 shows a 3D model of the PolyMUMPs flip-switch micro-contact structure in the pre-released state. After the device has been fabricated at the PolyMUMPs foundry, the device is coated with a protected layer of photoresist which must be removed; the device is 'released' when the oxide layers are etched away. The removal of the protective layer and oxides will allow for the residual stress in the long gold beam next to the flip-switch to 'flip' the switch over into a micro-contact testable state.
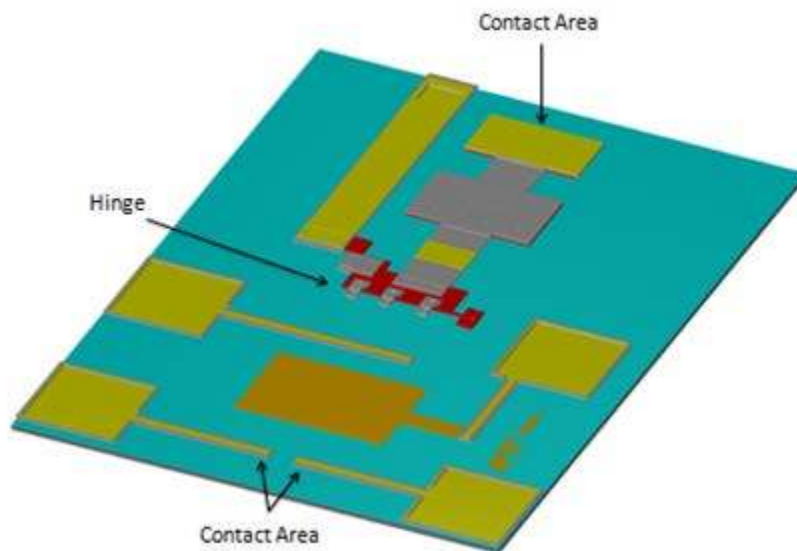
Figure 26 3D model of PolyMUMPs Flip-Switch Micro-Contact Structure

In order to determine the force required to close the gap for this micro-contact structure, which is expected to be 8 µm, the average of the beam's thickness was used for

determination of the moment of inertia. Figure 27 shows the layout of the PolyMUMPs flip-switch micro-contact structure. The force required for deflection was calculated by analytical modeling the PolyMUMPs flip-switch micro-contact structure as a fixed cantilever.

Figure 27 PolyMUMPs Flip-Switch Layout

Table 4 shows that an applied force of 9 µN will cause micro-contact make by closing the gap.

Table 4 Deflection as a Function of Force for PolyMUMPs Flip-Switch Micro-Contact Structure

| Applied Force (uN)	Deflection (um)
1	0.90
2	1.80
3	2.70
4	3.60
5	4.50
6	5.40
7	6.31
8	7.21
9	8.11
10	9.01

3.5 Examination of Micro-Contact Physics

3.5.1 Analytic

As previously mentioned, the micro-contact resistance is the parameter being used to characterize the evolution of the performance of the micro-contact over its lifetime. Micro-contact resistance is used due to its fundamental factors which are effective contact area, material hardness, and underlying physics of conduction. From the literature review, asperities on the surface of two materials are the first to make initial contact and allow current to flow through the micro-contact. For simplified contact resistance calculations, the effective contact radius is used. The effective contact radius changes based on elastic, elastic-plastic, and plastic deformations caused by the applied force. For micro-contacts, consideration of the electron's elastic mean free path l_e compared to the effective radius r_{eff} is important for determining the appropriate analytical contact resistance equation. If the elastic mean free path is greater than the effective contact radius, $l_e > r_{eff}$ then electrons are transported ballistically through the contact materials [27]. Alternatively, if $l_e \ll r_{eff}$ then electrons are transported diffusively [27]. For an analytical prediction of contact resistance as a function of force, both micro-contact structures have effective contact areas much greater than the elastic mean free path, therefore, Holm's contact resistance for elastic deformation and diffusive electron transport is used.

$$R_{cDE} = \frac{\rho}{2} \sqrt{\frac{H\pi}{F_c}} \tag{43}$$

where ρ is the resistivity of the conducting material, H is the hardness of the material, F_c is the contact force. Figure 28 shows the predicted analytical contact resistance for the fixed-fixed micro-contact structure's Au-Au micro-contact based on

81

diffusive electron transport and elastic deformation with the assumption of a simplified

contact area and no contaminant films. Likewise, Figure 29, Figure 30, and Figure 30

show the contact resistance prediction for structures comprised of various contact
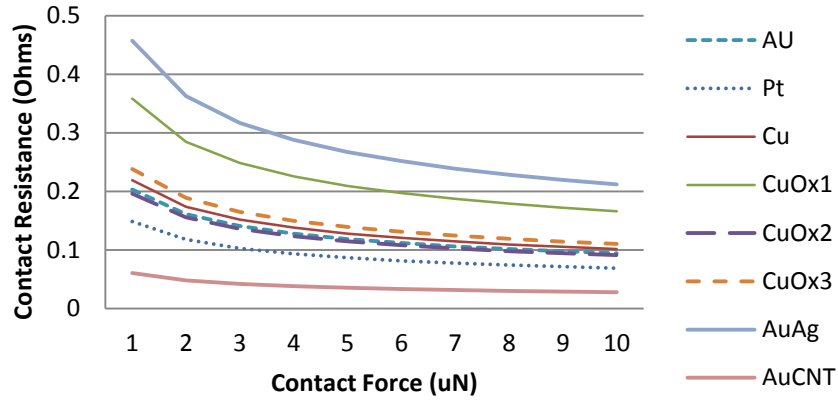
materials.
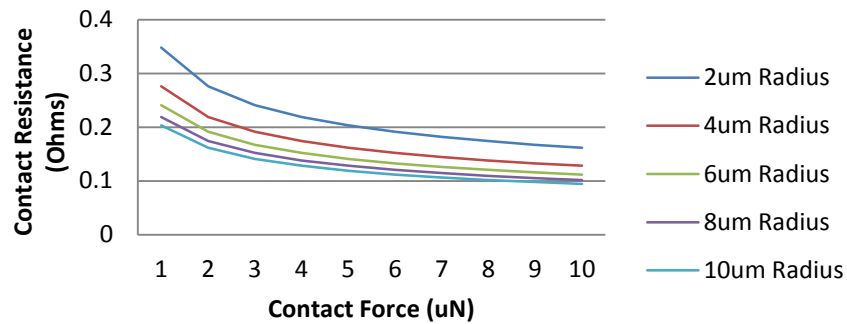
Figure 28 Contact Resistance Prediction for Fixed-Fixed Au Micro-Contact Structure
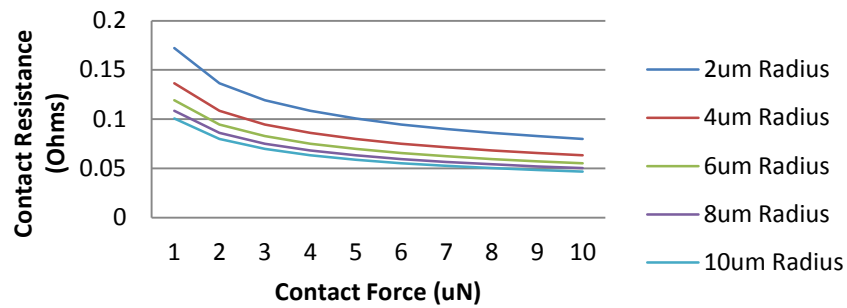
Figure 29 Contact Resistance Prediction for Fixed-Fixed Ag-Au Micro-Contact Structure

Figure 30 shows the contact resistance prediction for structures comprised of

various contact materials for a specified contact radius of 10 µm.

Figure 30 Contact Resistance Prediction for Various Contact Material Candidates

Changes to the material properties, namely the development of an insulating film, will bring the micro-contact to failure. Causes for the development of insulating films remain controversial and unknown in literature. The development of an insulating film indicates a change in micro-contact material chemistry. Should the film be the product of an electrochemical reaction of oxidation or reduction, the root cause for film development would appear to be corrosion.

In electrochemistry, all electron-transfer reactions are considered oxidation and reduction processes, which do not limit the use of the term to reactions with oxygen; even though oxidation is most commonly associated with oxygen reactants. Corrosion consists of the two processes: oxidation and reduction. Corrosion is determined by two factors, driving force, which is the difference in potential between anodic and cathodic sites, and kinetics, the rate of corrosion. The difference in potential between the anode and cathode of a micro-contact can be influenced by the use of electrostatic actuation and hot switching. The potential is a measure of the tendency for the reaction to take place spontaneously. The rate of corrosion is determined through the use of polarization measurements. The performance

of micro-contacts may only be limited to the rate of corrosion and tendency of spontaneous reaction since the potential difference between the surfaces of the micro-contact and number of actuations directly influence both electrochemical corrosion processes.

3.5.2 Physical and Chemical Phenomena

To examine the physical and chemical phenomena after testing, the micro-contact test structure was carefully broken in order to allow examination of the micro-contact surfaces. An inspection was performed in order to determine the development of any organic films as well as changes in the topology of the micro-contact. The topology of the micro-contact was examined under a scanning-electron microscope (SEM).

A test using an INCA x-sight Energy dispersive X-ray spectroscopy (EDS) Detector (Oxford Instruments) was conducted on a control group of micro-contact structures to baseline a quantifiable description of the chemical make-up of the micro-contact surface. Upon completion of testing on the experimental group of micro-contact support structures, the experimental group was examined to see if the chemical composition had remained unchanged. If the chemical composition had changed, this would indicate a development of some material which increases the micro-contact resistance and causes the performance of the micro-contact to wane.

After the micro-contact support structures were fabricated, a control was examined under a SEM to image the surface of a micro-contact before it had been cycled to failure. Upon completion of the cold-switched test groups, those groups were imaged under an SEM. The SEM images were then visually inspected for any noticeable changes in the micro-contact structures.

3.6 Summary

This chapter details the methodology for the design, fabrication, and testing for this research. A comparison of the research goals to previous works is shown. The test fixture used to examine the lifetime performance characteristics is described; to include an overview of the lab view programming required, explanation of the virgin, hot-switch, and cold-switch test, as well as the physical description of the test stand. Micro-contact structures for micro-contact lifecycle testing were characterized and the force required to make contact was analytically calculated. An examination of the micro-contact physics is performed to show the predicted micro-contact resistance by classical resistance theory. Physical phenomena and a description of the tests performed to verify and examine physical changes on the micro-contact are given.

# IV. Analysis and Results

4.1 Chapter Overview

To find an accurate description for the physical phenomena at the interface of the micro-contact, information gathered from the review of current micro-contact literature is compared with what was witnessed from the cold-switch tests. The following sections detail the testing of the fixed-fixed micro-contact support structures and PolyMUMPs micro-contact support structure. The goal was to notionally test as many of the 75 varieties of fixed-fixed micro-contact support structures as possible for comparisons between beam lengths, micro-contact radii, and number of micro-contacts to see which design would be most suitable for micro-contact lifetime characterization. However, once the devices were released, it was discovered that the micro-contact support structures were shorted at an average of 100Ω. The measurement of resistance where no resistance should have been measured indicated a flaw inherent in the fabrication method. Adjustments to the fabrication process then provided fully functioning micro-contact support structures. For preliminary data, despite being shorted, fixed-fixed micro-contact support structures of length 450µm, having three micro-contact bumps, and radii of 6, 8, and 10µm were tested using the µN force sensor at cycle rates up to 3 kHz. After fabrication was refined, three functioning fixed-fixed Au micro-contact support structures with contact radii of 4, 6, and 10 µm and two functioning fixed-fixed Ag micro-contacts were tested using the µN force sensor at cycle rates up to 3 kHz. Another goal was to compare the PolyMUMPs micro-contact support structure to the fixed-fixed micro-contact support structure to determine the best structure for studying the evolution of micro-contact resistance.

4.2 Experimental Results and Analysis
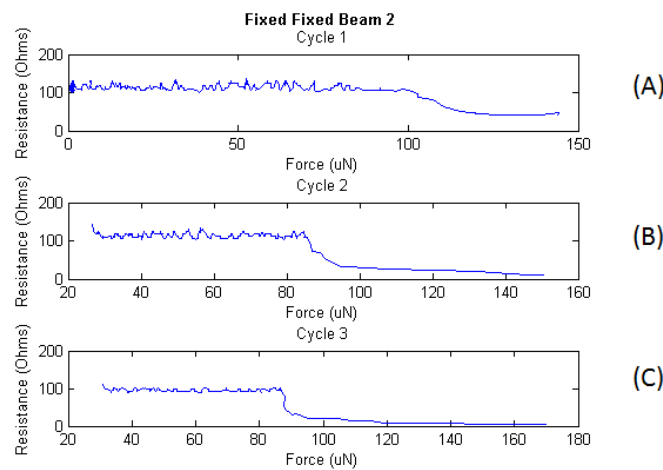
4.2.1 Virgin Contact Testing

4.2.1.1 Shorted Fixed-Fixed Au Micro-Contact Support Structure

As stated previously, the fixed-fixed micro-contact support structures were found to be shorted at an average of 100Ω. The devices ranged in thickness from 2.3 µm to 3 µm. The data from a single fixed-fixed micro-contact support structure is presented. Figure 31 displays the ideal trend for micro-contact resistance, based on Holm's contact resistance for elastic deformation and diffusive electron transport (42), as compared to the measured micro-contact resistance. As seen in the figure, the ideal micro-contact resistance measurement with no applied micro-contact force should begin at infinite (since contact is not made) and decrease sharply as contact is made and the applied contact force becomes greater. The measurement of resistance consistently at 110Ω between no applied force and near 100µN indicates the existence of a film preventing metal-to-metal contact.
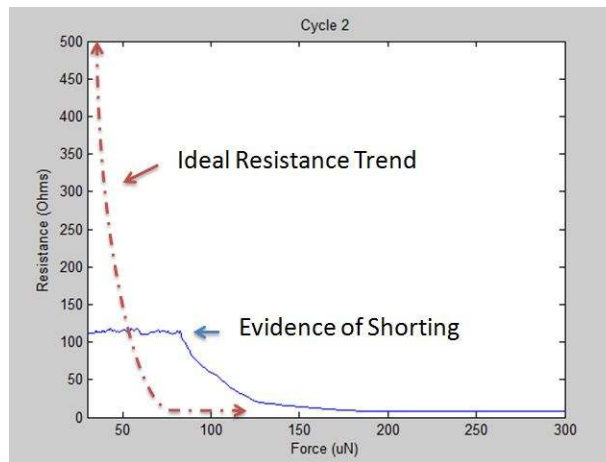
**Figure 31 VCT Measurement Revealing Shorted Micro-Contact Support Structure**

Figure 32 shows the virgin contact test data over three cycles for a single fixed-fixed Au micro-contact support structure 2.7µm thick. The claim of a contaminant film being present is supported by (A), (B), and (C) in Figure 32. In (A), the first actuation, the contaminant film is 'squeezed' near 100µN and resistance gradually drops to and then remains consistently near 50Ω. The next actuation, cycle two, shows that the required force to reduce resistance decreases from near 100µN to 85µN. (B) shows a sharper transition from the shorted resistance of 110Ω to less than 50Ω when compared to (A) in cycle one. This sharper transition in (B) aids the idea that the contaminant film is being fritted away by the contact bump grinding against it under pressure from the applied force.

Figure 32 Virgin Contact Test Data for Shorted Fixed Fixed Au Micro-Contact Support Structure

Again in (C), the transition from the initial resistance value to lower values is sharper than (B) and requires even less force to obtain. Also of note is that the contact resistance near the force limit of the test (150µN) was less than 1Ω Comparing the evolution of resistance from (A) to (B) to (C) substantiates the claim of a contaminant film (residual photoresist)

being present between the micro-contact surfaces (anode and cathode). Figure 33 provides a

visual representation of what is happening between cycles one, two, and three.
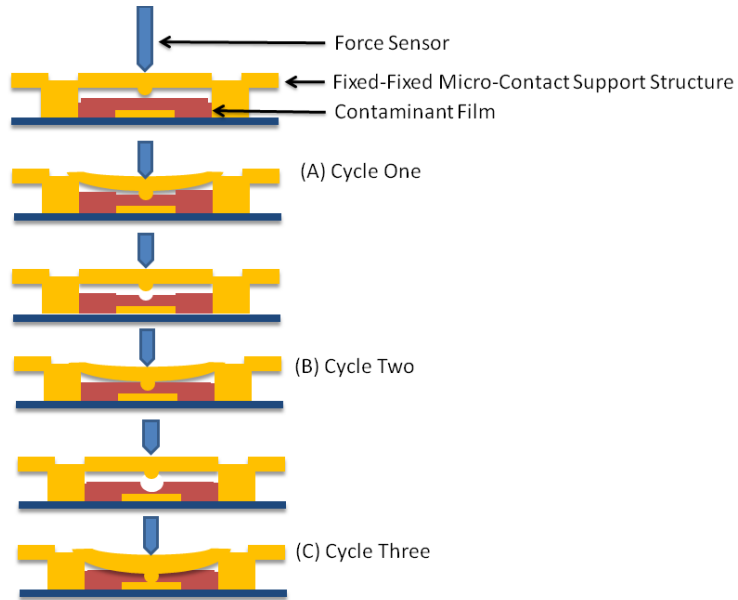
Figure 33 Visual Representation of Contaminant Film Fretting

<u>4.2.1.2 Functional Fixed-Fixed Au-Au Micro-Contact Support Structure</u>

After refining the fabrication process for the fixed-fixed Au-Au micro-contact support structure, three micro-contact structures were tested. While only one is presented in this section, the other two can be found in Appendix D. Figure 34 shows a comparison of the measured micro-contact resistance for an Au only fixed-fixed micro-contact support structure 2.7 µm thick with a contact radius of 10 µm and the predicted values of micro-contact resistance based on Holm's contact resistance for elastic deformation and diffusive electron transport. Variations between the modeled micro-contact resistance and measured results can be explained by the accuracy, precision, and performance of the test taking equipment; which will be discussed in further detail in a later section.
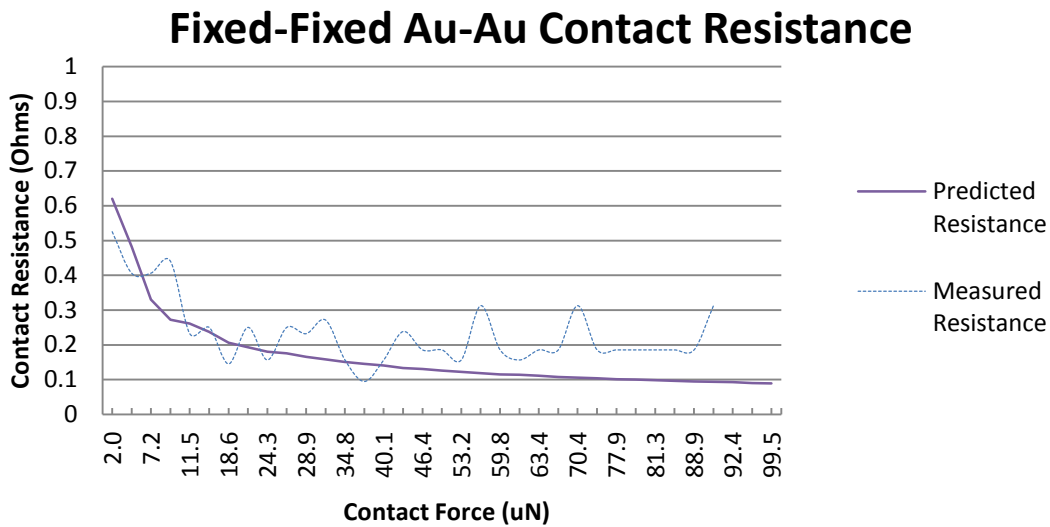
Fixed-Fixed Au-Au Contact Resistance

Figure 34 Predicted Resistance and Measured Resistance for Au-Au Micro-Contact

Figure 35 shows the VCT data for three cycles on a fixed-fixed Au-Au micro-contact support structure. As can be seen in the figure, the structure required approximately 140μN of force to make contact in cycle one. Over the next two cycles, the force required for contact make decreased.
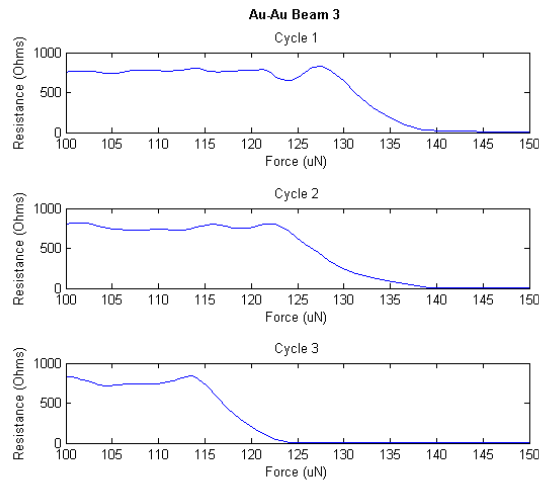
Figure 35 Au-Au Micro-Contact Support Structure VCT Data

In the previous examination of VCT data for a shorted fixed-fixed Au micro-contact support structure, the force required was also reduced with repeated actuation and there was an initial contact resistance up to the point of contact make. Unlike the previously shorted device, the functional fixed-fixed Au micro-contact support structure's beam topology may be changing due to the applied load and increased temperature from electrical conduction, thereby reducing the force required for contact make. The measured initial resistance is actually a resistor in parallel with the micro-contact support structure. Because of the operation of a current source in constant current mode, the voltage output of the current

91

source continues to vary in order to supply the set current. Therefore, if there is a change in resistance, the current source will adjust the voltage accordingly in order to maintain the preset value for current. In the event of an open circuit, the current source will raise the voltage until the voltage protection value (30V) is reached. At this value, once contact is made, there is an 'in-rush' of current which well exceeds the amount the micro-contact support structure can handle and remain operational. As can be seen in Figure 36, the bottom trace leading into the anchor of the fixed-fixed support structure is burned.
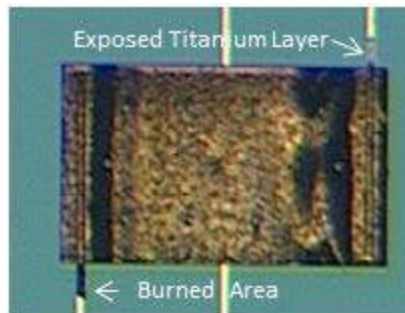
Figure 36 Evidence of In-Rush Current

To remedy this effect, a resistor of 750 Ω is placed in parallel in order to limit the voltage across the micro-contact at initial make and reduce the effect of in-rush current. With a parallel resistor in place, the measured contact resistance is the resistance equivalent of the circuit. However, since $R_c \ll 750\Omega$, the measured values of equivalent resistance remain within 0.5% of actual value until R_c is greater than 4Ω.

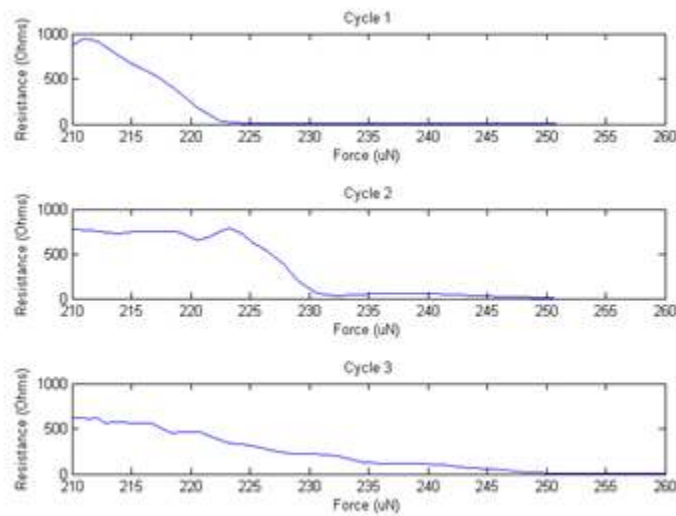## 4.2.1.3 Fixed-Fixed Mo-Au Micro-Contact Support Structure
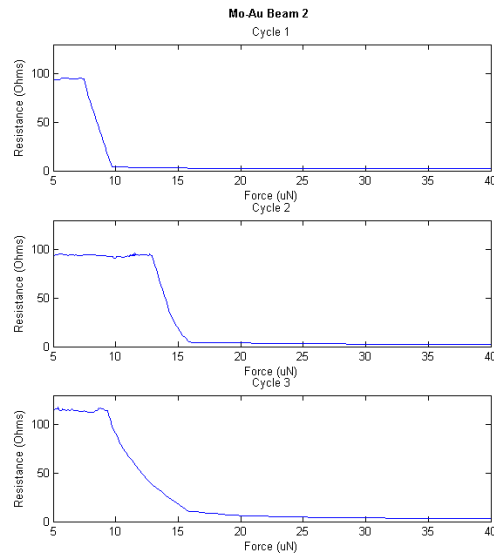
Figure 37 Mo-Au Micro-Contact Support Structure VCT Data

Figure 37 shows the VCT data for three cycles on a fixed-fixed micro-contact support structure fabricated with molybdenum (Mo). The Mo was added as a structural layer with the intention of enhancing the fixed-fixed beam stiffness. Because of processing difficulties, the Mo did not adhere to the Au surface of the beam uniformly as evident in Figure 38. Referring back to Figure 37, the structure required less than 10μN in order to potentially establish metal to metal contact. In the second cycle, the force required to make metal to metal contact increased by 5μN. The increase in the required force between cycle one and cycle two can likely be attributed to the uneven geometry of the micro-contact support structure; which may have changed with the applied force from cycle one. The force required for contact make reduced again in cycle three, supporting the claim of uneven support structure geometry.

93

Figure 38 Mo-Au Micro-Contact Support Structure

4.2.1.4 Fixed-Fixed Ag-Au Micro-Contact Support Structure

Figure 39 Ag-Au Micro-Contact Support Structure VCT Data

Figure 39 shows the VCT data for the first three cycles of the Ag-Au micro-contact. While the data may resemble that of the devices that were shorted, the initial contact resistance is the 750Ω parallel resistor. At contact make, the measured contact resistance lowers to 50Ω. In comparison with Figure 40, the predicted contact resistance, the measure value is different by two orders of magnitude. This difference may be explained by the geometry of the beam as shown in Figure 41. A notable difference in the micro-contact support structure depicted in Figure 41 and Figure 36 is that the bottom trace leading to the

94

anchors of the micro-contact support structure are not an exposed titanium layer but rather electroplated gold; allowing current to flow unimpeded.
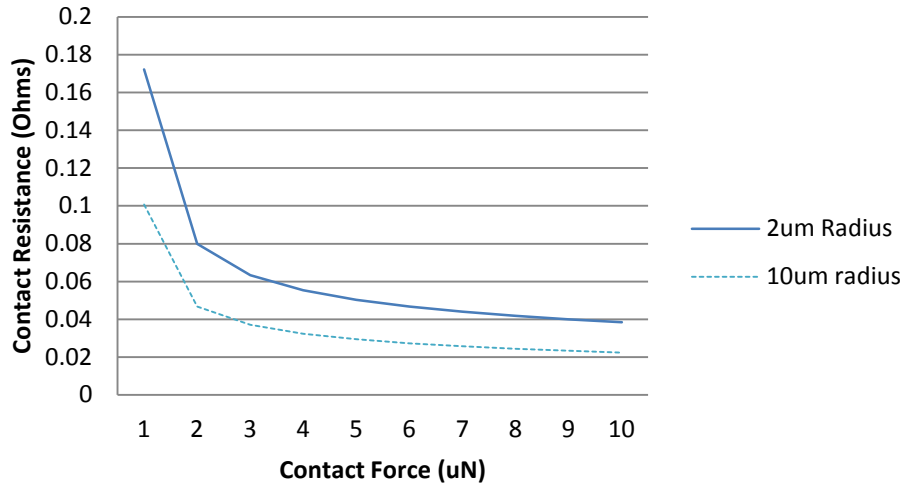

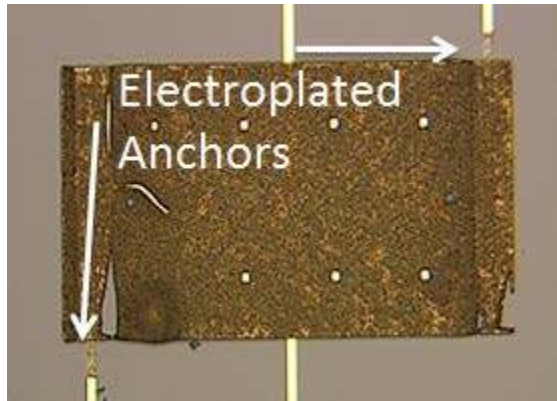**Figure 40 Predicted Contact Resistance for Ag-Au Micro-Contact Support Structure**
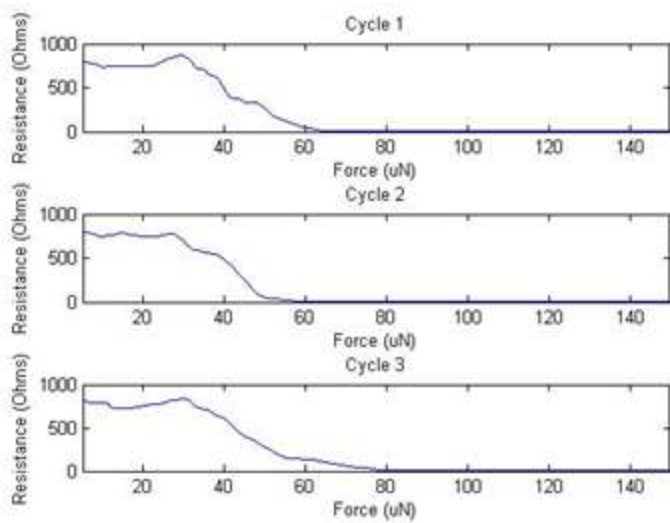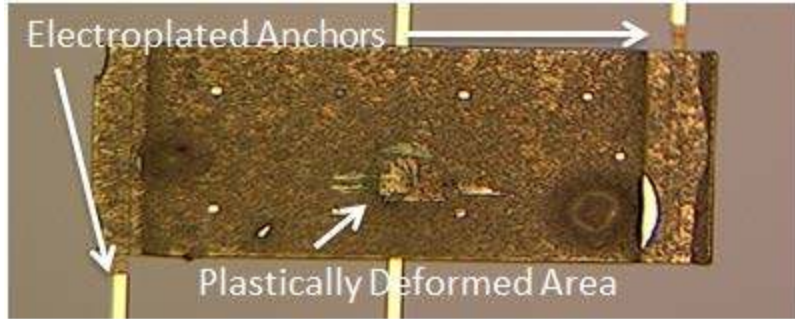

Figure 41 Pre-Tested Ag-Au Micro-Contact Support Structure

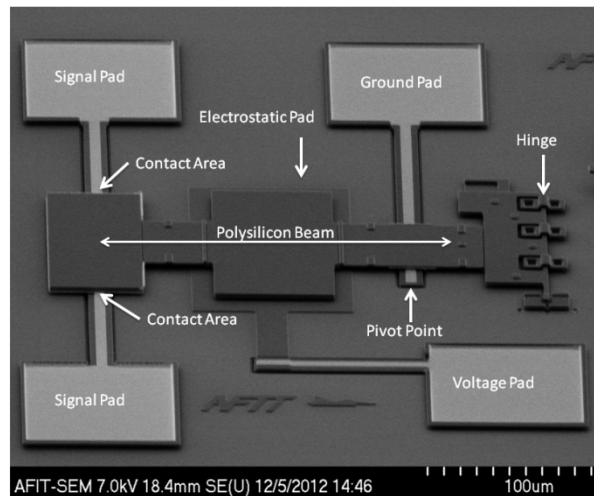**Figure 42 Ag-Au Micro-Contact Support Structure Beam Two VCT Data**

Figure 42 shows the VCT data for the second Ag-Au micro-contact support structure which was tested. As can be seen by the figure, the force required for contact was less than Ag-Au structure one. This may be caused by the gold etch step of the fabrication process, where devices on different areas of the wafer being processed can experience small variations in etch rate and exposure to the etchant. That would cause the thickness of the micro-contact support structure's beam to be thinner and require less force for actuation. The closed contact resistance for this device at 100µN's of contact force was 0.185Ω. By comparing the contact resistance of Ag-Au micro-contact support structure two with Figure 40, the predicted contact resistance for 10µm radius, it is apparent that the measured resistance and the predicted resistance are not closely matched until the contact force exceeds 40µN's. This discrepancy can be due to an under developed micro-contact bump. The development of a micro-contact bump is sensitive to variations in patterning and developing the photoresist prior to sputtering the contact metal; mask alignment, exposure time, and developing time all can impact the shape and size of the micro-contact.

96

Figure 43 Post-Test Ag-Au Micro-Contact Support Structure Two

Figure 43 shows Ag-Au micro-contact support structure two after being tested. From the image shown, it is obvious to see where the sensor made contact with the support structure and scuffed the surface during alignment. Less likely discernible from the image is that the structure is plastically deformed in that particular region from excessive force on the 2.6 µm thin Ag-Au beam.
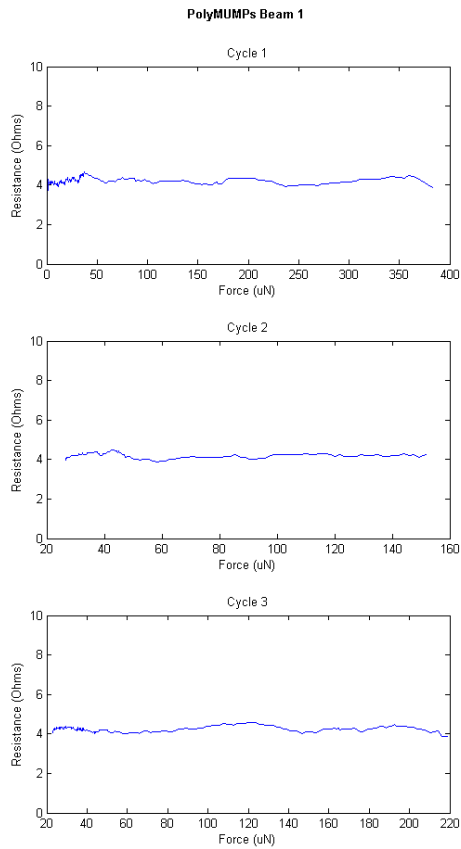
4.2.1.4 PolyMUMPs Micro-Contact Structure

Figure 44 PolyMUMPs Micro-Contact Support Structure

Figure 44 shows the fabricated PolyMUMPs micro-contact support structure used for testing. During testing, the force was applied on the center of the beam above the signal path. The micro-contact support structure was designed to allow an examination of the upper and lower

micro-contact areas by 'flipping' the beam over via the hinge. The PolyMUMPs micro-contact support structures, which were fabricated at a foundry, were defective due to residual stresses during the fabrication process. The residual stresses of the foundry's processes caused the polysilicon beam to curl over the pivot point forcing the contact to be made: effectively rendering the beam shorted. Figure 45 shows the recorded VCT data. The consistently low contact resistance from zero applied force to forces in excess of 140μN gives evidence that the structure is shorted.
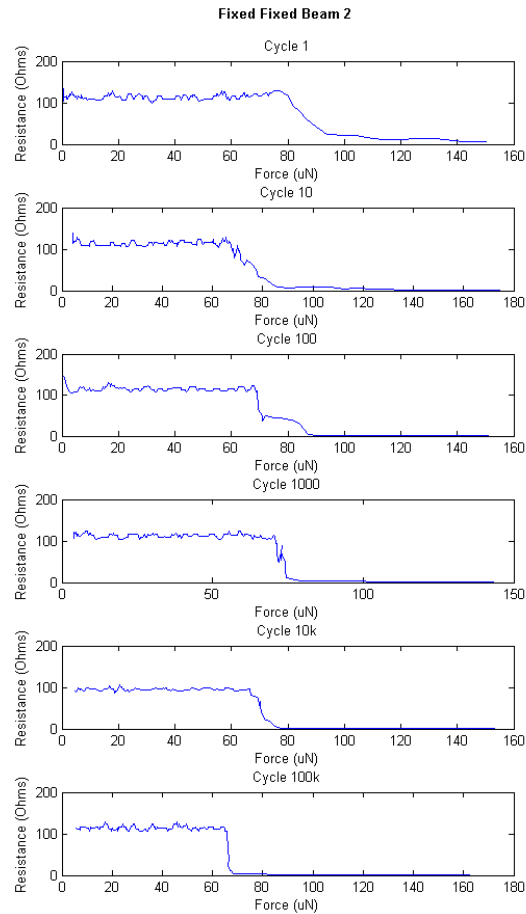

**Figure 45 PolyMUMPs VCT Data**

4.2.2 Cold-Switch Testing

Figure 46 Shorted Fixed-Fixed Au Micro-Contact Structure Cold-Switch Testing Data

For cold-switching, the device under test was first cycled up to 100 times at 10Hz with measurements taken at every 10 cycles. Following the initial 100 cycles, the device was actuated up to 1,000 cycles at 100Hz with measurements performed every 100 cycles. Then 10,000 cycles at 1kHz with measurements every 1,000 cycles. Lastly, the micro-contact structure was actuated to 100,000 cycles at 3kHz with measurements every 10,000

99

cycles. As was discussed in the analysis of the VCT data for the fixed-fixed micro-contact structure, the cold-switch results indicate that the contaminant film which was existent fritted away allowing metal to metal contact at lower and lower levels of applied force. Cycle 1 indicates the squeezing of the contaminant film and cycle 10 indicates the contaminant film is still present but is reduced in the micro-contact area. Cycle 100 shows a relatively steep drop in contact resistance but a higher contact resistance at 80µN than in cycle 10. To explain this phenomenon, the contaminant film is fritting away after the micro-contact support structure is repeatedly actuated, pieces of residual fretted contaminant film may get shifted into the contact area; causing the increase in contact resistance where previous cycles did not. Figure 47 shows the comparison of cycle 100 to 100,000, with visual representations of the contact area containing residual fretted contaminant film and with a clearer contact area.
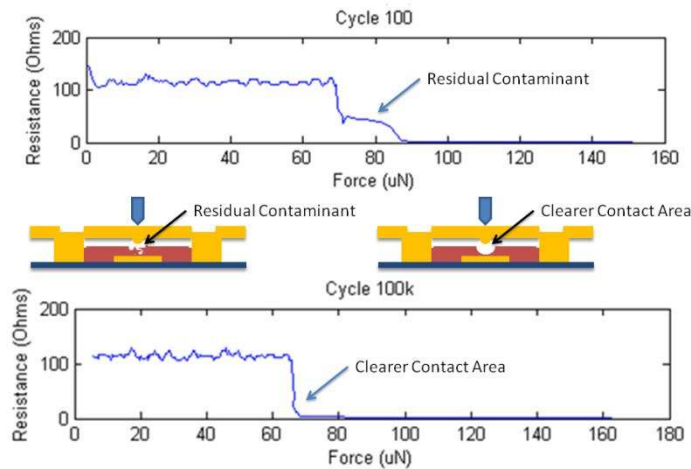
Figure 47 Contaminant Film Comparison Between Cycle 100 and Cycle 100,000

100

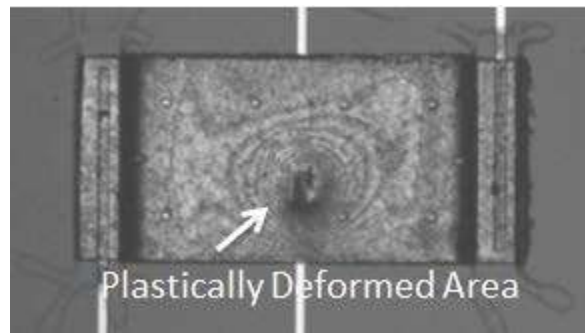### 4.2.2.2 Functional Fixed-Fixed Au Micro-Contact Structure

Similar to the shorted fixed-fixed Au micro-contact structure, the device under test was first cycled up to 100 times at 10Hz with measurements taken at every 10 cycles. Following the initial 100 cycles, the device was actuated up to 1,000 cycles at 100Hz with measurements performed every 100 cycles. Then 10,000 cycles at 1kHz with measurements every 1,000 cycles. In addition, the micro-contact structure was actuated to 100,000 cycles at 3kHz with measurements every 10,000 cycles. Lastly, the device was actuated to failure with measurements at every 100,000 cycles.
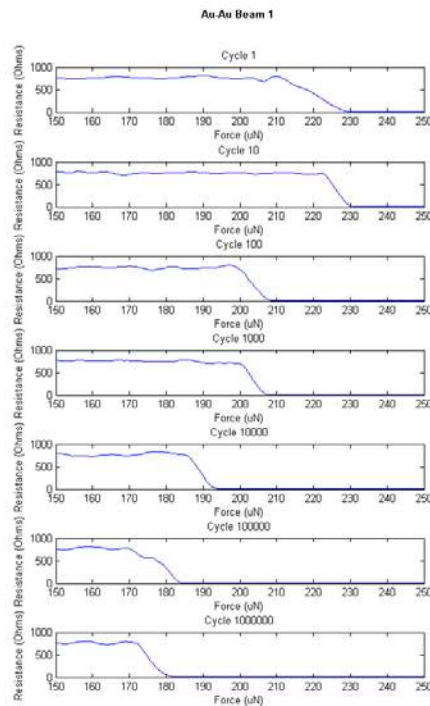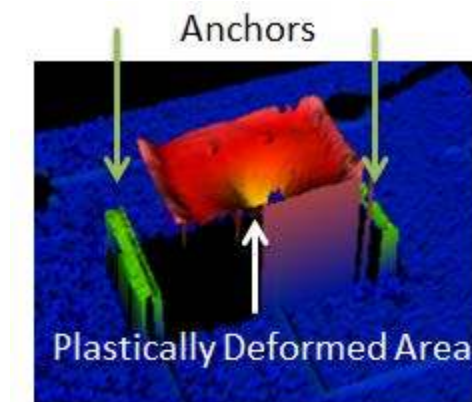

Figure 48 Fixed-Fixed Au Micro-Contact Support Structure

Figure 48 shows the CST data collected for the fixed-fixed Au micro-contact support structure. Looking at the figure, the force required for contact make decreases from 220µN to 175µN after 1 million actuations. As stated previously, the cause of reduced required

force for contact make is a change in the micro-contact support structure's geometry. Using the Zygo system, the tested micro-contact support structure was inspected for a visible change in geometry. As seen by Figure 49 and Figure 50, the force sensor left an impression in the all Au beam of the micro-contact support structure.

Figure 49 Zygo Intensity Map showing Contour of Micro-Contact Support Structure

Figure 50 Zygo 3D Image of Fixed-Fixed Au Micro-Contact Support Structure

The beam itself was approximately 2.7µm thick. For plastic deformation, the applied force must meet and surpass the yield stress of the material, which is the lowest value for stress to cause permanent deformation. According to Volinksky *et al.*, the yield stress for Au films decreases with a rise in material temperature, which can increase by the flow of current

102

through the micro-contact and supporting structure [120]. His team also reports that for a 2.7µm thick Au film, the yield stress can be as low as 360MPa (or 360µN/µm²) at room temperature and become 160MPa (or 160µN/µm²) at 120°C [120]. Considering that the max applied force to the beam was 350µN in order to achieve near 100µN of contact force, it is likely that the yield stress threshold was passed causing the beam to be plastically deformed.

4.2.2.3 Fixed-Fixed Ag-Au Micro-Contact Support Structure
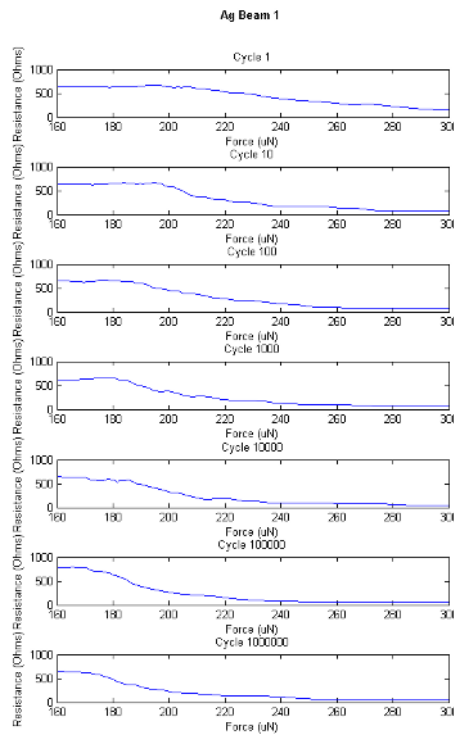
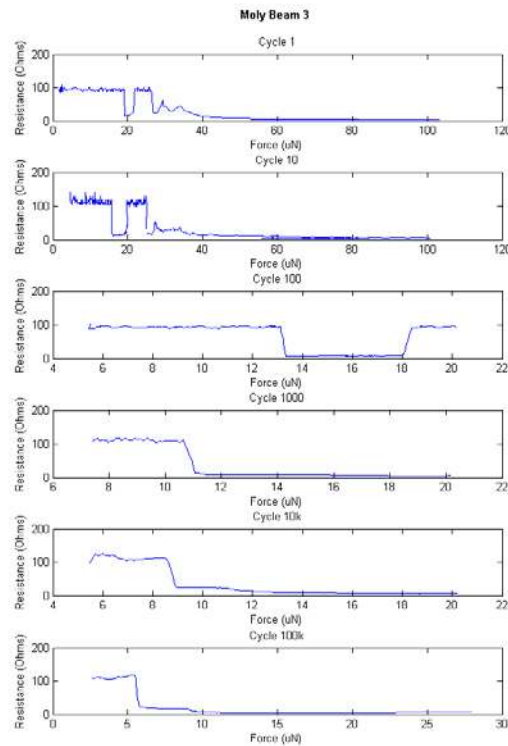**Figure 51 CST Data for Fixed-Fixed Ag-Au Micro-Contact Support Structure**

The fixed-fixed Ag-Au micro-contact support structure provided the data collected in Figure 51. The device was tested under the same conditions as the fixed-fixed Au micro-contact support structure, with measurements every 100,000 cycles until failure. As was discussed in the VCT section for this device, the high closed contact resistance value (~50Ω)

is due to the odd geometry of the structure near the anchor and the possibility of an underdeveloped micro-contact bump.

Figure 52 Fixed-Fixed Shorted Mo-Au Micro-Contact Support Structure

Recall from Figure 38 that the fixed-fixed Mo-Au micro-contact support structure had 'wrinkled' geometry. The uneven geometry of the micro-contact support structure could have provided multiple metal to metal contact points. Multiple contact points may be the reason for the unexpected results in cycles 1, 10, and 100. In cycle 1, the applied force of 20µN causes a 'wrinkle' to make metal to metal contact. As more force is applied, the geometry of the beam changes and contact is lost as evident by the increase in contact

resistance to the initial contact resistance value. As the applied force becomes greater, odd

geometry causes the relatively small peaks in contact resistance until metal to metal contact

is stabilized after 40μN. As the micro-contact support structure is actuated repeatedly, the

contact area of the micro-contact support structure begins to smooth and the odd geometries

no longer interfered with the resistance measurement. Figure 53 provides a visual

representation of what occurred between cycles 1, 10, and 100. By cycle 1000, the micro-

contact support structure is behaving similar to its fixed-fixed Au micro-contact support

structure counterpart.
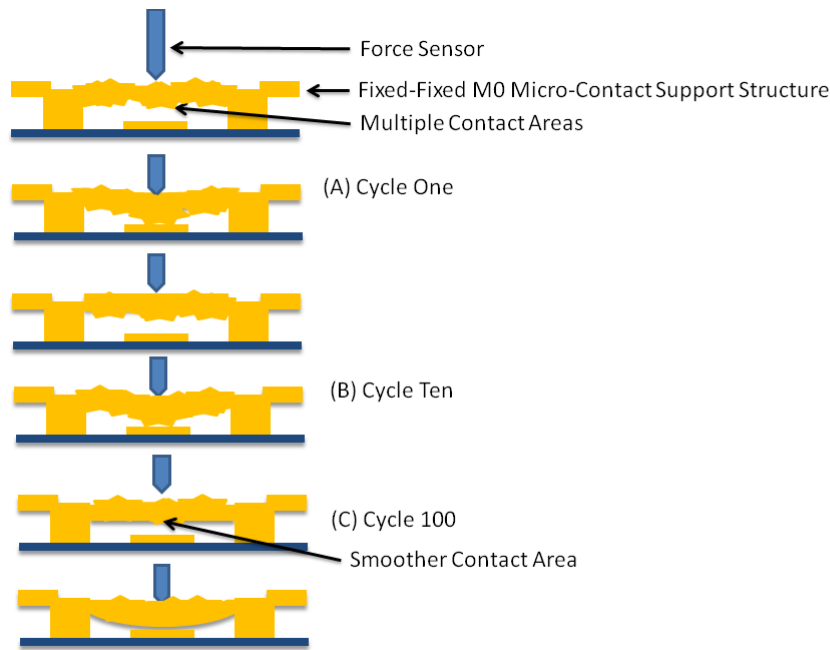
Figure 53 Fixed-Fixed Mo-Au Micro-Contact Support Structure Representation

4.3 Investigative Questions Answered

4.3.1 Micro-Contact Test Fixture for Studying Micro-Contact Resistance

Evolution

Each micro-contact support structure that was tested was subjected to the following tests as shown in Table 5. The tests were repeatable with minimal interruption caused by output errors from the current source. The devices were tested to examine the evolution of contact resistance over 10 million cycles. Measurements were made up to the designated number of cycles by the measurement interval. Between measurements, the micro-contact was cycled at the actuation rate and force. This system has proven to be an effective test fixture for cycling micro-contacts at relatively fast cycle rates to examine the evolution of micro-contact resistance.

Table 5 Automated Micro-Contact Tests Performed by Micro-Contact Test Fixture

Number of Cycles	Measurement Interval	Actuation Rate (Hz)	Actuation Force (µN)
100	10th	10	100
1000	100th	100	100
10000	1000th	1000	100
100000	10000th	3000	100

The current source output errors were sporadic (two occurrences out of 40 measurements on one support structure). The error required a reset of the current source to fix before the Lab View micro-contact test program could be restarted. The only detriment to a micro-contact test by the current source error is a loss of accuracy in the cycle count. The accuracy of the cycle count is changed because the test is interrupted and the recorded number of cycles up to the point of error is reset.

### 4.3.2 Performance Evolution of Micro-Contact Support Structures

The PolyMUMPs micro-contact support structure was effectively 'shorted' between 4-5Ω and showed no change in contact resistance with applied force for the virgin contact tests. Because of this, the PolyMUMPs micro-contact support structures were not cold switched. On the other hand, the fixed-fixed micro-contact structures were also shorted but demonstrated lower contact resistance as the applied contact force increased. The fixed-fixed micro-contact support structures were shorted with an average initial resistance value of 110Ω. Despite this defect, four structures were tested up to 100,000 cycles to examine changes in contact resistance over their lifetime: three shorted fixed-fixed Au micro-contact support structures, three functional fixed-fixed Au micro-contact support structures, two fixed-fixed Ag-Au micro-contact support structures and one Mo-Au fixed-fixed micro-contact support structure.

The following figures plot the 100,000 cycle lifetime of the tested shorted and functional micro-contact support structures which ranged in thickness from 2.6 µm to 3 µm. The following figures are plots of the initial (open) and closed resistance values at cycle intervals. The closed resistance values are all for 100µN of contact force. By plotting the data in this manner, it is possible to determine whether or not the micro-contact support structure failed in the open state (i.e. contaminant film development) or failed in the closed state (i.e. stiction). A discussion of the results follows each figure.
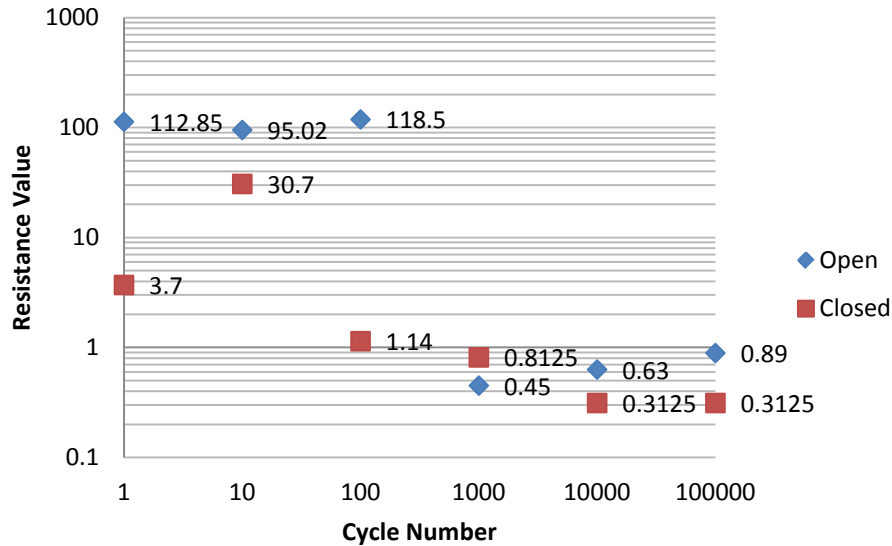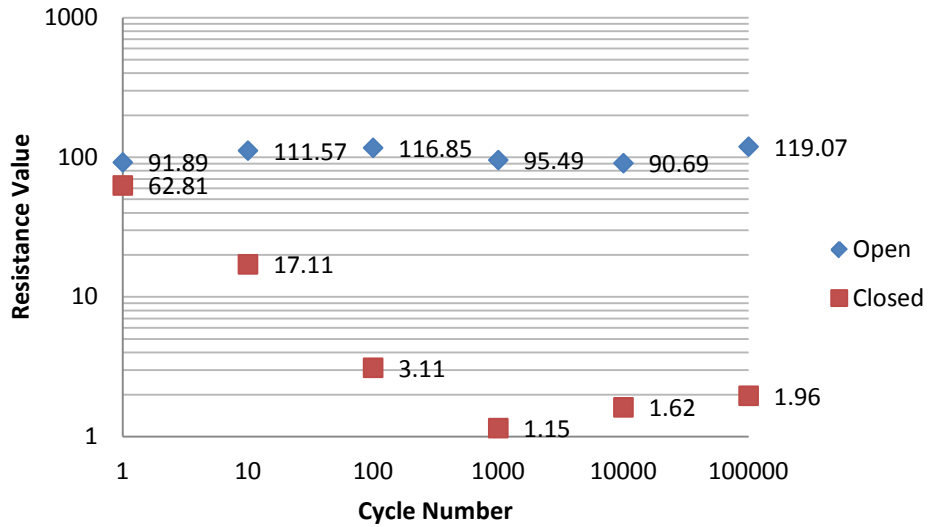
Figure 54 Open and Closed Resistance Values for Shorted Fixed-Fixed Au Micro-Contact Device One

Figure 54 shows the open and closed resistance values for fixed-fixed Au micro-contact device one. As can be seen in the figure, the micro-contact support structure begins its first 100 cycles fully returning to the open state. After 100 cycles, the open resistance is less than the closed resistance. This inversion can be explained by considering that the micro-contact support structure was stuck down in previous cycles until cycle 1000, where the application of force aided in separating the micro-contact. This is evident by noting that the open resistance for the remaining cycles is greater than the closed resistance. While looking at the cycles from 1000 to 100,000, the open contact resistance is no longer returning to the initial contact resistance of 110Ω; indicating that the micro-contact support structure has failed closed. Failure in the closed state could have occurred due to the contaminant film providing a greater chance for stiction by increasing the area available for contact.
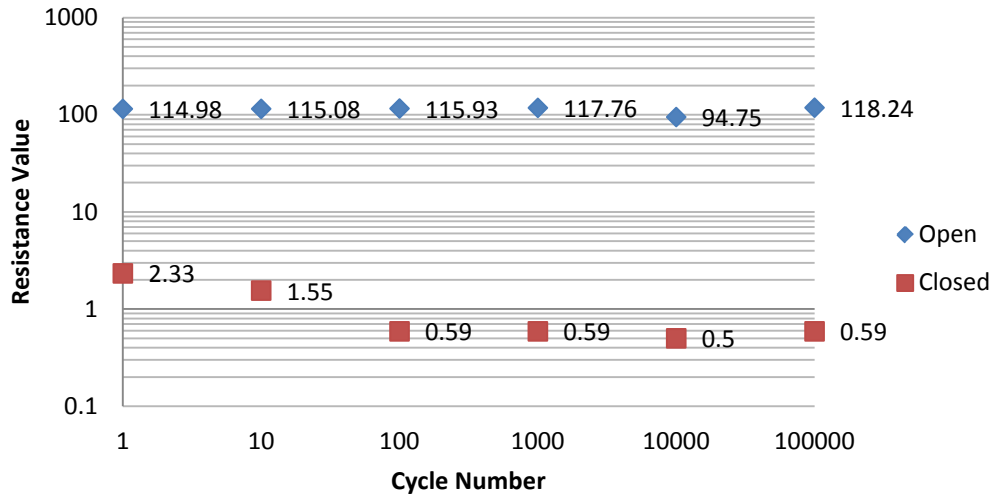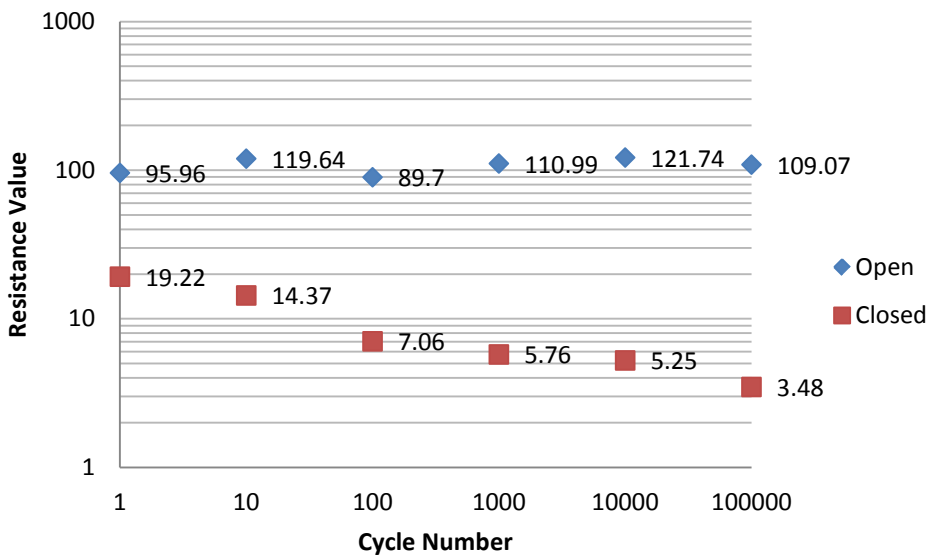
Figure 55 Open and Closed Resistance Values for Shorted Fixed-Fixed Au Micro-Contact Device Two

Figure 55 shows the open and closed resistance values for fixed-fixed Au micro-contact device two. As the limited lifecycle test progressed, the suspect contaminant film theory from earlier is supported by the closed resistance trending toward lower resistance values. Also aiding the conjecture is the open resistance trending toward greater resistance values (114Ω to 118Ω) which indicates that the contact between the support structure and contaminant film is being reduced, with more actuations to remove the contaminants from the contact area, the device may potentially have shown a complete open. Though quite a small change in open resistance given the number of actuations, the trend for greater open contact resistance suggests that the contaminant film is the cause for shorting. As the micro-contact support structure is repeatedly cycled, the film is fritted away from the contact area and reducing the available contaminant film for the short circuit. Figure 56 also supports the two claims: there is a contaminant film being fritted away and that the contaminant film is responsible for the short. The justification is the change in closed resistance from 62Ω to $<2\Omega$ as well as the upward trend in open contact resistance (91Ω to 119Ω).

109

Figure 56 Open and Closed Resistance Values for Shorted Fixed-Fixed Au Micro-Contact Three

Figure 57 Open and Closed Resistance Values for a Mo-Au Micro-Contact

Figure 57 shows the open and closed resistance values for the Mo-Au fixed-fixed micro-contact support structure. Despite the unusual geometry of the device, the limited lifetime test data in the figure shows similar trending behavior as its fixed-fixed Au

counterpart. The trend of the closed contact resistance moving from 19Ω to 3Ω occurs slower with this particular device than the previously tested structures. This may be evidence of a contaminant film such as residual photoresist, also responsible for its short circuit, which is more robust than the contaminant film found in the fixed-fixed Au micro-contact structure. The short circuit could located at the contact area or from the underside of the structure being in contact via the contaminant film to the contact area or the traces leading to the contact area. The difference in robustness of the contaminant film could be explained by the relative variances of the fabrication processes. The addition of Mo during the fabrication process to the micro-contact support structure increases the heat that the sacrificial layer is exposed to, which could imply that the sacrificial layer is being over baked and hardened to a point which makes it relatively difficult to remove. The open contact resistance varies widely (approximately 20Ω) and inconsistently. As discussed previously, the odd beam geometry can cause unexpected results and may be the cause of the 20Ω variance.

Figure 58 shows the reliability test results which show the change in resistance over the 4.1 million cycles the micro-contact experienced. An explanation for the jagged climb in resistance is provided by the deformation of the micro-contact support structure's bridge. Examining Figure 59, the open state resistance is that of the ~750Ω resistor placed in parallel with the micro-contact for current limiting protection. By cycle 1000, the contact resistance has dramatically dropped from its first cycle measurement of 2.86Ω. This may indicate the point at which either the Au beam or the contact interface of the micro-contact support structure has plastically deformed similar to the beam discussed previously in Figure 50.
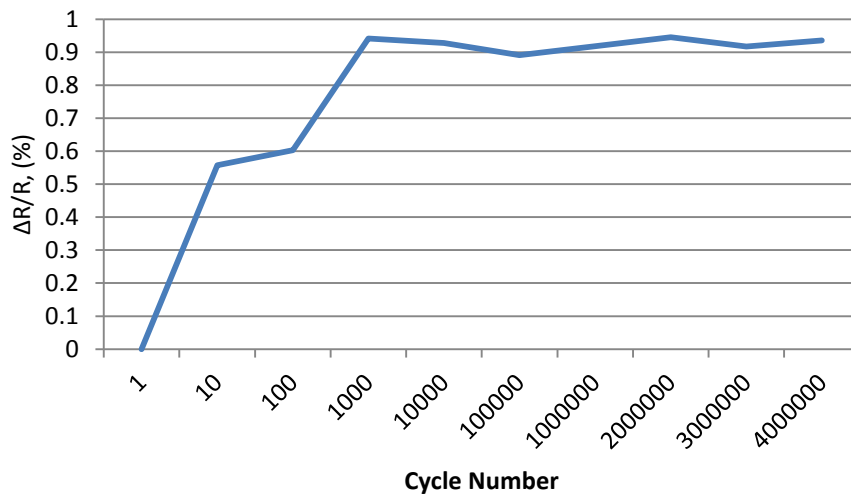
Figure 58 Reliability and test results showing the resistance change over Au beam 1 lifetime
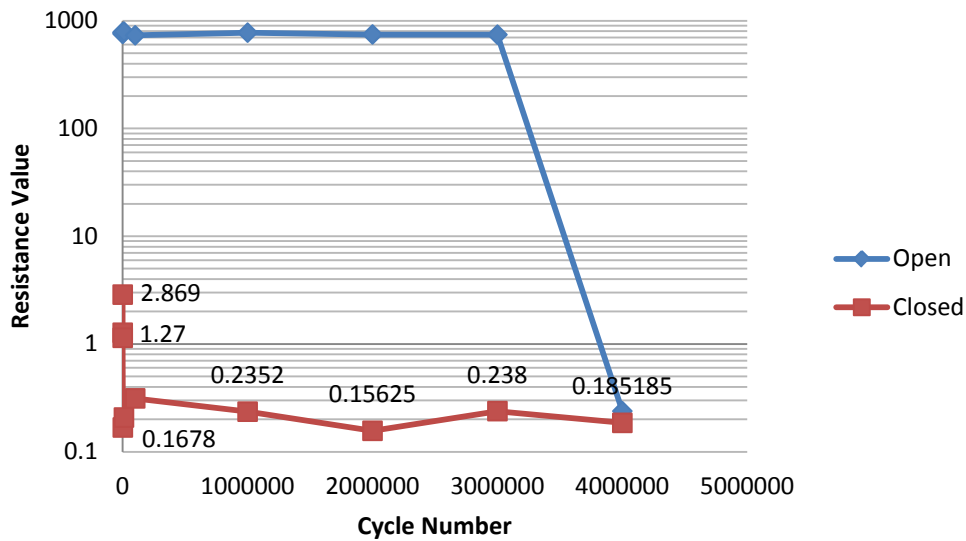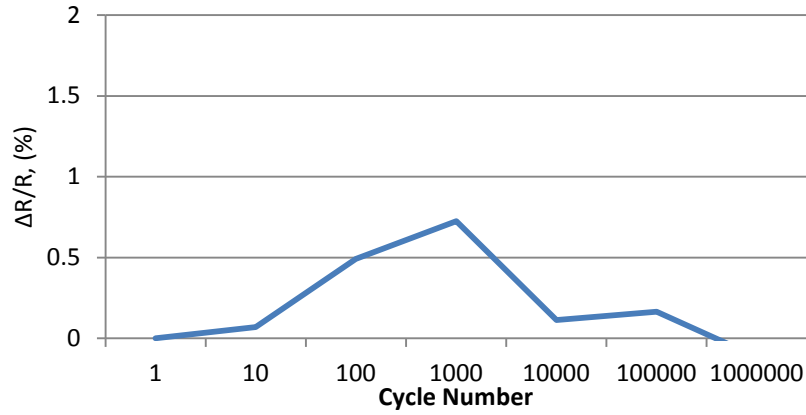

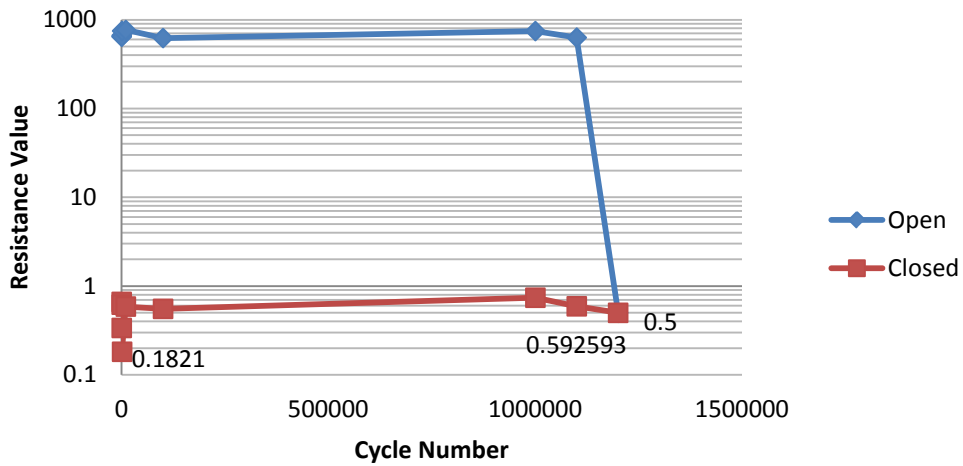**Figure 59 Open and Closed Resistance Values for Functional Fixed-Fixed Au Micro-Contact Support Structure One**

After 4.1 million actuations, the micro-support structure failed closed and provided a closed contact resistance of 0.5Ω. Using equation (37), this particular contact reached the - 0.5 dB attenuation RF criteria for failure at 2.7 million cycles. Undergoing the same tests, the

112

functioning fixed-fixed Au micro-contact support structures two and three data are shown in Figure 60, Figure 61 and Figure 62.

Figure 60 Reliability and test results showing the resistance change over Au beam 2 lifetime

Figure 61 Open and Closed Resistance Values for Functional Fixed-Fixed Au Micro-Contact Support Structure Two

Figure 60 shows the reliability and test results for the Au beam 2 over the 1.2 million cycles leading to its failure. Using equation (37), this particular contact reached the -0.5 dB attenuation RF criteria for failure at 0.7 million cycles. Figure 61 shows that the functioning fixed-fixed Au micro-contact support structure maintained lower values of contact resistance

than the initial 0.66Ω from cycle one.   As will be discussed later, the micro-support structure failed closed after 1.2 million actuations with a contact resistance of 0.5Ω.

Figure 62 shows that the fixed-fixed Au micro-contact support structure experienced steadily increasing contact resistance with the more actuations; which is also represented in Figure 63. This particular micro-contact was cycled nearly 10.2 million times, at which point the closed contact resistance was 14.43Ω. Using equation (37), this particular contact reached the -0.5 dB attenuation RF criteria for failure at 5.6 million cycles. Zygo imaging revealed that the micro-contact support structure had plastically deformed. Along with plastic deformation affecting the contact area, the rise in resistance after 7 million cycles indicates the development of a frictional polymer and is likely the reason for the increasing contact resistance.
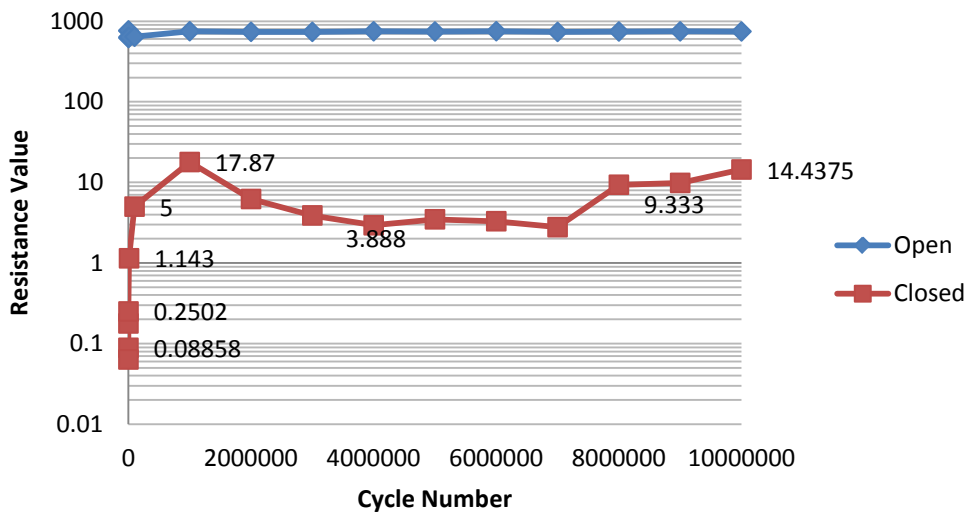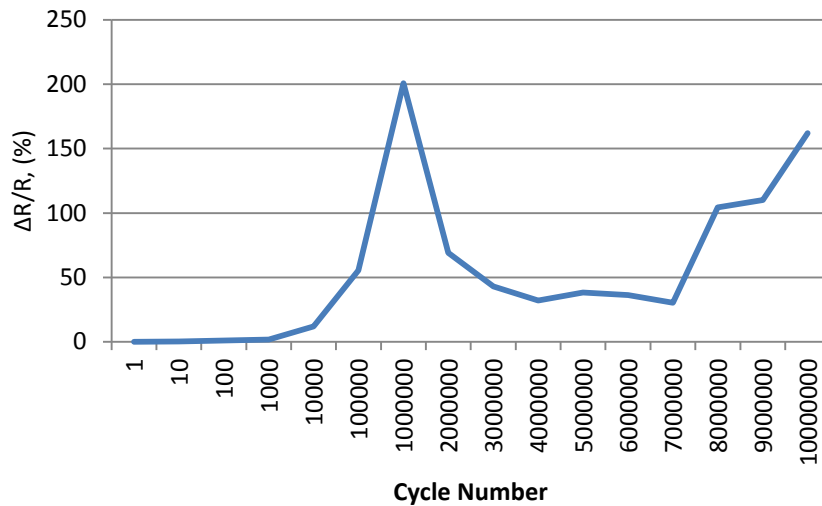

Figure 62 Open and Closed Resistance Values for Functional Fixed-Fixed Au Micro-Contact Support Structure Three

Figure 63 Reliability and test results showing the resistance change over Au beam 3 lifetime

After cold-switching the functional fixed-fixed Au micro-contact support structures for several million cycles a piece, the structures were 'peeled' back in order to reveal the lower contact area. The exposed lower contact areas were examined under the SEM for visual confirmation of changes to the contact area. Figure 64 and Figure 65 show the micro-contact areas after 4 million cycles and 1.2 million cycles respectively. Examining Figure 64, the micro-contact area shows evidence of material transfer and smooth bumps. The micro-contact area is not symmetrical due to changes in the micro-contact support structure over repeated actuations; deformation of the fixed-fixed beam changed the position of contact make. The asperities of the micro-contact likely experienced localized high temperatures from the current flow during the measurement. The raise in temperature at the localized spots caused the Au material to soften and in conjunction with mechanical pressure from the upper contact, smoothed the 'bumps' of the contact region.

115
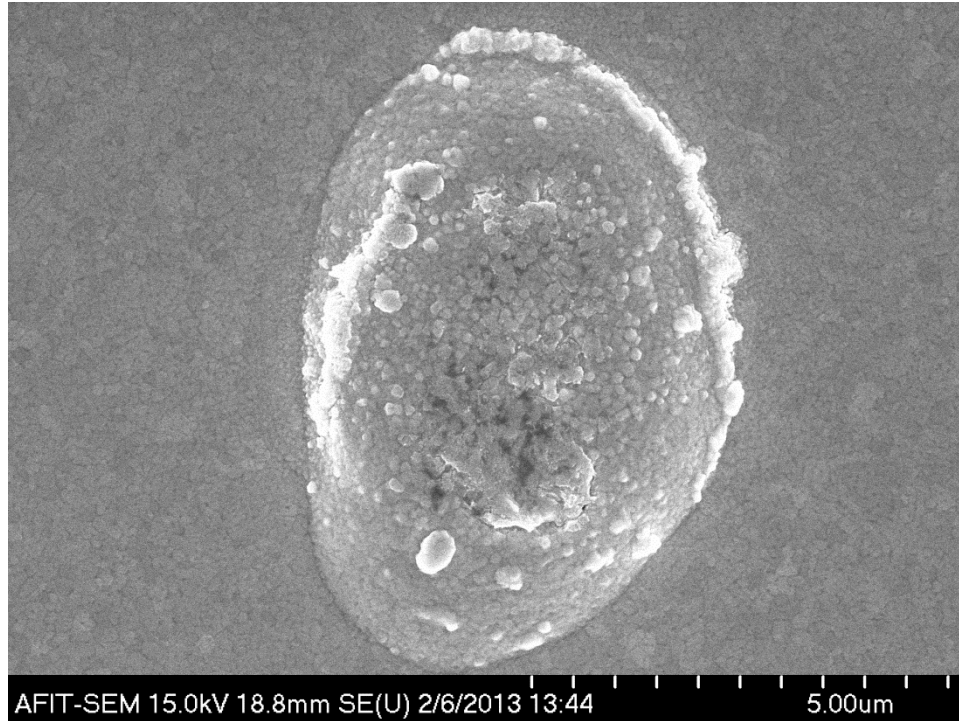
Figure 64 Exposed Micro-Contact Area for Fixed-Fixed Au Micro-Support Structure

Similar to Figure 64, the micro-contact shown in Figure 65 also shows signs of material transfer and material softening. As mentioned previously, the micro-contact for Figure 65 was only cycled 1.2 million times. Along with difference in micro-contact size (4µm and 2µm respectively), the 2.8 million cycles difference between the two contacts is the reason for the stark contrast in size and amount of material transferred. In Figure 65, it is clearer to see that the micro-contact experienced material transfer, softening, and flattening from the mechanical pressure of the upper contact.
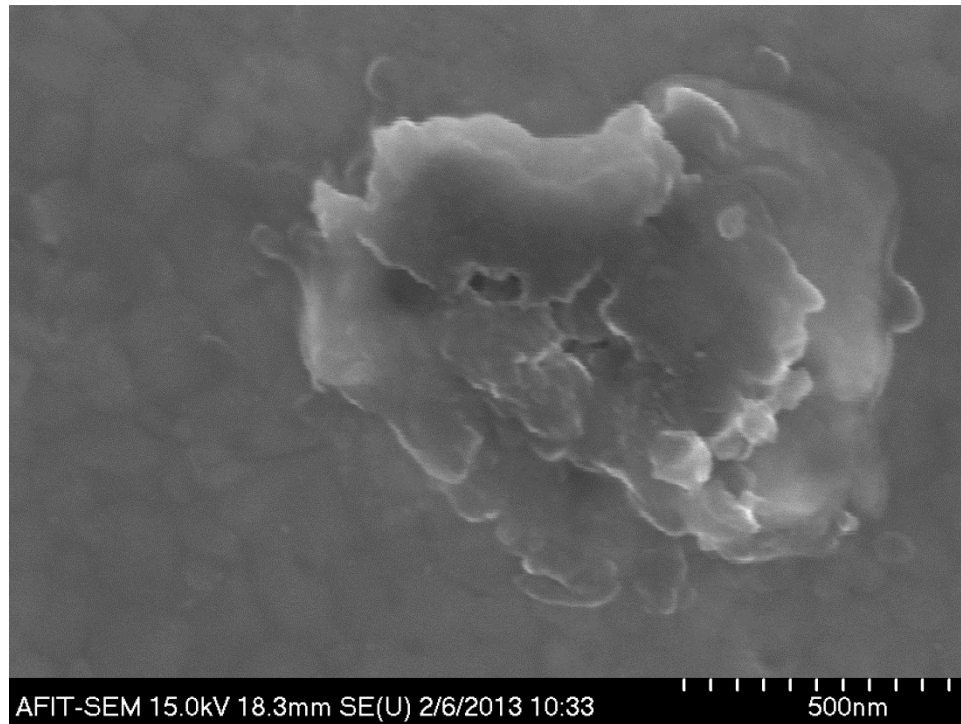
Figure 65 Exposed Micro-Contact Area for Fixed-Fixed Au Micro-Support Structure

Similar to the functional fixed-fixed Au micro-contact support structure three, the fixed-fixed Ag-Au micro-contact support structure was also cycled 10.2 million times. The device still provided an open at 10.2 million cycles but upon contact make, had contact resistance of 35.7Ω. As demonstrated by Figure 66 and Figure 67, the contact resistance of 158Ω from the initial cycle steadily decreased until the test was stopped at 10.2 million cycles and the contact resistance increased to 165Ω. This indicates a changing of the contact interface topology through repeated mechanical actuation for more contact area. Using equation (37), this particular contact reached the -0.5 dB attenuation RF criteria for failure at 3.9 million cycles.
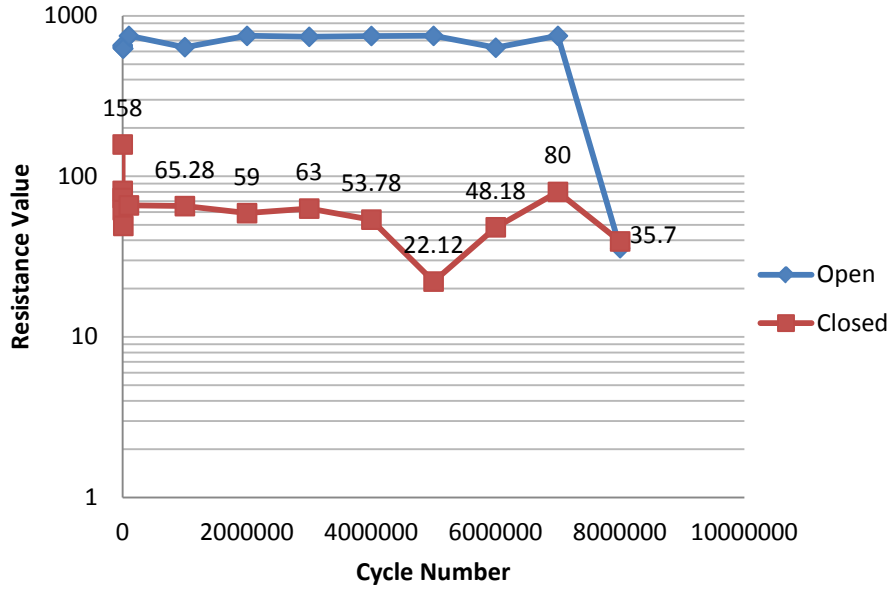
Figure 66 Open and Closed Resistance Values for Fixed-Fixed Ag-Au Micro-Contact Support Structure
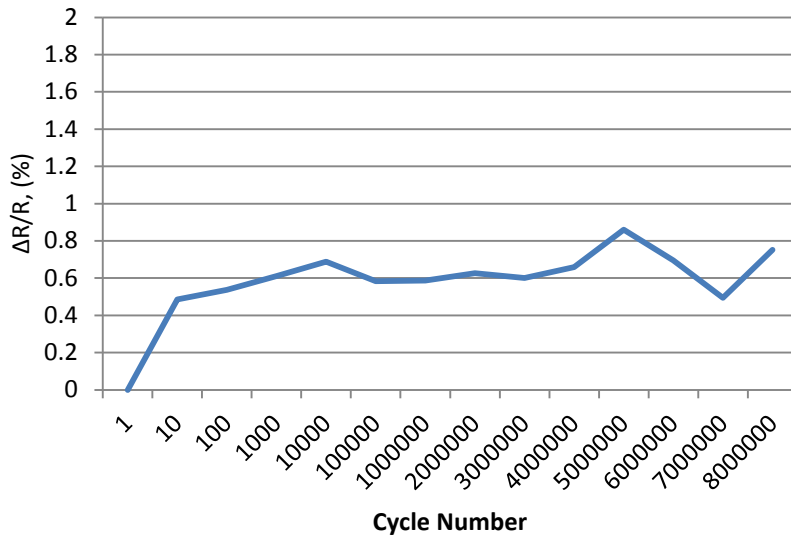
Figure 67 Reliability and test results showing the resistance change for Fixed-Fixed Ag-Au Micro-Contact Support Structure

The Ag-Au micro-contact support structure data shown in Figure 68 and Figure 69 shows that the micro-contact resistance varied from 0.37 Ω to 1.47Ω, improved from cycles 1000 to 10000, then began to sharply rise after 10000. The sharp rise in contact resistance can again be explained by the physical deformation of the contact support structure and micro-contact surface topology, which in turns can have a limiting effect on the area available for contact. Using equation (37), this particular contact reached the -0.5 dB attenuation RF criteria for failure at 1000 cycles.
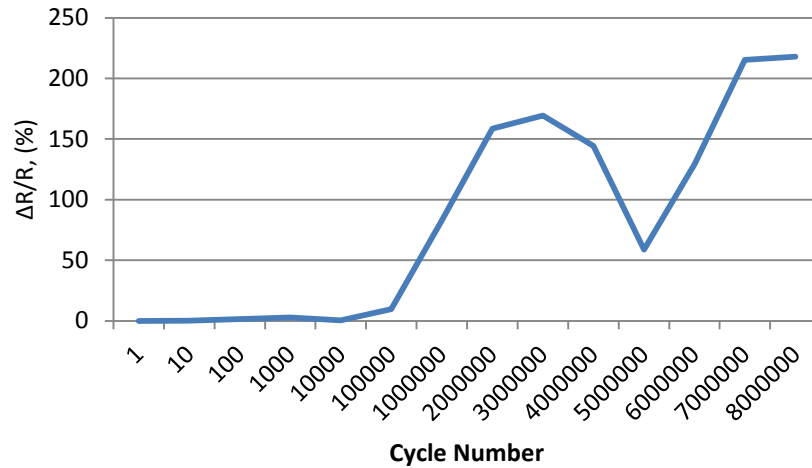

Figure 68 Reliability and test results showing the change in resistance for Fixed-Fixed Ag-Au Micro-Contact Support Structure Two
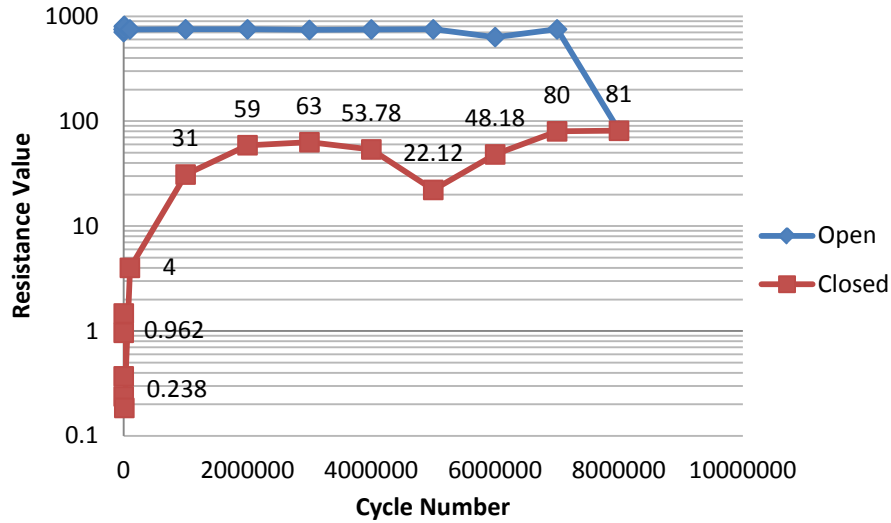
Figure 69 Open and Closed Resistance Values for Fixed-Fixed Ag-Au Micro-Contact Support Structure Two

4.3.3 Micro-Contact Support Structure Comparison

Of the micro-contact support structures tested, fixed-fixed Au, fixed-fixed Mo-Au, and PolyMUMPs, the fixed-fixed Au micro-contact support structure is the most suitable candidate for studying the lifetime performance evolution of micro-contacts. The main criteria for this determination are testability and design. Each support structure was unique in order to explore the advantages of their design. However, the ability to perform various tests with the micro-contact support structure is paramount for witnessing the evolution of micro-contact performance.

The current design of the PolyMUMPs micro-contact support structure as a testable device relies too heavily on the design's tolerance to residual stresses inherent in the foundry's processes. Another disadvantage to this design is the delay in fabrication time. The design is sent to a commercial company and requires month(s) before the device is fabricated and delivered. In addition, post processing must be performed if a micro-contact

material other than Au is to be examined. The design's advantage is the ability to examine the micro-contact interface simply by 'flipping' the polysilicon beam via its hinge. Then both the upper and lower contacts are ready for a number of examination methods (SEM, AFM, etc).

The fixed-fixed micro-contact support structure design is suitable for recreating Holm's crossed bar experiment on the micro level. Its design provides the advantage of a four wire measurement as well as stiffness in the micro-contact support structure's beam to prevent stiction. The Mo enhanced fixed-fixed micro-contact support structure's intended purpose was to provide greater restoring force and prevent or delay stiction from occurring. Unfortunately, the fabrication of a testable Mo-enhanced fixed-fixed micro-contact support structure has not been repeatable.

For the fixed-fixed Au micro-contact support structure, the preliminary devices were shorted due to issues with the fabrication process. While the suggestion could be made to study the evolution of micro-contact resistance on shorted micro-contact support structures, the argument against that notion is the element of the unknown physical contributions of the short circuit upon micro-contact resistance. The knowledge that current flow is precisely and only through the micro-contact is critical for obtaining data comparable to those found in literature as well as for making conjectures about the performance behavior.

To troubleshoot the fabrication process, three fabrication adjustments were examined using three wafers. First, to determine if the contact bump exposure was the issue, a wafer using the preexisting fabrication process was processed as a control and a wafer which skipped the contact bump exposure was processed. It was revealed that despite the lack of contact bump exposure, the devices still had unreleased photoresist beneath the micro-

121

contact structures. To guarantee full release of the micro-contact support structures, a third layer of SF-11 was added to create a larger gap and more exposed area for photo resist removal. With the fabrication process remedied, functional fixed-fixed Au micro-contact support structures were made and tested. The new fabrication process is repeatable and can be modified to include other material types; such as adding a layer of CNTs in the beam of the micro-contact support structure.

4.4 Summary

This chapter detailed the testing of the fixed-fixed micro-contact support structures and PolyMUMPs micro-contact support structures as well as described the success of using the micro-contact test fixture. The reasons for why the fixed-fixed Au micro-contact support structure is the best candidate for studying the evolution of micro-contact resistance were discussed and it was determined that the structure excelled in the areas of design and testability. Four shorted devices and five functional devices were examined under limited lifetime tests to confirm the validity of the micro-contact structure's design as well as the repeatability of the novel micro-contact test fixture's capabilities. One shorted device showed evidence of failing in the closed state while the other three provided signs of a contaminant film being fritted away and being responsible for the shorting of the micro-contact support structures. Also presented was the cold-switch and virgin contact test data for the three different micro-contact support structures. The PolyMUMPs micro-contact support structure was found to be defective by its design's sensitivity to residual stresses in the fabrication process. The VCTs and cold switch tests confirmed the existence of a

contaminant film and provided further justification that the film was being fritted away with repeated actuation.

V. Conclusions and Recommendations

5.1 Chapter Overview

The improvement of micro-contacts will provide benefits in many areas of technology. These benefits may include greater bandwidths, lower power consumption, and enhanced performance. To make these improvements, MEMS engineers need the capability to study the performance evolution of micro-contacts by examining the physical and chemical phenomena at the interface under controlled conditions. Previously at AFIT, a novel test fixture concept was drafted but never fully realized. This research focused on full realization of a test fixture which would allow future MEMS engineers to study the performance evolution of micro-contacts. The groundwork for exploring micro-contact physics was also put into place. This chapter summarizes the research effort with the lessons learned from the detailed results from chapter four as well as other work outside of this research. First, the main contributions of this research are discussed. Following this discussion, the recommendations for future research are provided.

5.2 Contributions

- This research led to the implementation of a novel micro-contact test fixture. The system provides AFIT the capability to study the lifetime evolution of micro-contact performance using high cycle rates (up to 3kHz) with known applied force where previously cycle rates with known force were reported at 0.5Hz.

- Novel micro-contact support structures which replicated Holm's well known crossed-rod experiment were fabricated and tested.

- Preliminary characterizations of the micro-contact support structures, to include the Mo enhanced fixed-fixed, Au fixed-fixed, and PolyMUMPs were accomplished. Based on comparisons, emphasis was given to the fixed-fixed micro-contact support structure design as the lead candidate for micro-contact study.

- A thorough background of the failure modes and relevant micro-contact theory was provided which serves as a starting point for future investigations into micro-contact physics.

- A solid foundation for future work on this effort is provided. This foundation gives clear insight into the design, fabrication, and characterization methodologies so a clear direction of how this research may continue is apparent.

5.3 Recommendations for Future Research

5.3.1 Testing Micro-Contact Material Types

Au-Au and CNT-Au composite, micro-contacts with structures which will only elastically deform during testing will be tested for micro-contact performance characteristics. As the most common type of contact in literature, Au-Au will be used for comparison to literature and as a baseline for comparison to the other micro-contact candidates. In order to test these contact material types, Holm's crossed rod contact experiment is adapted as a suitable method to measure micro-contact resistance.

Similar to the crossed rod experiment, the contact voltage is measured between the upper micro-contact area and the lower micro-contact area; this is effectively the micro-contact voltage. The micro-contact voltage will be divided by the current flowing through the micro-contact to obtain the micro-contact resistance. The measurement, as mentioned previously, will be performed under dry circuit conditions to reduce heating of the contact.

The contact force applied will be limited to low values to enable elastic deformation to produce the closed interface of the micro-contact. The contact design will be a circle with an approximate radius defined by the design of the micro-contact structure. Comparing the resistance of analytical contact resistance for the contact material type and contact force to the measured value will provide evidence as explained by Holm of, "a film penetrable for tunneling electrons" [8].

5.3.2 Upgrading the Test Fixture

The micro-contact test fixture uses a current source which operates at its lower limits. Being at the lower spectrum of its range for supplied current, the current through the micro-contact is inconsistent and varies greatly compared to the precision required. For example, to test under dry circuit conditions, the supplied current should not exceed 3mA. When applying 3mA of current (the lower limit of the current supply), the current will vary from 2.5-3.1mA. In order to improve on the precision and accuracy of the system, the current source module should be replaced by a higher quality current source.

### 5.3.3 Improving Fabrication Method

In order to reliably test micro-contacts, micro-contact support structures which are not susceptible to plastic deformation at the applied loads needed should be fabricated. The design and fabrication should be reviewed and iterated until success. The next area in this

research is to investigate the performance evolution of different micro-contact material types and to find an accurate description for the physical phenomena at the interface of the micro-contact. Information gathered from the review of current micro-contact literature should be compared with what was witnessed from cold-switch and hot-switch tests. The results of the micro-contact tests must be used to test relevant analytical equations or to develop more accurate analytical equations. The conformity of the resultant data to the equations provides confidence in the underlying physics theory to produce the analytical equation.

Appendix A: Lab View

VIRGIN CONTACT TEST INFORMATION

The following figure shows the virgin contact test program block diagram.
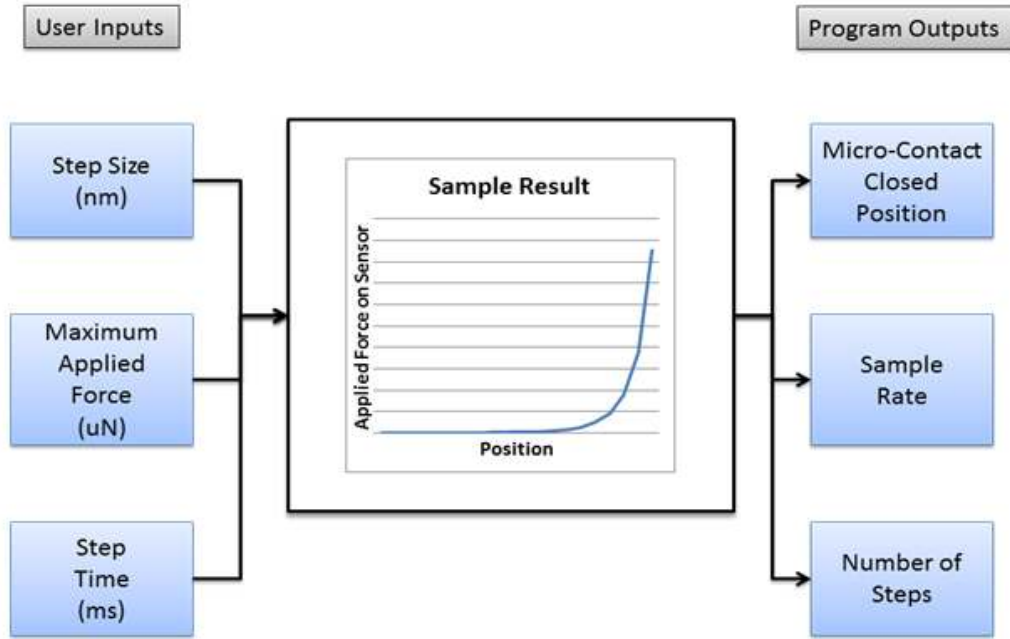

Figure 70 Virgin Contact Test Program Block Diagram

Specification of the step size allows for variances in micro-contact fabrication and design. As the gap between the micro-contacts may be designed at varying distances, the ability to set a step size explicitly prevents an application of force to the micro-structure which could cause plastic deformation. Setting the maximum applied force provides protection from exceeding the limits of the force sensor as well as the micro-structure. In order to have a more controlled approach by the force sensor to the micro-contact, the user may set a time interval at each step. At each step, a reading for the applied force, contact voltage, and contact current takes place. The values of the readings are then stored in an excel file upon completion of the test.

The output of the virgin contact test program is the applied force and position of the sensor required for a closed connection of the micro-contact. The sample rate is provided in order to verify the chosen time at each step and number of steps taken. The determination of a closed connection is performed by examining the recorded data for a real result in micro-contact resistance. The applied force and position required for a real result in micro-contact resistance are then offsets so that the true applied contact force is calculated. The position and applied force values are inputs for the next chosen type of testing: hot-switch or cold-switch.

HOT-SWITCH TEST INFORMATION

The following figure shows the hot-switch program block diagram.
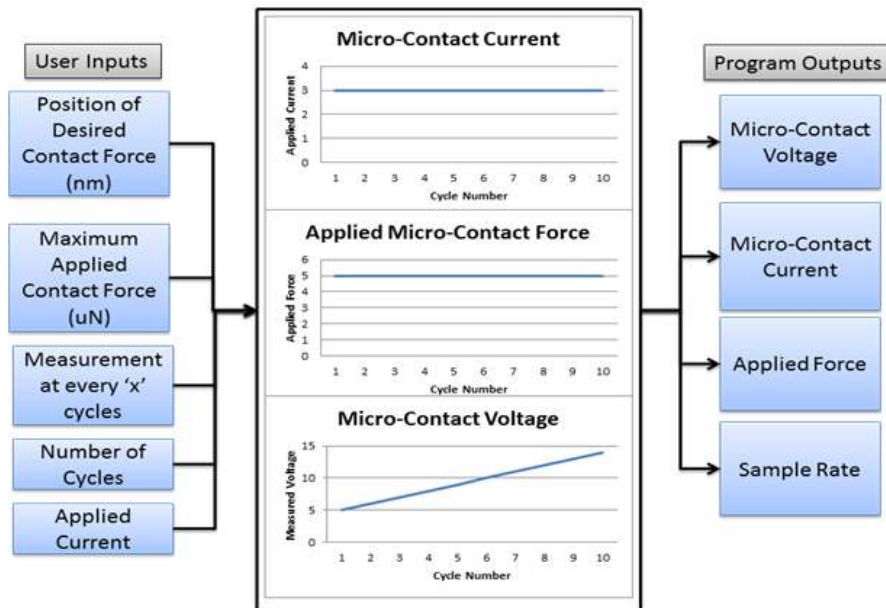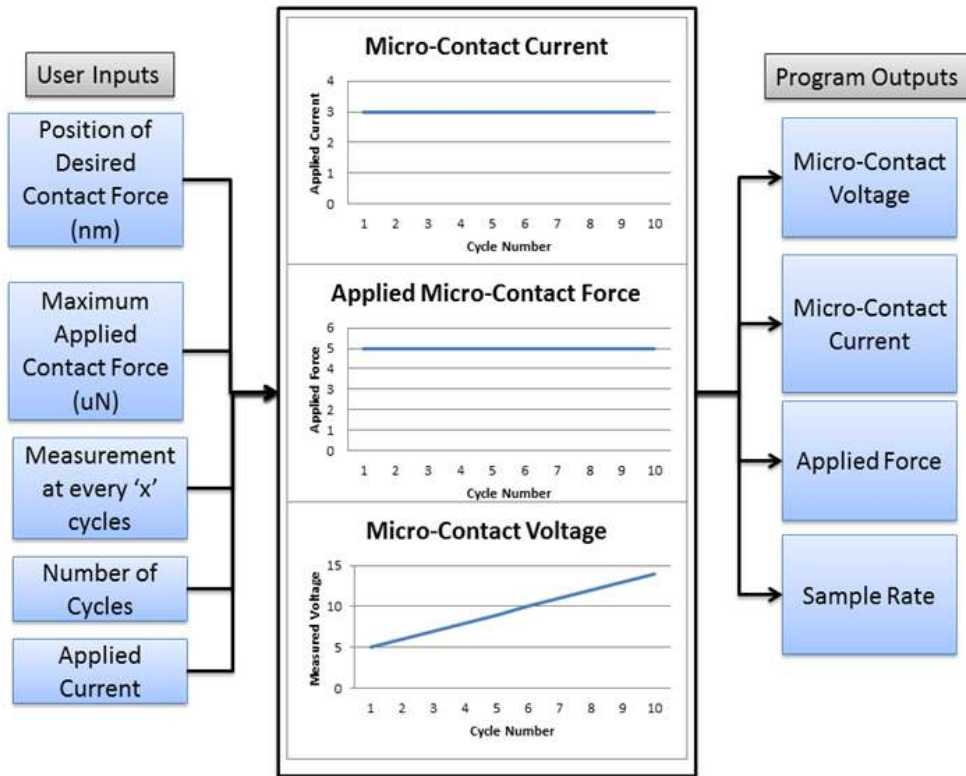
Figure 71 Hot-Switch Program Block Diagram

Most important for the hot-switch testing is knowing the position the force sensor needs to be in order to apply the appropriate and desired contact force. Setting the maximum applied contact force establishes a force limit to protect the force sensor and the micro-contact structure. This limit is checked every measurement to ensure compliance. If the force applied is greater than the limit, which can be caused by position drift, then the program reduces the position accordingly to apply the desired contact force. Position drift occurs through the repeated commands sent to the piezo control unit. Due to systematic errors in converting from digital to analog control signals, i.e. lab view to piezo controller to piezo motor, the position requested by the user is given to the controller but slight variances in the piezo motor actuation capability cause a drift in position. To raise the sample rate, the user may input the number of cycles between measurements. The time in which it takes one iteration of an actuation and measurement decreases without having to take a measurement. If desired, this feature allows the user to see only those data points after so many actuations. Specification of the number of cycles to perform and current to apply to the micro-contact allows for a characterization of the micro-contact for the given performance requirements.

The output of the hot-switch program is an excel file which contains the applied current and force, measured voltage, and calculated micro-contact resistance. The sample rate is also provided for the interest of rate of actuation. The information provided from this test can then be used to characterize the performance of the micro-contact. The applied current and measured voltage across the micro-contact is used to calculate the micro-contact resistance.

Plotting the micro-contact resistance against number of cycles will show the relative lifetime of the given micro-contact structure.

COLD-SWITCH TEST

The following figure shows the block diagram for the cold-switch program.

Figure 72 Cold-Switch Program Block Diagram

As with the hot-switch test program, the most important input is knowing the position the force sensor needs to be in order to apply the appropriate and desired contact force. Setting the maximum applied contact force establishes a force limit to protect the force sensor and the micro-contact structure. This limit is checked every measurement to ensure compliance. If the force applied is greater than the limit, which can be caused by position

drift, then the program reduces the position accordingly to apply the desired contact force. Position drift occurs through the repeated commands sent to the piezo control unit. Due to systematic errors in converting from digital to analog control signals, i.e. lab view to piezo controller to piezo motor, the position requested by the user is given to the controller but slight variances in the piezo motor actuation capability cause a drift in position. To raise the sample rate, the user may input the number of cycles between measurements. The time in which it takes one iteration of an actuation and measurement decreases without having to take a measurement. If desired, this feature allows the user to see only those data points after so many actuations. Specification of the number of cycles to perform and current to apply to the micro-contact allows for a characterization of the micro-contact for the given performance requirements.

The output of the cold-switch program is an excel file which contains the applied current and force, measured voltage, and calculated micro-contact resistance. The sample rate is also provided for the interest of rate of actuation. The information provided from this test can then be used to characterize the performance of the micro-contact. The applied current and measured voltage across the micro-contact is used to calculate the micro-contact resistance. Plotting the micro-contact resistance against number of cycles will show the relative lifetime of the given micro-contact structure.

LAB VIEW PROGRAMMING INFORMATION

Lab View is a dataflow visual programming environment and general programming language. The interface allows users to 'code' based on the visualization of how data flows through the system they wish to implement. The following are screenshots of the graphical

131

programming interface which comprise the automated data acquisition system. Following

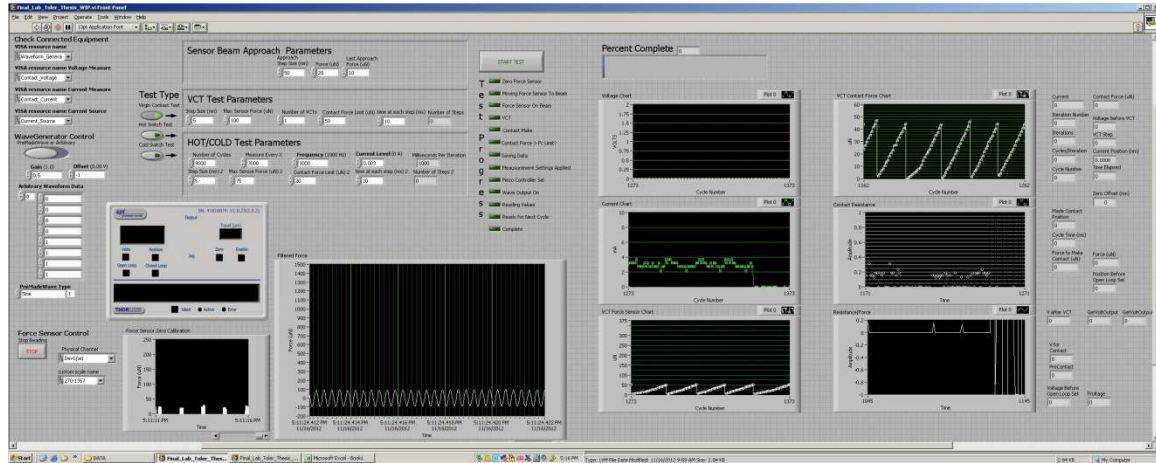the screenshots is a general description of what each 'frame' of programming accomplishes.

Figure 73 Lab View Data Acquisition System User Interface

Figure 73 shows the user interface for the automated data acquisition system. On this

screen, the user may determine the test type to be performed, set the parameters, start and

stop the test, and monitor the test's progress.
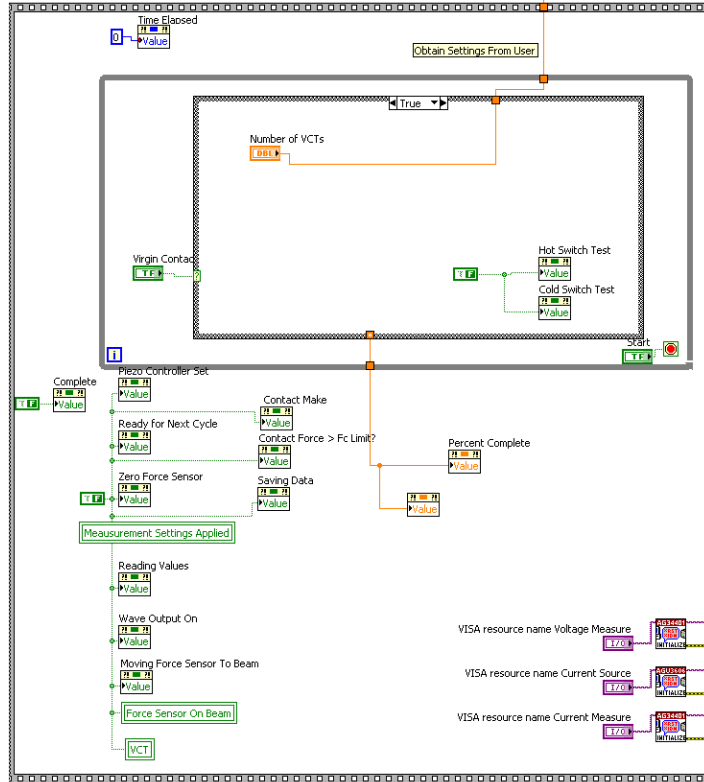
Figure 74 Frame 1 of the Graphical Programming for the Automated Data Acquisition System

Frame 1 is responsible for accepting the user's input for the desired test type and resetting the progress indicators on the main user interface screen. While loops within the frame allow the user to adjust parameters and settings before beginning the test.
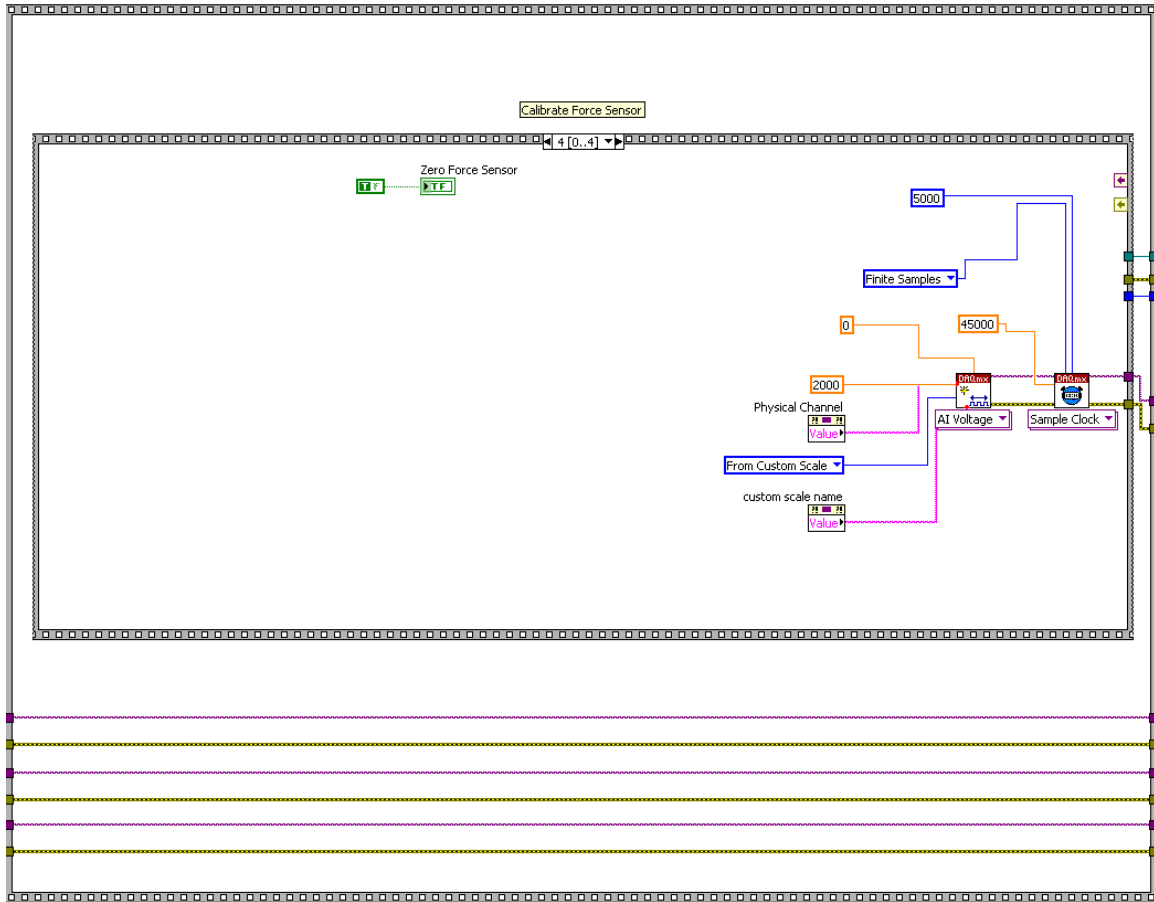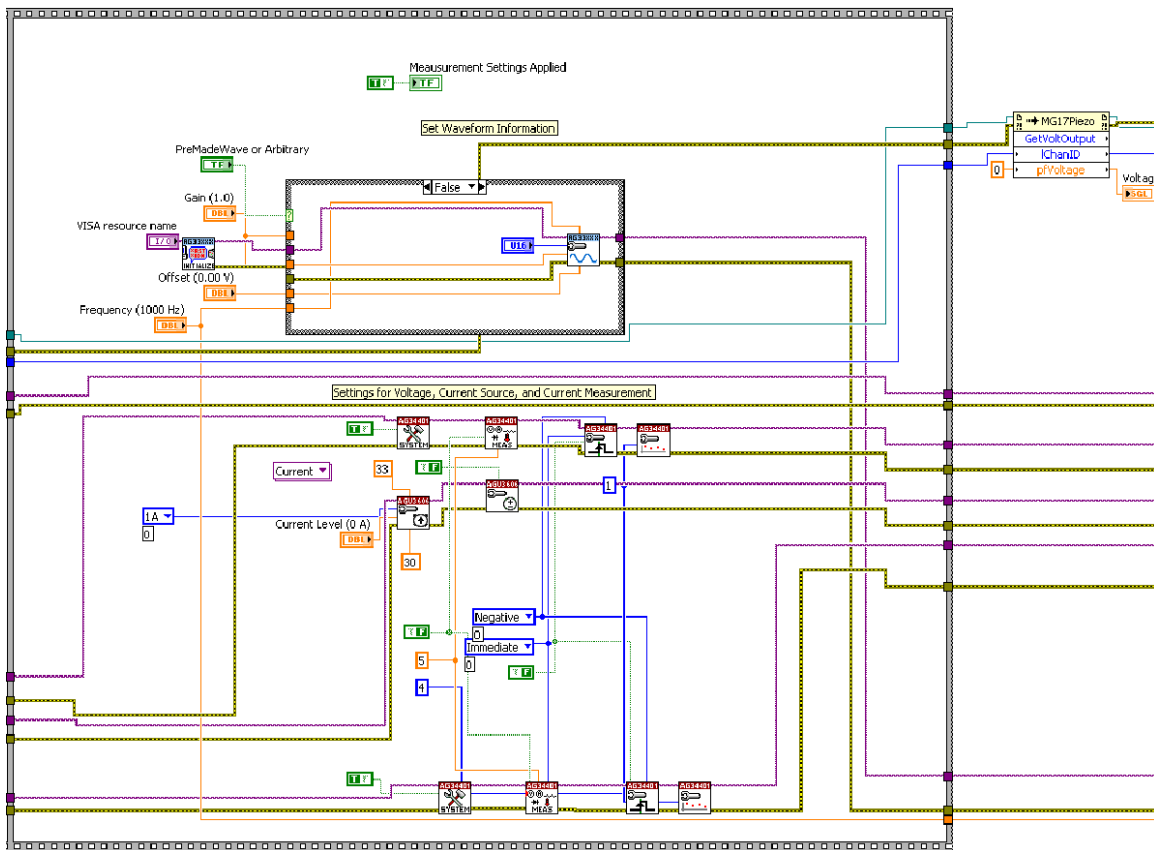
Figure 75 Frame 2 of the Graphical Programming for the Automated Data Acquisition System

Frame 2 is responsible for the calibration of the force sensor. In this frame, the piezo controller and the force sensor's sampling clock are initialized. The force sensor is then zeroed and the graph displaying the force sensor's output on the user interface screen is adjusted. The sampling condition of the force sensor is changed from continuous to finite sampling for the purpose of performing incremental measurements in the next frame.
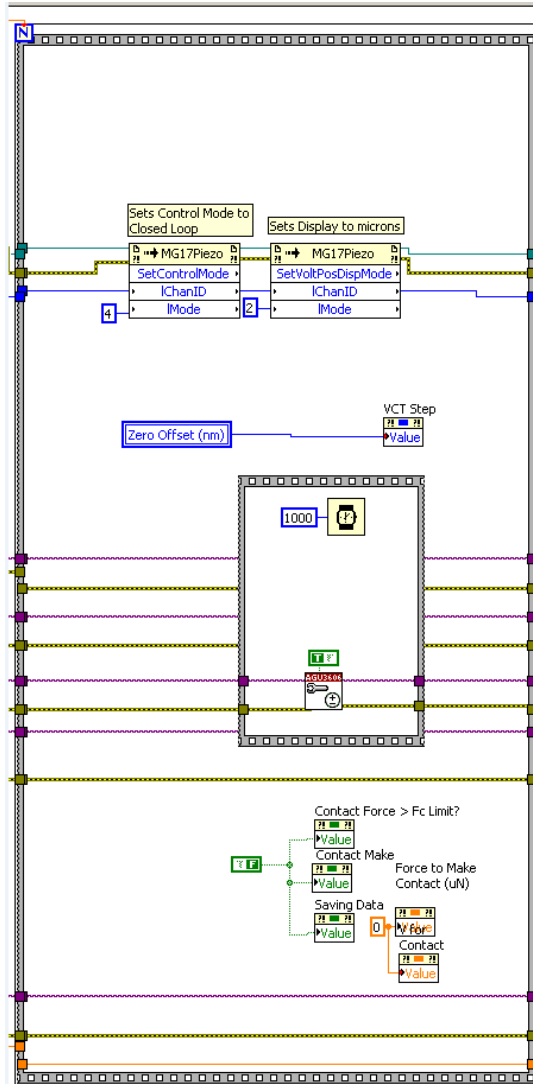
134
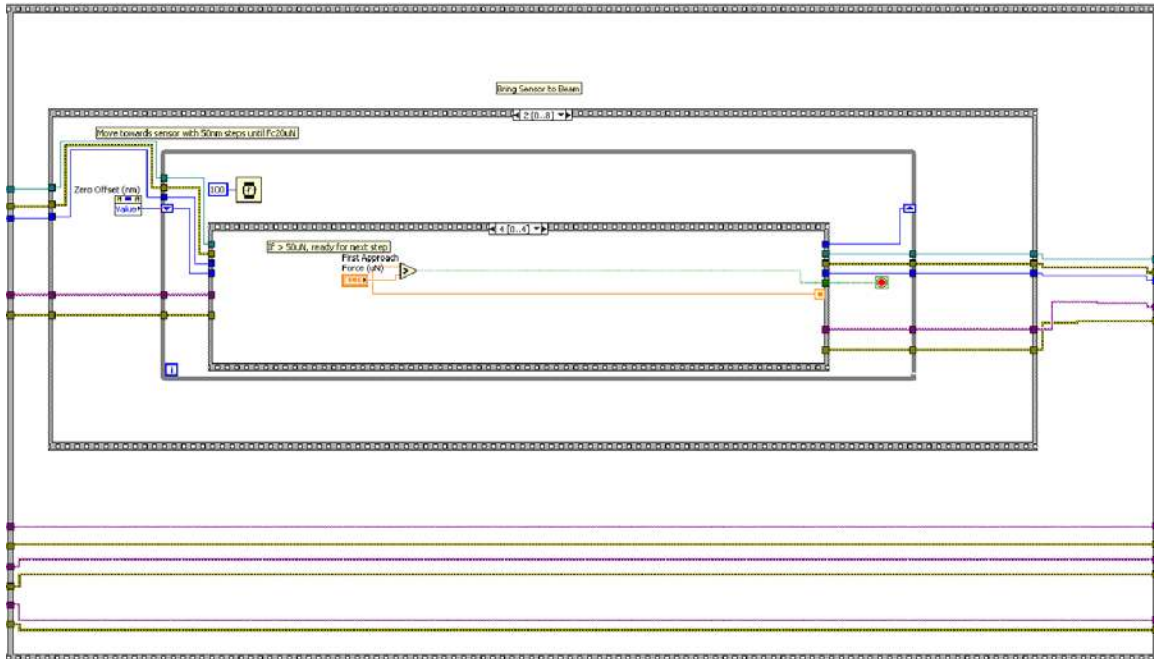
Figure 76 Frame 3 of the Graphical Programming for the Automated Data Acquisition System

In Frame 3, the force sensor is brought into contact with the micro-contact structure. To accomplish this, the user is prompted to use the micromanipulators on the test fixture in order to manually bring the force sensor into close, but not contact, proximity with the micro-contact structure. After the manual approach, the piezo actuator moves the sensor in steps set by the user before the start of the test until the force limit, also set by the user, is reached. The piezo actuator then moves the sensor away in 5 nm increments until a force less than 5 µN is read from the force sensor. The piezo actuator then moves the sensor towards the micro-contact structure until a force level greater than 5 µN is reached. The movement away and towards the micro-contact structure is repeated until a force of just less than 5 µN is measured on the last movement away from the micro-contact structure. The purpose of the back and forth movement is to verify contact with the micro-contact structure.
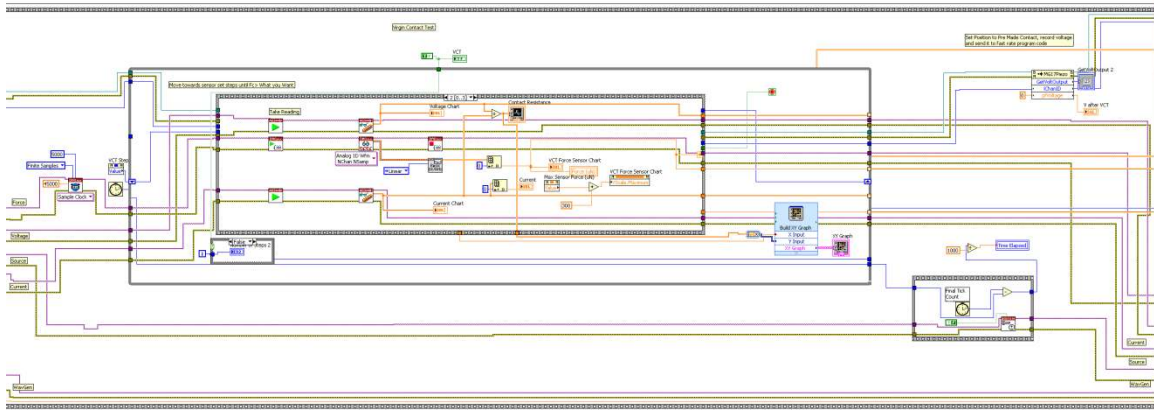
Figure 77 Frame 4 of the Graphical Programming for the Automated Data Acquisition System

At frame 4, the force sensor is now in contact with the micro-contact structure and the waveform information for the piezo controller is set. Also set in this frame are the voltage and current multimeters as well as the current source (if applicable).

Figure 78 Frame 5 of the Graphical Programming for the Automated Data Acquisition System

Frame 5 is where the piezo controller is set to closed loop mode for accurate position

control and the current source is turned on for the beginning of the VCT.

Figure 79 Frame 6 of the Graphical Programming for the Automated Data Acquisition System

Frame 6 is programmed to actually perform the VCT. In this frame, the force sensor is set to sample finite samples, then the piezo moves the sensor to actuate the micro-contact structure by increments set by the user. The system then waits at the incremental step for a period of time set by the user. Voltage, current, and force are read and displayed. The limits for contact force and maximum sensor force, which are set by the user, are checked. If the current measurement is greater than 700 nA then contact is considered to have been made. Once contact make has occurred, actual contact force is recorded. At this point, the VCT is complete and the position of the sensor is set back to its initial position.

138
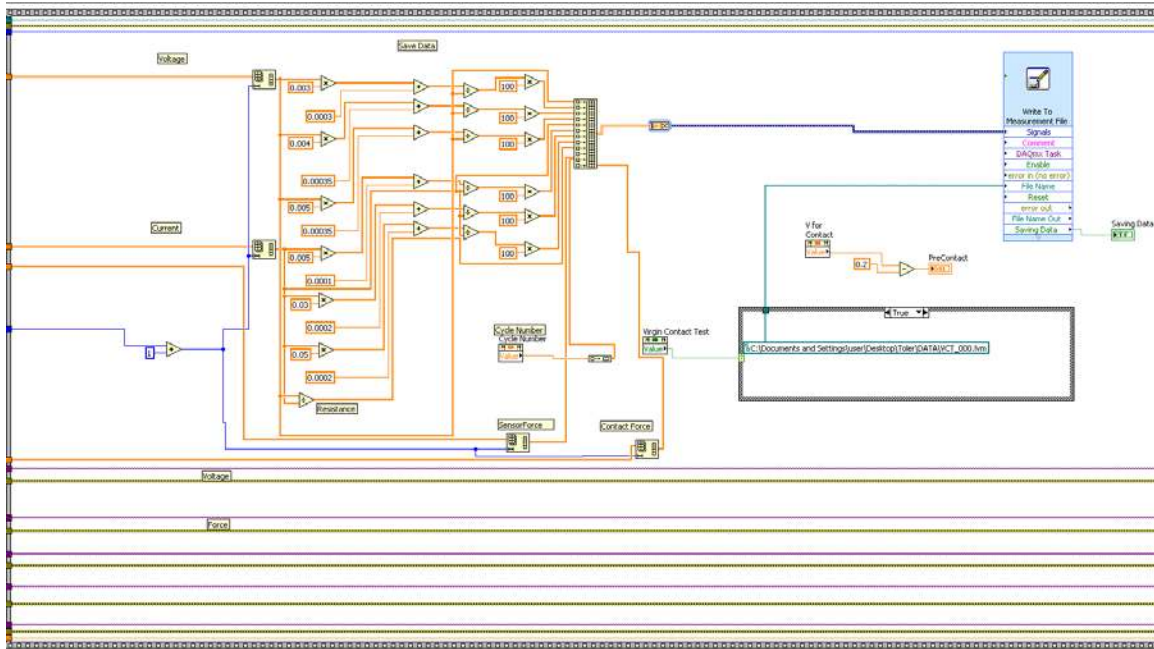
Figure 80 Frame 7 of the Graphical Programming for the Automated Data Acquisition System

In frame 7, the data from the VCT is recorded into an excel file. The data includes columns of voltage, current, resistance, sensor force, contact force, cycle number, and is placed in an excel file with a name designated for the test type being performed.
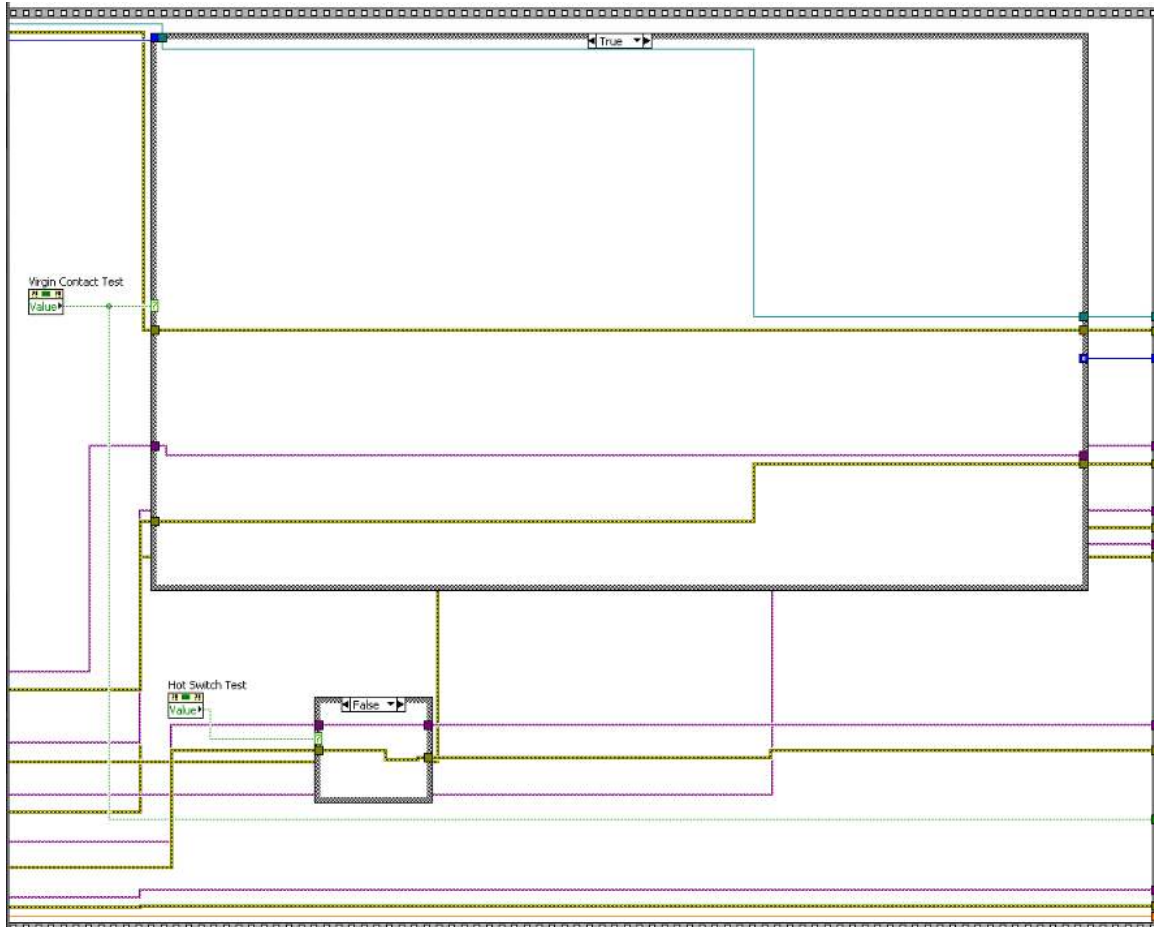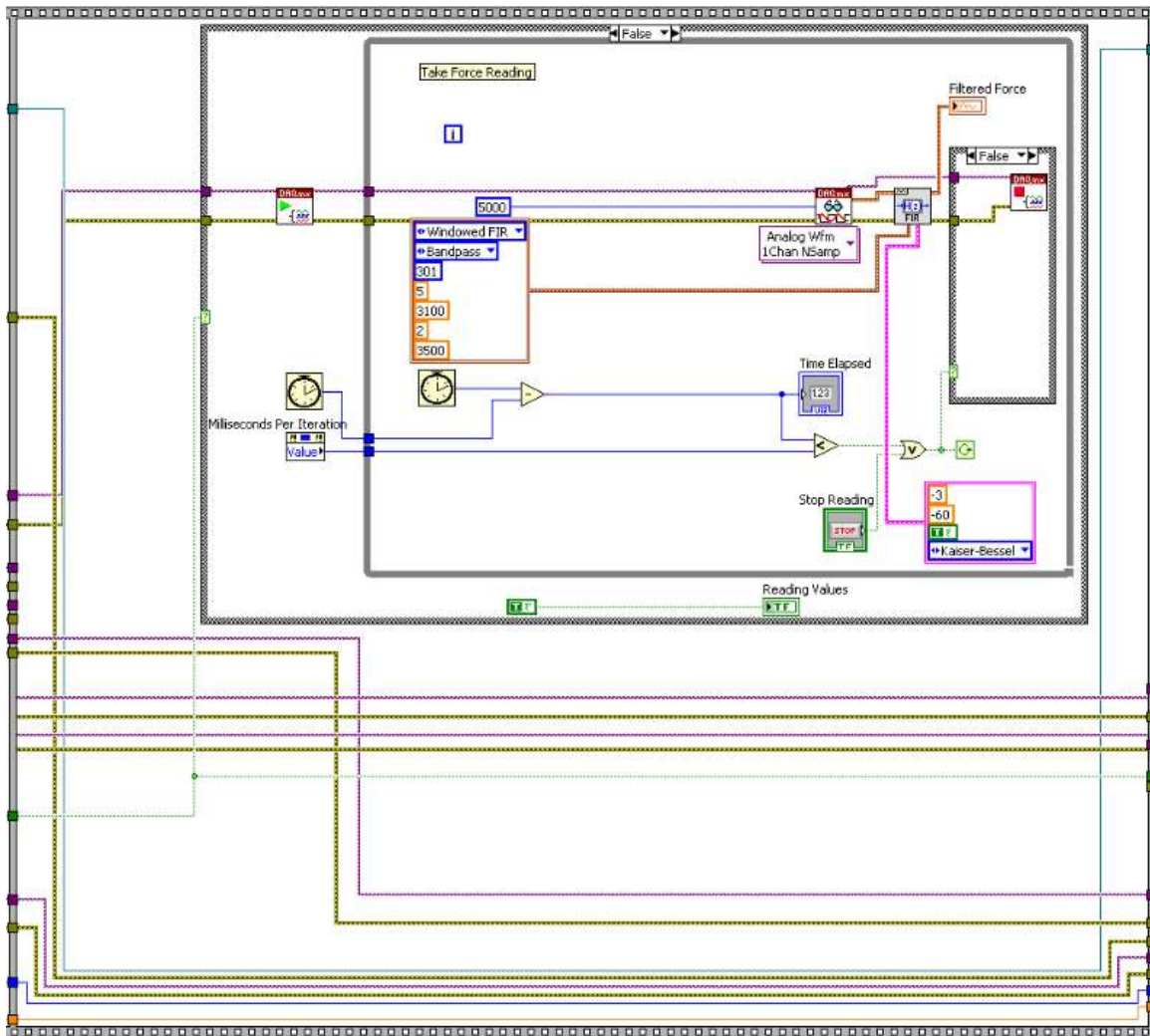
Figure 81 Frame 8 of the Graphical Programming for the Automated Data Acquisition System

Frame 8 is the programming responsible for the performance of a Hot or Cold test if applicable. The frame is skipped if the user has elected only to perform a VCT. In this frame, the current source is set and turned on for a Hot test or off for a Cold test. The piezo controller is then set to open loop mode in order to accommodate fast rate testing.
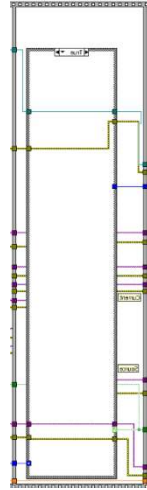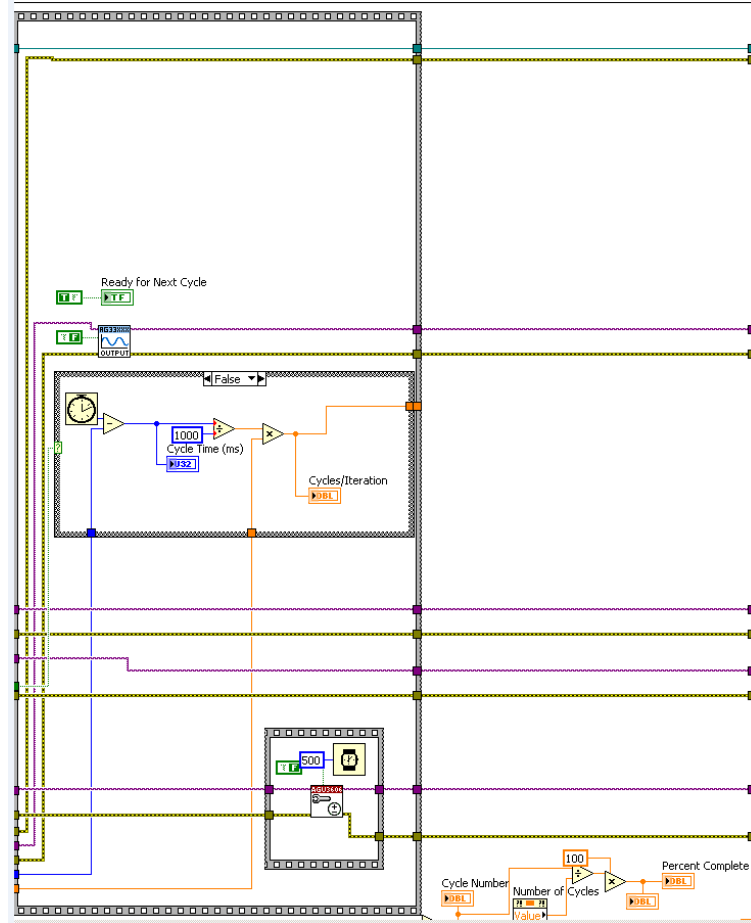
Figure 82 Frame 9 of the Graphical Programming for the Automated Data Acquisition System

Frame 9 contains the programming for applying the waveform chosen by the user to

the piezo controller. A conditional loop checks to see if the user desires a fast rate test and

skips the frame if false. Under the true condition, the frame applies the waveform.
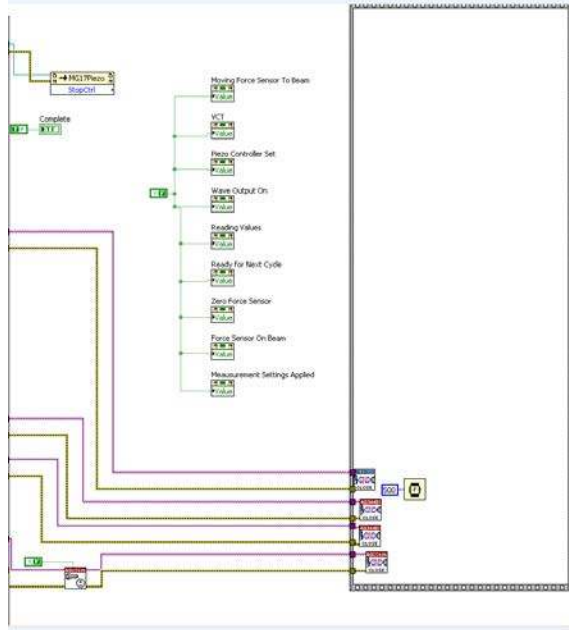
Figure 83 Frame 10 of the Graphical Programming for the Automated Data Acquisition System

The force sensor is set to continuous mode in order to display the force sensor readings on the user interface during a fast rate Cold or Hot test. Frame 10 filters the output of the force sensor appropriately to verify to the user that the desired waveform has been applied.

142

Figure 84 Frame 11 of the Graphical Programming for the Automated Data Acquisition System

In frame 11, the current source is turned off if needed and the cycle number is determined in order to check if the desired number of cycles have been performed. If the desired number of cycles have been performed then the for loop condition is complete and the program moves to frame 12. If the cycle count is below that of the set number, then the for loop iterates back to frame 5.

143

Figure 85 Frame 12 of the Graphical Programming for the Automated Data Acquisition System

Frame 12 contains the programming responsible for adjusting the progress indicators

and closing communications with the equipment used to perform the testing.

Appendix B: Functional Fixed-Fixed Micro-Contact Support Structure Data
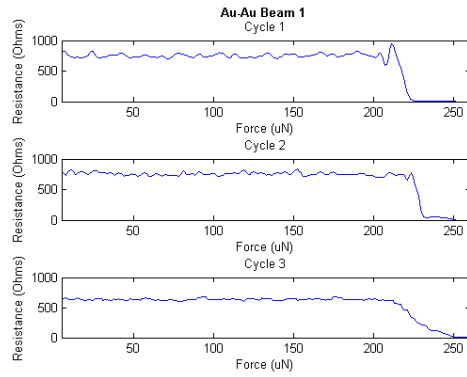

Figure 86 Au-Au Fixed-Fixed Micro-Contact Support Structure VCT Beam 1

Figure 87 Au-Au Fixed-Fixed Micro-Contact Support Structure VCT Beam 2

Figure 88 Au-Au Fixed-Fixed Micro-Contact Support Structure VCT Beam 3

Figure 89 Ag-Au Fixed-Fixed Micro-Contact Support Structure VCT Beam 1

Figure 90 Ag-Au Fixed-Fixed Micro-Contact Support Structure VCT Beam 2

Figure 91 Au-Au Fixed-Fixed Micro-Contact Support Structure CST Beam 1
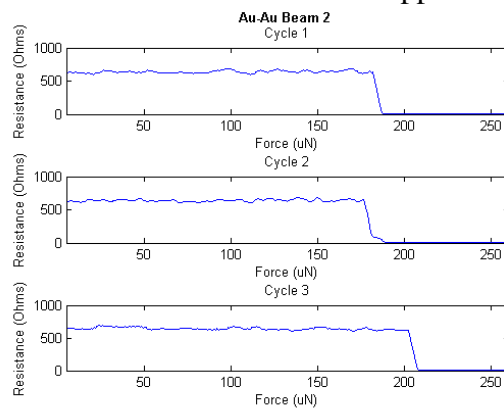
147

Au-Au Beam 2

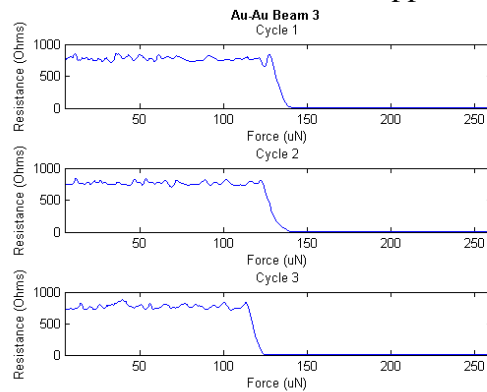Figure 92 Au-Au Fixed-Fixed Micro-Contact Support Structure CST Beam 2

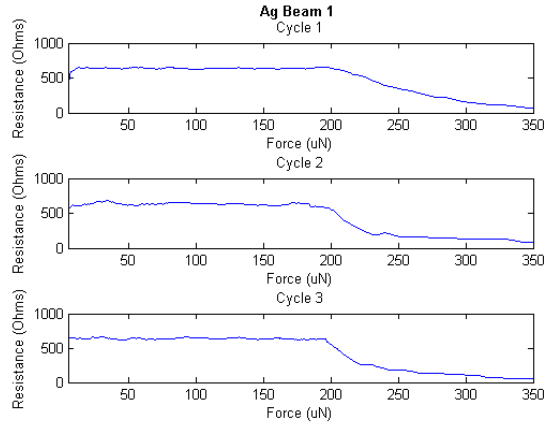Figure 93 Au-Au Fixed-Fixed Micro-Contact Support Structure CST Beam 3

149
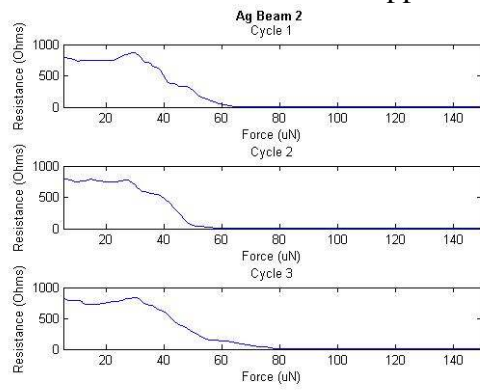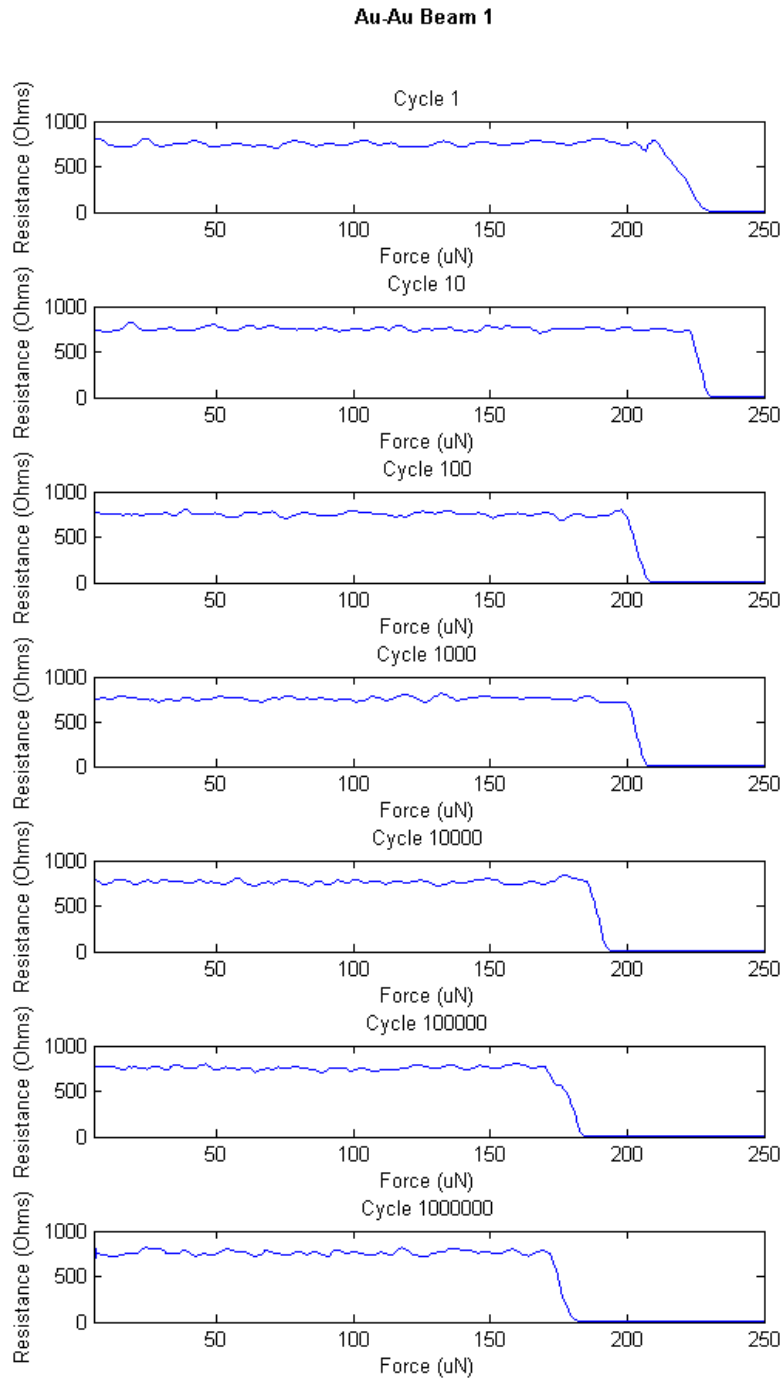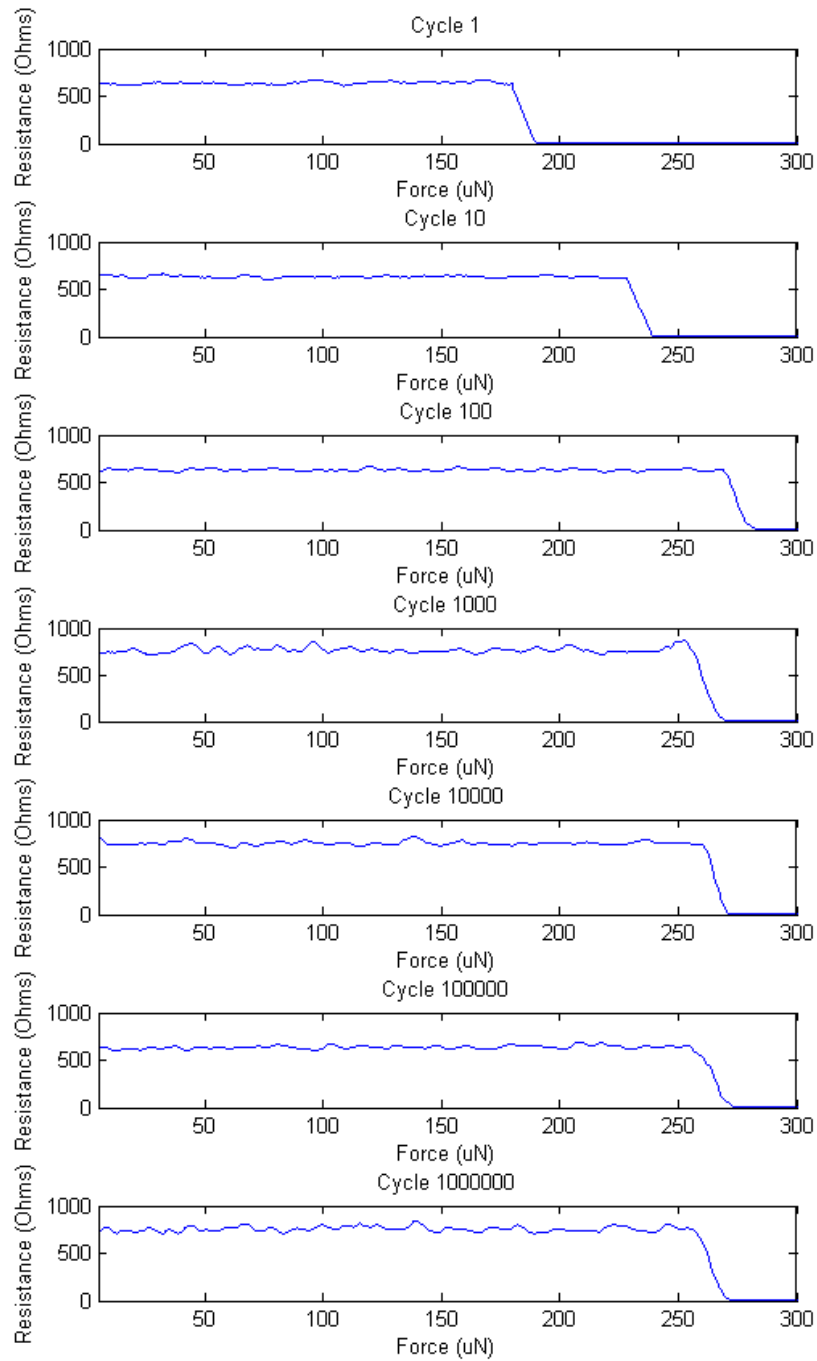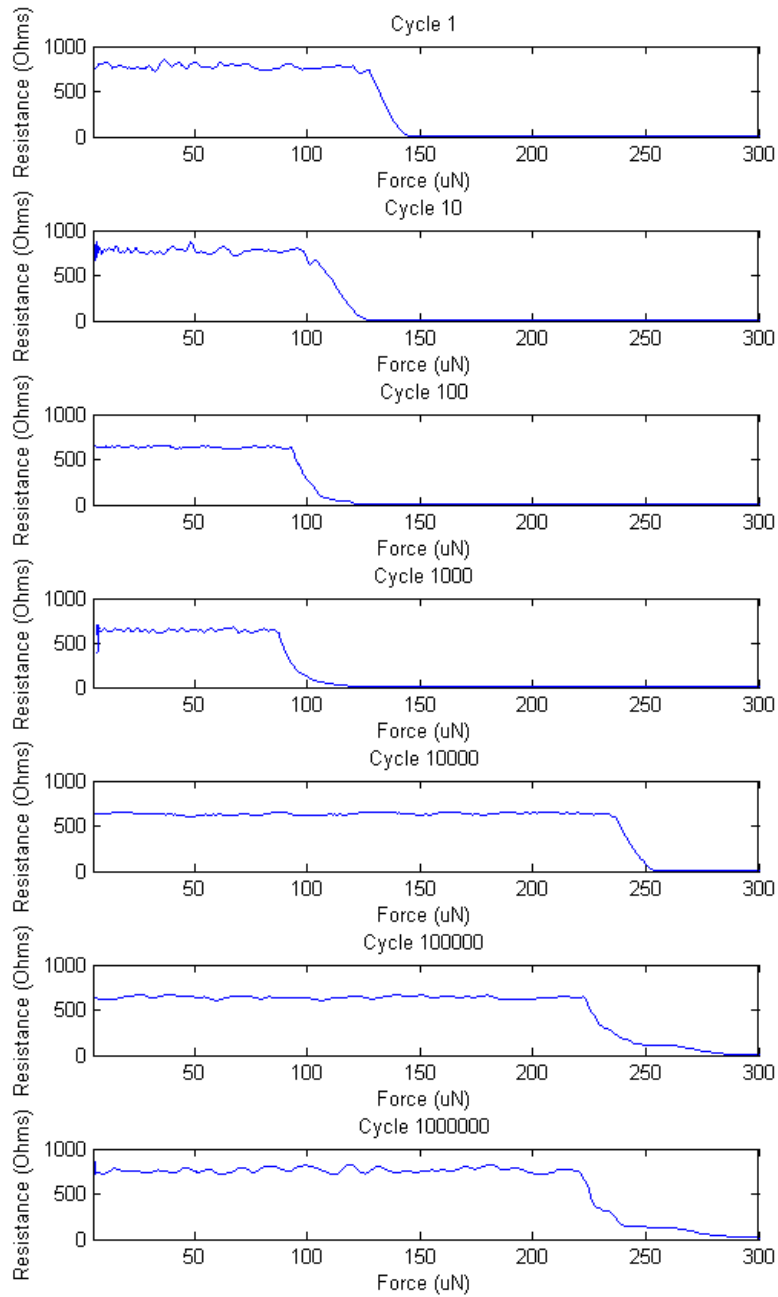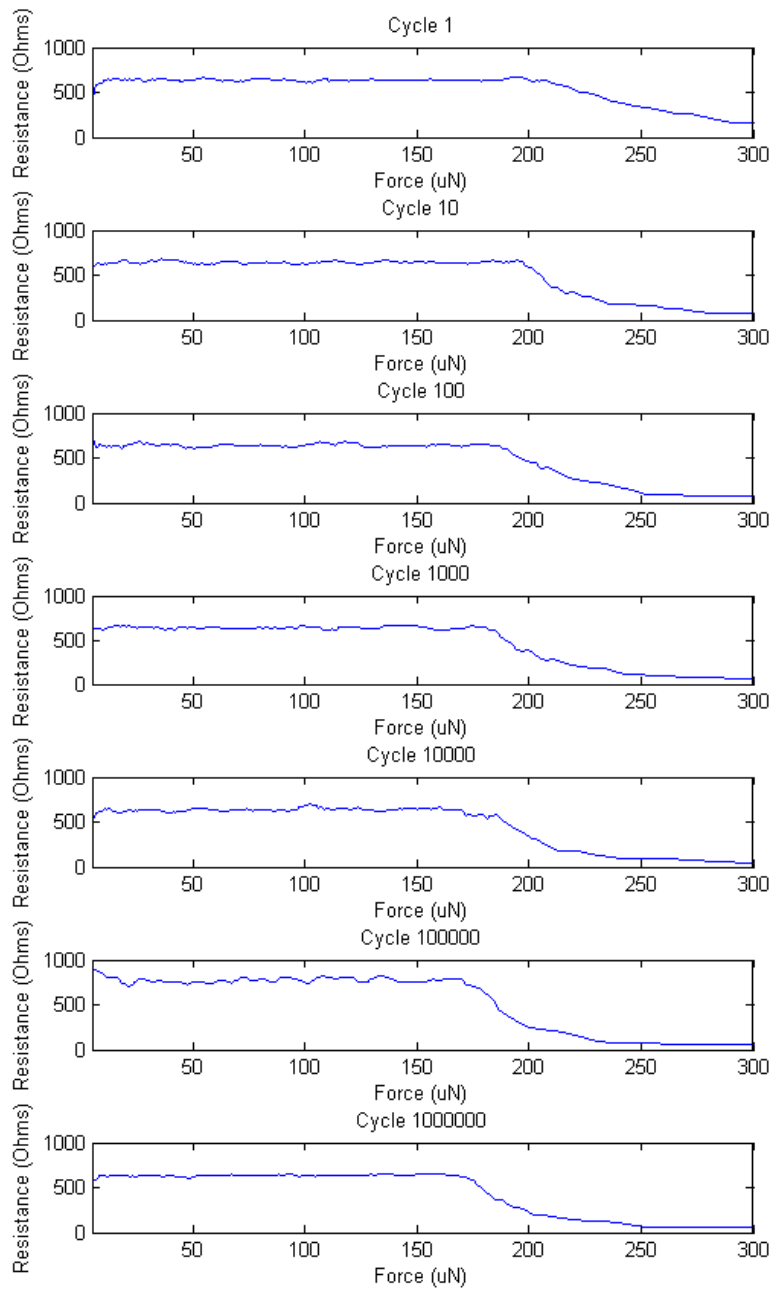
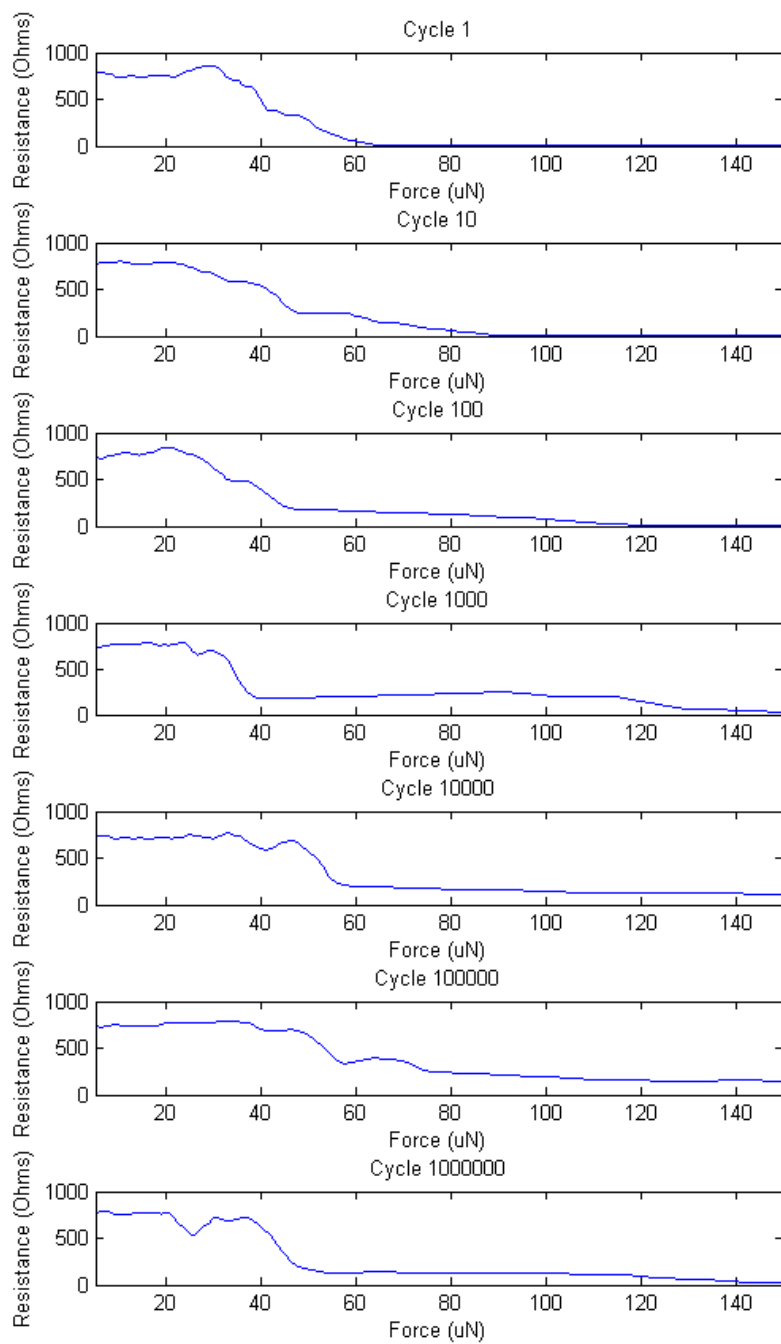Figure 94 Ag-Au Fixed-Fixed Micro-Contact Support Structure CST Beam 1

Figure 95 Ag-Au Fixed-Fixed Micro-Contact Support Structure CST Beam 2

Appendix C: Process Followers

Wafer **Wafer ID**	Purpose **µ-contacts**	Masks *Bottom Metal*	Process **Bottom Metal**	Print Date **2/16/2013**

Init.	Process Step	Notes	Date Time
	INSPECT WAFER: ☐ Note any defects	<u>Start Date</u> <u>Start Time</u>	
	SOLVENT CLEAN WAFER: ☐ 30 sec acetone rinse at 500 rpm ☐ 30 sec methanol rinse at 500 rpm ☐ 30 sec isopropyl alcohol rinse at 500 rpm ☐ 30 sec DI water rinse at 500 rpm ☐ Dry with nitrogen at 500 rpm ☐ Dry wafer with nitrogen on clean texwipes		
	DEHYDRATION BAKE: ☐ 1 min 110°C hot plate bake		
	SF-11 RESIST COAT: ☐ Flood wafer with SF-11 ☐ 30 sec spin at 4,000 rpm - Hold swab between wafer and Al foil during spin to capture excess photoresist which spins like 'cotton candy' ☐ 2 min 200°C hot plate bake		
	1805 COAT: ☐ Flood wafer with 1805 ☐ 4 sec spread at 500 rpm ☐ 30 sec spin at 4,000 rpm, ramp=200 ☐ 75 sec 110°C hot plate bake ☐ Use acetone to remove 1805 on backside		
	EXPOSE 1805 WITH Bottom Metal MASK #1: ☐ No alignment for first level mask needed, however mask should be straight ☐ 4.0 sec exposure using EVG 620; 4 sec exposure using MJB3		
	1805 DEVELOP: ☐ 40 sec develop with 351:DI (1:5), use a spin/stop/spin/stop method at 500 rpm ☐ 30 sec DI water rinse at 500 rpm ☐ Dry with nitrogen at 500 rpm ☐ Dry wafer with nitrogen on clean texwipes		
	INSPECT RESIST: ☐ Inspect photoresist under microscope, look for fringe patterns indicating residual SF-11		
	SF-11 EXPOSURE (~1.5 um / cycle): ☐ Place wafer in center of circle ☐ 300 sec DUV exposure with OAI DUV		
	SF-11 DEVELOP: ☐ 60 sec bucket develop with SAL 101 ☐ 30 sec DI rinse at 500 RPM or hold under DI faucet for 30 sec ☐ Dry with nitrogen at 500 RPM ☐ Dry wafer with nitrogen on clean texwipes		
	INSPECT RESIST: ☐ Inspect photoresist under microscope		
	TENCOR MEASUREMENT: ☐ Measure metal step height T_____ C_____ B_____		
	ASHER DESCUM ☐ 4 min, 75W, LFE Barrel Asher - Immediately before Evaporation		
	BOTTOM METAL DEPOSITION ☐ *Evaporate* 200 Å Ti / 2800 Å Au		

Process Step #1   Page 1

Init.	Process Step	Notes	Date Time
	LIFT-OFF METAL: ☐ Heat 1165 remover to 90°C (set hot plate to 170°C) ☐ Use packing tape to lift off *evaporated* Au/Ti ☐ 5 min ultrasonic bath in acetone ☐ 30 sec acetone rinse at 500 rpm ☐ 30 sec isopropyl alcohol rinse at 500 rpm ☐ 30 sec DI water rinse at 500 rpm ☐ Dry with nitrogen at 500 rpm ☐ 5 min soak in 1165 at 90° C ☐ 30 sec DI rinse at 500 rpm ☐ Dry wafer with nitrogen on clean texwipes		
	INSPECT METAL: ☐ Inspect metal under microscope		
	ASHER DE SCUM ☐ 4 min, 150W, LFE Barrel Asher		
	TENCOR MEASUREMENT: ☐ Measure metal step height T _____ C _____ B _____		
	Electrical Isolation Test: ☐ Verify electrical isolation between contact pads		

Wafer	Purpose	Masks	Process	Print Date
Wafer ID	μ-contacts	*Anchor/Bump*	**Anchor & Bump**	**2/16/2013**

Init.	Process Step	Notes	Date Time
	DEHYDRATION BAKE: ☐ 5 min 110°C hot plate bake	Start Date Start Time	
	FIRST SF-11 (PMGI) COAT: ☐ Flood wafer with SF-11 ☐ 30 sec spin at 4,000 rpm, ramp= 999, 5 sec spread=500 ☐ 2 min 200° hot plate bake		
	SECOND SF-11 (PMGI) COAT: ☐ Flood wafer with SF-11 ☐ 30 sec spin at 4,000 rpm ☐ 2 min 200° hot plate bake		
	1805 COAT: ☐ Flood wafer with 1805 ☐ 4 sec spread at 500 rpm ☐ 30 sec spin at 4,000 rpm, ramp=200 ☐ 75 sec 110°C hot plate bake ☐ Use acetone to remove 1805 on backside		
	EXPOSE 1805 WITH Anchor MASK #2: ☐ Align to bottom metal alignment marks ☐ 4.0 sec exposure using EVG 620; 4 sec exposure using MJB3		
	1805 DEVELOP: ☐ 40 sec develop with 351:DI (1:5), use a spin/stop/spin/stop method at 500 rpm ☐ 30 sec DI water rinse at 500 rpm ☐ Dry with nitrogen at 500 rpm ☐ Dry wafer with nitrogen on clean texwipes		
	INSPECT RESIST: ☐ Inspect photoresist under microscope		
	FIRST DUV EXPOSURE (~1.5 um / cycle): ☐ Place wafer in center of circle ☐ 200 sec DUV exposure with OAI DUV		
	SF-11 DEVELOP: ☐ 60 sec bucket develop with SAL 101 ☐ 30 sec DI rinse at 500 RPM ☐ Dry with nitrogen at 500 RPM ☐ Dry wafer with nitrogen on clean texwipes		
	INSPECT RESIST: ☐ Inspect photoresist under microscope, look for fringe patters indicating residual SF-11		
	SECOND DUV EXPOSURE (~1.5um / cycle): ☐ Place wafer in center of circle ☐ 200 sec DUV exposure with OAI DUV		
	SF-11 DEVELOP: ☐ 60 sec bucket develop with SAL 101 ☐ 30 sec DI rinse at 500 RPM ☐ Dry with nitrogen at 500 RPM ☐ Dry wafer with nitrogen on clean texwipes		
	INSPECT RESIST: ☐ Inspect photoresist under microscope, look for fringe patters indicating residual SF-11		
	TENCOR MEASUREMENT: ☐ Measure metal step height T _____ C _____ B _____		

154

Wafer **Wafer ID**	Purpose μ-contacts	Masks *Anchor/Bump*	Process **Anchor & Bump**	Print Date 2/16/2013	

Init.	Process Step	Notes	Date Time
	REMOVE 1805: □ ~12 sec acetone rinse at 500 rpm "As Needed" □ 30 sec methanol rinse at 500 rpm □ 30 sec isopropyl alcohol rinse at 500 rpm □ 30 sec DI rinse at 500 rpm □ Dry with nitrogen at 500 rpm □ Dry wafer with nitrogen on clean texwipes	When using Ace, the 1805 in the center of wafer will open up, immediately apply methanol to center and concurrently use ace to remove remaining 1805	
	INSPECT RESIST: □ Inspect photoresist under microscope		
	TENCOR MEASUREMENT: □ Measure metal step height T_____ C_____ B_____		
	1805 COAT: □ Flood wafer with 1805 □ 4 sec spread at 500 rpm □ 30 sec spin at 4,000 rpm, ramp=200 □ 75 sec 110°C hot plate bake □ Use acetone to remove 1805 on backside		
	EXPOSE 1805 WITH Contact Bump MASK #3: □ Align to bottom metal alignment marks □ 4 sec exposure using EVG 620; 4 sec exposure using MJB3		
	1805 DEVELOP: □ 40 sec develop with 351:DI (1:5), use a spin/stop/spin/stop method at 500 rpm □ 30 sec DI water rinse at 500 rpm □ Dry with nitrogen at 500 rpm □ Dry wafer with nitrogen on clean texwipes		
	INSPECT RESIST: □ Inspect photoresist under microscope		
	TENCOR MEASUREMENT: □ Measure metal step height T_____ C_____ B_____		
	PARTIAL DUV EXPOSURE (~0.7um BUMP DEPTH): □ 60 sec DUV exposure @ 35 mW/cm², 254 nm		
	SF-11 DEVELOP: □ 60 sec bucket develop with SAL 101 □ 30 sec DI rinse at 500 RPM □ Dry with nitrogen at 500 RPM □ Dry wafer with nitrogen on clean texwipes		
	INSPECT RESIST: □ Inspect photoresist under microscope		
	TENCOR MEASUREMENT: □ Measure metal step height T_____ C_____ B_____		

155

Init.	Process Step	Notes	Date Time
	REMOVE 1805: □ 30 sec acetone rinse at 500 rpm *DO NOT ALLOW acetone to dry on SF-11 □ 30 sec methanol rinse at 500 rpm □ 30 sec isopropyl alcohol rinse at 500 rpm □ 30 sec DI rinse at 500 rpm □ Dry with nitrogen at 500 rpm □ Dry wafer with nitrogen on clean texwipes		
	INSPECT RESIST: □ Inspect photoresist under microscope		
	TENCOR MEASUREMENT: □ Measure metal step height T_____ C_____ B_____		
	ASHER DESCUM □ 8 min, 75W, LFE Barrel Asher		
	TENCOR MEASUREMENT: □ Measure metal step height T_____ C_____ B_____		
	ANCHOR AND BUMP REFLOW & INSPECT WAFER: □ 90 sec 270°C hot plate bake **OR** □ 2-4 min 250°C hot air oven bake □ Inspect for resist reflow □ Reflow again if necessary		
	TENCOR MEASUREMENT: □ Measure metal step height T_____ C_____ B_____		

156

Wafer	Purpose	Masks	Process	Print Date
Wafer ID	µ-contacts	*Bridge Metal*	Bridge Metal & Release	2/16/2013

Init.	Process Step	Notes	Date Time
	ASHER DE SCUM: ☐ 4 min, 75W, LFE Barrel Asher	Start Date Start Time	
	SPUTTER CONTACT METAL LAYER: ☐ Sputter 2000 Å Au using Discovery-18		
	AZ3350 COAT: ☐ Flood wafer with AZ3350 ☐ 4 sec spread at 300 rpm ☐ 30 sec spin at 3,000 rpm, ramp=500 ☐ 5 min 110°C hot plate bake		
	EXPOSE AZ3350 WITH Bridge Metal MASK: ☐ Align to bottom metal alignment marks ☐ 7 sec exposure using EVG620;		
	AZ3350 DEVELOP: ☐ 60 sec develop with 300MIF, use a spin/stop/spin/stop method at 500 rpm ☐ 30 sec DI water rinse at 500 rpm ☐ Dry with nitrogen at 500 rpm ☐ Dry wafer with nitrogen on clean texwipes		
	INSPECT RESIST: ☐ Inspect photoresist under microscope		
	TENCOR MEASUREMENT: ☐ Measure metal step height T _____ C _____ B _____		
	SOLVENT BAKE: ☐ Bake in 90°C oven for 20 min		
	ASHER DE SCUM ☐ 4 min, 75W, LFE Barrel Asher		
	Electroplate BRIDGE METAL LAYER: ☐ Electroplate 2.4um Au using AFRL Electroplate Bath		
	TENCOR MEASUREMENT: ☐ Measure metal step height T _____ C _____ B _____		
	REMOVE AZ3350: ☐ 30 sec acetone rinse at 500 rpm ☐ 30 sec isopropyl alcohol rinse at 500 rpm ☐ 30 sec DI water rinse at 500 rpm ☐ Dry with nitrogen at 500 rpm ☐ Dry wafer with nitrogen on clean texwipes		
	ASHER DE SCUM ☐ 2 min, 75W, LFE Barrel Asher		
	CONTACT METAL ETCH: ☐ 40 sec Au Etchant, agitated ☐ 30 sec DI water rinse (stops the etching) ☐ Dry with nitrogen on clean texwipes		
	INSPECT CONTACT METAL: ☐ Make sure contact metal layer is completely removed		
	ASHER DE SCUM: ☐ 5 min, 150W, LFE Barrel Asher		

Process Step #3

Page 1

157

Init.	Process Step	Notes	Date Time
	STRIP SF-11 SACRIFICIAL LAYER (RELEASE PROCESS):		
	☐ Do NOT place devices in ultrasonic bath		
	☐ Place devices in 1165 at room temperature		
	☐ Heat 1165 remover to 90ºC (set hot plate to 120ºC)		
	☐ 35 min soak in 1165 at 90ºC		
	☐ Wet transfer from 1165 beaker to 1st IPA in petri dish, 30 sec soak		
	☐ Wet transfer to 2nd IPA in petri dish, 30 sec soak		
	☐ Wet transfer to 3rd IPA in petri dish, 30 sec soak		
	☐ Wet transfer to 4th IPA in petri dish, 30 sec soak		
	☐ Wet transfer to 1st methanol in petri dish, 30 sec soak		
	☐ Wet transfer to 2nd methanol in petri dish, 30 sec soak		
	☐ Wet transfer to 3rd methanol in petri dish, 30 sec soak		
	☐ Wet transfer to 4th methanol in petri dish, 30 sec soak		
	☐ Fill CO_2 dryer chamber with enough methanol to cover the wafer		
	☐ Remove wafer from 4th methanol dish and place in CO_2 dryer chamber		
	☐ Immediately cover CO_2 dryer and start process		
	ASHER DESCUM		
	☐ 15-30 min, 75W, LFE Barrel Asher		

Process Step #3

Bibliography

[1]   Rebeiz G, RF MEMS, theory, design, and technology, Hoboken: John Wiley and
        Sons, 2004.

[2]   Van Caekenberghe, K, "RF MEMS on the radar," *IEEE Microwave Magazine,* vol.
        10, no. 6, pp. 99-116, 2009.

[3]   Yang Z, Lichtenwalner D, Morris A, Krim J, Kingon A, "Comparison of Au and
        Au-Ni Alloys as Contact Materials for MEMS Switches," *IEEE Journal of
        Microelectromechanical Systems,* vol. 18, no. 2, pp. 287-295, 2009.

[4]   Dennard R, Cai J, Kumar A, "A perspective on today's scaling challenges and
        possible future directions," *Solid State Electronics,* vol. 51, no. 4, pp. 518-525,
        2007.

[5]   Kaynak M, Ehwald K, Sholz R, Korndorfer F, Wipf C, Sun Y, Tillack B, Zihir S,
        Gurbuz Y, "Characterization of an Embedded RF-MEMS Switch," in *Topical
        Meeting on Silicon Monolithic Integrated Circuits in RF Systems (SiRF)*, New
        Orleans, LA, pp. 144-147, 2010.

[6]   Zavracky P, Majumber S, McGruer N, "Micromechanical switches fabricated using
        nickel surface micromachining," *J. MEMS,* vol. 6, no. 1, pp. 3-9, 1997.

[7]   Yang Z, Lichtenwalner D, Morris A, Menzel S, Nauenheim C, Gruverman A, Krim
        J, Kingon A, "A new test facility for efficient evaluation of MEMS contact,"
        Journal of Micromechanics and Microengineering, vol. 17, pp. 1788-1795,
        2007.

[8]   Holm, R, Electric Contacts: Theory and Applications, Fourth Edition ed., Berlin:
        Springer, 1967.

[9]   Braunovic M, Konchits V, Myshkin N, Electrical Contacts- Fundamentals,
        Applications, and Technology, New York: CRC Press, 2007.

[10]   Coutu R, McBride J, Starman L, "Improved Micro-Contact Resistance Model that
        considers Material Deformation, Electron Transport and Thin Film
        Characteristics," in *Proc. 55th IEEE Holm Conference on Electrical Contacts*,

Vancouver, British Columbia, Canada, pp. 296-299, 2009.

[11] Greenwood J, Williamson J, "Contact of Nominally Flat Surfaces," *Proceedings of the Royal Society: Series A,* vol. 295, pp. 300-319, 1966.

[12] Majumder S, McGruer N, Adams G, Zavracky P, Morrison R, Krim J, "Study of contacts in an electrostatically actuated microswitch," *Sensors Actuators,* vol. 93, no. 1, pp. 19-26, 2001.

[13] Pitney K, Ney Contact Manual, Bloomfield: The J. M. Ney Company, 1973.

[14] Chang W, "An elastic-plastic model for a rough surface with an ion-plated soft metallic coating," *Journal of Wear,* vol. 212, pp. 229-237, 1997.

[15] Coutu R, Reid J, Cortez R, Strawser R, Kladitis P, "Microswitches with Sputtered Au, AuPd, Au-on-AuPt, and AuPtCu Alloy Electrical Contacts," *IEEE Transactions on Components and Packaging Technologies,* vol. 29, no. 2, pp. 341-349, 2006.

[16] Firestone F, Abbot E , "Specifying surface quantity - a method based on the accurate measurement and comparison," *ASME Mech. Eng,* vol. 55, p. 569, 1933.

[17] Edelmann T, Coutu R, Starman L, "Novel test fixture for collecting microswitch reliability data," in *Proceeding of SPIE, Photonics West: Reliability, Packaging, Testing and Characterization of MEMS/MOEMS and Nanodevices IX*, San Diego, CA, 2010.

[18] Wexler G, "The size effect and the non-local Boltzmann transport equation in orifice and disk geometry," *Proc. Phys. Soc.,* vol. 89, pp. 927-941, 1966.

[19] Timsit, R, "Constriction Resistance of Thin Film Contacts," *IEEE Transactions on Components and Packaging Technologies,* vol. 33, no. 3, pp. 636-642, 2010.

[20] Karmalkar S, Mohan P, Kumar B, "A Unified Compact Model of Electrical and Thermal 3-D Spreading Resistance Between Eccentric Rectangular and Circular Contacts," *IEEE Electron Device Letter,* vol. 26, no. 12, pp. 909-912, 2005.

[21] Dickrell D, Dugger M, "Electrical Contact Resistance Degradation of a Hot-Switched Simulated Metal MEMS Contact," *IEEE Transactions on Components and Packaging Technologies,* vol. 30, no. 1, pp. 75-80, 2007.

[22] Patton S, Eapen K, Zabinski J, "Effects of adsorbed water and sample aging in are on uN level adhesion force between Si(100) and silicon nitride," *Tribology International,* vol. 34, pp. 481-491, 2001.

[23] Lumbantobing A, Kogut L, Komvopoulos K, "Electrical Contact Resistance as a Diagnostic Tool for MEMS Contact Interfaces," *Journal of Microelectromechanical Systems,* vol. 13, no. 6, pp. 977-987, 2004.

[24] Sawada S., Tsukiji S, et al, "Current Density Analysis of Thin Film Effect in Contact Area on LED wafer," in *Proc. 58th IEEE Holm Conference on Electrical Contacts*, pp. 242-247, 2012.

[25] Norberg G, Dejanovic S, HesselBom H, "Contact resistance of thin metal film contacts," *IEEE Transactions Components Packaging Technology,* vol. 29, no. 2, pp. 371-378, 2006.

[26] Timsit R, "Electrical Conduction Through Small Contact Spots," *IEEE Transactions on Components and Packaging Technologies,* vol. 29, no. 4, pp. 727-734, 2006.

[27] Agrait N, Yeyati A, Ruitenbeek J, "Quantum Properties of atom-sized conductors," *Physics Reports,* vol. 377, pp. 81-279, 2003.

[28] Jackson R, Crandall E, et al, "An Analysis of Scale Dependent and Quantum Effects on Electrical Contact Resistance between Rough Surfaces," in *Proc. 58th IEEE Holm Conference on Electrical Contacts*, pp. 1-8 2012.

[29] Poulain C, Jourdan G, Peschot A, Mandrillon V, "Contact conductance quantization in a MEMS switch," in *Proceedings of the 56th IEEE Holm Conference on Electrical Contacts*, pg. 1-7, 2010.

[30] Pennec F, Peyrou D, Leray D, Pons P, Plana R, Courtade F, "Impact of the Surface Roughness Description on the Electrical Contact Resistance of Ohmic," *IEEE Transactions on Components, Packaging and Manufacturing Technology,* vol. 2, no. 1, pp. 85-94, 2012.

[31] McCool J, "Comparison of models for the contact of rough surfaces," *Wear,* vol. 107, no. 1, pp. 37-60, 1986.

[32] Majumdar A, Bhushan B, "Role of fractal geometry in roughness characterization and contact mechanics of surfaces," *ASME Journal of Tribology,* vol. 112, no. 2, pp. 205-216, 1990.

[33] Majumdar A, Tien C, "Fractal characterization and simulation of rough surfaces," *Wear,* vol. 136, no. 2, pp. 313-327, 1990.

[34] Kogut L, Jackson R, "A comparison of contact modeling utilizing statistical and fractal approaches," *ASME Journal of Tribology,* vol. 128, no. 1, pp. 213-217, 2005.

[35] Kogut L, Etsion I, "A finite element based elastic-plastic model for the contact of rough surfaces," *Tribology Transactions,* vol. 46, no. 3, pp. 383-390, 2003.

[36] Greenwood J, , "A Unified Theory of Surface Roughness," *Proceedings of The Royal Society A,* vol. 393, pp. 133-157, 1984.

[37] Rezvanian O, Zikry M, Brown C, Krim J, "Surface roughness, asperity contact and gold RF MEMS switch behavior," *Journal of Micromechanics and microengineering,* vol. 17, pp. 2006-2015, 2007.

[38] Borri-Brunetto M, Chiaia B, Ciavarella M, "Incipient sliding of rough surfaces in contact: a multiscale numerical analysis," *Computer Methods in Applied Mechanics and Engineering,* vol. 190, no. 46/47, pp. 6053-6073, 2001.

[39] Komvopoulos K, Ye N, "Three-dimensional contact analysis of elastic-plastic layered media with fractal surface topographies," *ASME Journal of Tribology,* vol. 123, no. 3, pp. 632-640, 2001.

[40] Persson B, Bucher F, Chiaia B, "Elastic contact between randomly rough surfaces: comparison of theory with numerical results," *Physical Review B,* vol. 65, pp. 184106-184111, 2002.

[41] Persson B, "Elastoplastic contact between randomly rough surfaces," *Physical Review Letters,* vol. 87, no. 11, p. 116101, 2001.

[42] Jackson R, Streator J, "A multi-scale model for contact between rough surfaces," *Wear,* vol. 261, pp. 1337-1347, 2006.

[43] Wilson W, Angadi S, Jackson R, "Electrical Contact Resistance Considering Multi-Scale Roughness," in *Proc. 54th IEEE Holm Conference on Electrical Contacts*, pp. 190-197, 2008.

[44] Jackson R, "A model for the adhesion of multiscale rough surfaces in MEMS," in *System Theory (SSST), 2011 IEEE 43rd Southeastern Symposium on*, 2011.

[45] Jackson R, Kogut L, "Electrical Contact Resistance Theory for Anistropic Conductive Films Considering Electron Tunneling and Particle Flattening," *IEEE Transactions on Components and Packaging Technologies,* vol. 30, no. 1, pp. 59-66, 2007.

[46] Coutu R, Kladitis P, Leedy K, Crane R, "Selecting metal allow electric contact materials for MEMS switches," *Journal for Micromechanical Microengineering,* no. 14, pp. 1157-1164, 2004.

[47] Broue A, Dhennin J, Charvet P, Pons P, Jemaa N, Heeb P, Coccetti F, Plana R, "Multi-physical characterization of micro-contact materials for MEMS switches," in *Proc. 56th IEEE Holm Conference on Electrical Contacts*, pp. 363-372, 2010.

[48] Gere J, Timoshenko S, Thornes S, Mechanics of Materials (Fourth SI Edition), Nelson Thornes, 1999.

[49] Shigley, J and Mischke C, Mechanical engineering Design, New York: McGraw-Hill, Inc., 1990.

[50] Cowen A, Hardy B, Mahadevan R, Wilcenski S, "PolyMUMPs Design Handbook," MEMSCAP Inc., Revision 13.0.

[51] Jaafar H, "Design and simulaiton of high performance RF MEMS series switch," in *2011 IEEE Regional Symposium on Micro and Nanoelectronics (RSM)*, Serdang, Malaysia, 2011.

[52] Kaajakari V, Practical MEMS, Las Vegas, Nevada: small gear publishing, 2009.

[53] Kovacs, G, Micromachined Transducers Sourcebook, New York: McGraw-Hill, 1998.

[54] Comtois J, Michalicek M, Barron C, "Fabricating Micro-Instruments in Surface-Micromachined Polycrystalline Silicon," in *Proceedings of the 43rd International Instrumentation Symposium*, 1997.

[55] Lucyszyn S, "Review of radio frequency microelectromechanical systems technology," in *Science, Measurement and Technology, IEE Proceedings*, London, 2004.

[56] Kim J, Lee S, Baek C, Kwon Y, Kim Y, "Cold and hot switching lifetime characterizations of ohmic contact RF MEMS switches," *IEICE Electronics Express,* vol. 5, no. 11, pp. 418-423, 2008.

[57] American Society for Metals, "Metals Handbook," *ASM International,* vol. 2, 1990.

[58] Arrazat B, Duvivier P, Mandrillon V, Inal K, "Discrete Analysis of Gold Surface Apserities Deformation under Spherical Nano-Indentation Towards Electrical Contact Resistance Calculation," in *Proc. IEEE 57th Holm Conference on Electrical Contacts*, pp. 167-174, 2011.

[59] Broue A, Dhennin J, Courtade F, Dieppedale C, Pons P, Lafontan X, Plana R, "Characterization of Au/Au, Au/Ru and Ru/Ru ohmic contacts in MEMS switches improved by a novel methodology," *Journal of Micro/Nanolithography, MEMS, and MOEMS,* vol. 9, no. 4, pp. 041102-1 - 041102-8, 2010.

[60] McGreuer N, Adams G, Chen L, Guo Z, Du Y, "Mechanical, thermal, and material influences on ohmic-contact-type MEMS switch operation," in *Proc. 19th MEMS* , Istanbul, Turkey, 2009.

[61] Kwon H, Choi D, Park J, Lee H, Kim Y, Nam H, Joo Y, Bu J, "Contact materials and reliability for high power RF-MEMS switches," in *IEEE 20th International Conference on Micro Electro Mechanical Systems, 2007*, 2007.

[62] Yaglioglu O, Hart A, Martens R, Slocum A, "Method of characterizing electrical contact properties of carbon nanotube coated surfaces," *Rev. Scie Instrum.,* vol. 77, pp. 095105/1 - 095105/3, 2006.

164

[63] Thostenson E, Ren, Chou T, "Advances in the science and technology of carbon nanotubes and their composits: A review," *Composites Sci. Technology,* vol. 61, pp. 1899-1912, 2001.

[64] Yunus E, McBride J, Spearing S, "The Relationship Between Contact Resistance and Contact Force on Au-Coated Carbon Nanotube Surfaces Under Low Force Conditions," *IEEE Transactions on Components and Packaging Technologies,* vol. 32, no. 3, pp. 650-657, 2009.

[65] Choi J, Lee J, Eun Y, Kim M, Kim J, "Microswitch with self-assembled carbon nanotube arrays for high current density and reliable contact," in *IEEE 24th International Conference on Micro Electro Mechanical Systems (MEMS),* 2011.

[66] Chai Y, Hazeghi A, Takei K, Chen H, Chan P, Javey A, Wong H, "Low-Resistance Electrical Contact to Carbon Nanotubes with Graphitic Interfacial Layer," *IEEE Transactions on Electron Devices,* vol. 59, no. 1, pp. 12-19, 2012.

[67] Gambino J, Colgan E, "Silicides and ohmic contacts," *Materials Chemistry and Physics,* vol. 52, no. 2, pp. 99-146, 1998.

[68] Kim W, Javey A, Tu R, Cao J, Wang Q, Dai H, "Electrical contacts to carbon nanotubes down to 1nm in diameter," *Applied Physics Letters,* vol. 87, no. 17, pp. 101-173, 2005.

[69] Chai Y, Hazeghi A, Takei K, Chen Y, Chan P, Javey A, Wong H, "Graphitic interfacial layer to carbon nanotube for low electrical contact resistance," *IEDM Technology Digest,* pp. 210-213, 2010.

[70] Chen Q, Wang S, Peng L, "Establishing Ohmic contacts for in situ current-voltage characteristic measurements on a carbon nanotube inside the scanning electron microscope," *Nanotechnology,* vol. 17, no. 4, pp. 1087-1098, 2006.

[71] Rykaczewski K, Henry M, Kim S, Fedorov A, Kulkarni D, Singamaneni S, Tsukruk V, "The effect of geometry and material properties of a carbon joint produced by electron beam induced deposition on the elctrical resistance of a multiwalled carbon nanotube-to-metal contact interface," *Nanotechnology,* vol. 21, no. 3, pp. 1-12, 2010.

[72] Ke F, Miao J, Oberhammer J, "A Ruthenium-Based Multimetal-Contact RF MEMS Switch with a corrugated diaphragm," *Journal of Microelectromechanical systems,* vol. 17, no. 6, pp. 1447-1459, 2008.

[73] Lee H, Coutu R, Mall S, Leedy K, "Characterization of metal and metal alloy films as contact materials for MEMS switches," *Journal of Micromechanical and Microengineering,* vol. 16, pp. 557-563, 2006.

[74] Cha P, Srolovitz D, Vanderlick T, "Molecular Dynamics Simulation of Single Asperity Contact," *Acta Materialia,* vol. 52, pp. 3983-3996, 2004.

[75] Song J, Srolovitz D, "Atomistic Simulation of Multi-cycle Asperity Contact," *Acta Materialia,* vol. 55, p. 14, 2007.

[76] Kuipers L, Frenken J, "Jump to contact, neck formation, and surface melting in the scanning tunneling microscope," *Physcial Review Letters,* vol. 70, no. 25, pp. 3907-3910, 1993.

[77] Patton S, Zabinski J, "Fundamental studies of Au contacts in MEMS RF switches," *Tribology Letters,* vol. 18, pp. 215-230, 2005.

[78] Fortini A, Mendelev M, Buldyrev S, Srolovitz D, "Asperity contacts at the nanoscale: comparison of Ru and Au," *Journal of Applied Physics,* vol. 104, no. 7, pp. 074320.1-074320.8, 2008.

[79] Frenkel D, Smit B, Understanidng Molecular Simulation 2nd edition vol.1 of Computational Science Series, New York: Academic Press, 2002.

[80] Sorensen M, Brandbyge M, Jacobsen K, "Mechanical deformation of atomic-scale metallic contacts: Structure and mechanisms," *Physics Review B: condensed matter and materials physics,* vol. 57, no. 6, pp. 3283-3294, 1998.

[81] Du Y, Chen L, McGruer N, Adams G, Etsion I, "A finite element model of loading and unloading of an asperity contact with adhesion and plasticity," *Journal of Colloid and Interface Science,* vol. 312, no. 2, pp. 522-528, 2007.

[82] Chen Y, Nathanael R, Jeon J, Yaung J, Hutin L, Liu T, "Characterization of Contact Resistance Stability in MEM Relays With Tungsten Electrodes,"

Journal of Microelectromechanical Systems, vol. PP, no. 99, pp. 1-3, 2012.

[83]   Kam H, Pott V, Nathanael R, Jeon J, Alon E, Liu T, "Design and reliability of a micro-relay technology for zero-standby-power digital logic applications," *IEDM Technical Digest,* pp. 809-811, 2009.

[84]   Deal B, Grove A, "General relationship for the thermal oxidation of silicon," *Journal of Applied Physics,* vol. 36, no. 12, pp. 3770-3778, 1965.

[85]   Spencer M, Chen F, Wang C, Nathanael, Fariborzi H, Gupta A, Kam H, Pott V, Jeon J, Liu T, Markovic D, Alon E, Stojanovic V, "Demonstration of integrated micro-electro-mechanical relay circuits for VLSI applications," *IEEE Journal of Solid-State Circuits,* vol. 46, no. 1, pp. 308-320, 2011.

[86]   Chandler R, Park W, Li H, Yama G, Partridge A, Lutz M, Kenny T, "Single wafter encapsulation of MEMS devices," *IEEE Transactions Advance Packaging,* vol. 26, no. 3, pp. 227-232, 2003.

[87]   Yamashita T, Itoh T, Suga T, "Investigation of anti-stiction coating for ohmic contact MEMS switches with thiophenol and 2-naphtalenethiol self-assembled monolayer," *Sensors and Actuators A: Physical,* vol. 172, no. 2, pp. 455-461, 2011.

[88]   Tang W, Xu K, Wang P, Li X, "Surface roughness and resistivity of Au film on Si-(111) substrate," *Microelectronics Engineering,* vol. 66, pp. 445-450, 2003.

[89]   Hyman D, Mehregany M, "Contact physics of gold microcontacts for MEMS switches," *IEEE Transactions on Components and Packaging Technologies,* vol. 22, no. 3, pp. 357-564, 1999.

[90]   Kataoka K, Itoh T, Suga T, "Characterization of fritting phenomena on Al electrode for low contact force probe card," *IEEE Transactions on Components and Packaging and Technology,* vol. 26, pp. 382-387, 2003.

[91]   Baek S, Fearing R, "Reducing Contact Resistance Using Compliant Nickel Nanowire Arrays," *IEEE Transactions on Components and Packaging Technologies,* vol. 31, no. 4, pp. 859-868, 2008.

[92] Myers M, Leidner M, et al, "Contact Resistance Reduction by Matching Current and Mechanical Load Carrying Asperity Junctions," in *Proc. 58th IEEE Holm Conference on Electrical Contacts*, pp. 248-251, 2012.

[93] Jemaa, N, "Short arc duration laws and distributions at low current(<1A) and voltage (14-42Vdc)," *IEEE Transactions on Components, Packaging, and Technology,* vol. 24, no. 3, pp. 358-363, 2001.

[94] Jemaa N, "Contacts conduction and switching in DC levels," in *Proceedings of the 48th IEEE Holm Conference on Electrical Contacts*, 2002.

[95] Hasegawa M, Kamada Y, "An experimental study on re-interpretation of minimum arc current of electrical contacts," *IEICE Transactions on Electronics,* vol. 8, no. E88-C, pp. 1616-1619, 2005.

[96] Johler W, "Basic investigations for switching of RF signals," in *Proceedings of 53rd IEEE Holm Conference on Electrical Contacts*, 2007.

[97] Miki N, Sawa K, "Arc extinction characteristics in power supply frequencies from 50Hz to 1Mhz," in *Proceedings of 24th International Conference on Electrica Contact Phenomena*, 2008.

[98] Peschot A, Poulain C, et al, "Contact Bounce Phenomena in a MEM Switch," in *Proc. 58th IEEE Holm Conference on Electrical Contacts*, pp. 49- 55, 2012.

[99] Maboudian R, Howe R, "Critical review: Adhesion in surface micromechanical structures," *Journal of Vacuum Science & Technology B,* vol. 15, no. 1, pp. 1-20, 1997.

[100] McCarthy B, Adams G, McGruer N, Potter D, "A Dynamic Model, Including Contact Bounce, of an Electrostatically Actuated Microswitch," *Journal of Microelectromechanical Systems,* vol. 11, no. 3, pp. 276-283, 2002.

[101] Majumder S, Lampen J, Morrison R, Maciel J, "MEMS Switches," *IEEE Instrum. Meas. Mag.,* vol. 6, no. 1, pp. 12-15, 2003.

[102] Newman H, Ebel J, Judy D, Maciel J, "Lifetime Measurements on a High-Reliability RF-MEMS Contact Switch," *IEEE Microwave and Wireless*

Components Letters , vol. 2, pp. 100-102, 2008.

[103] McBride J, "The wear processes of gold coated multi-walled carbon nanotube surfaces used as electrical contact for micro-mechanical switching," *Nanoscience and Nanotechnology Letters,* vol. 4, no. 2, pp. 357-361, 2010.

[104] Toler B, Coutu R, "Characterizing External Resistive, Inductive and Capacitive Loads for Micro-Switches," *MEMS and Nanotechnology, Volume 6,* vol. 42, pp. 11-18, 2013.

[105] Mercado L, Kuo S, Lee T, Liu L, "Mechanism-based solutions to RF MEMS switch stiction problem," *IEEE Transactions Components and Packaging Technologies,* vol. 27, pp. 560-570, 2004.

[106] Peroulis D, Pacheco S, Sarabandi K, Katehi L, "Electromechanical considerations in developing low-voltage RF MEMS switches," *IEEE Transactions on Microwave Theory Technologies,* vol. 51, pp. 259-270, 2003.

[107] Park J, Shim E, Choi W, Kim Y, Kwon Y, Cho D, "A non-contact-type RF MEMS switch for 24-GHz radar applications," *Journal of Microelectromechanical Systems,* vol. 18, pp. 163-173, 2009.

[108] Brown C, Morris A, Kingon A, Krim J, "Cyrogenic performance of RF MEMS switch contats," *Journal of Microelectromechanical Systems,* vol. 17, pp. 1460-1467, 2008.

[109] Prokopovich P, Perni Stefano, "Comparison of JKR and DMT based multi-asperity adhesion model: Theory and experiment," *Colloids and Surfaces A: Physicochemical and Engineering Aspects,* vol. 383, no. 1-3, pp. 95-101, 2011.

[110] Wu L, Noels L, Rochus V, Pustan M, Golinval J, "A Micro-Macro approach to predict stiction due to surface contact in microelectromechanical systems," *Journal of microelectromechanical systems,* vol. 20, no. 4, pp. 976-990, 2011.

[111] Nikolic B, Allen P, "Electron transport through a circular constriction," *Physical Review B,* vol. 60, pp. 3963-3969, 1999.

[112] Gregori G, Clarke D, "The interrelation between adhesion, contact creep, and roughness on the life of gold contacts in radio-frequency microswitches,"

Journal of Applied Physics, vol. 100, no. 9, p. 094904, 2006.

[113] Budakian R, Putterman S, "Time scales for cold welding and the origins of stick-slip friction," *Physical Review B,* vol. 65, p. 235429, 2002.

[114] Kruglick E, Pister K, "Lateral MEMS microcontact considerations," *Journal of Micromechanical Systems,* vol. 8, no. 3, pp. 264-271, 1999.

[115] Sun M, Pecht M, Natishan M, Martens R, "Lifetime resistance model of bare metal electrical contacts," *IEEE Transactions on Advanced Packaging,* vol. 22, no. 1, pp. 60-67, 1999.

[116] Takano E, Mano K, "Theoretical lifetime of static contacts," *IEEE Transactions on Parts, Materials, and Packaging,* vol. 22, no. 1, pp. 60-67, 1967.

[117] Poulain C, Peschot A, Vincent M, Bonifaci N, "A Nano-Scale Investigation of Material Transfer Phenomena at Make in a MEMS Switch," in *2011 IEEE 57th Holm Conference on Electrical Contacts*, Grenoble, France, 2011.

[118] Klein S, Thilmont S, Ziegler V, Prechtel U, Schmid U, Seidel H, "High temperature stable RF MEMS switch based on tungsten-titanium," in *Solid-State Sensors, Actuators and Microsystems Conference, 2009. TRANSDUCERS 2009. International*, 2009.

[119] Crossland W, Murphy P, "The formation of insulating organic films on palladium-silver contact alloys," *IEEE Transactions on Parts, Hybrids and Packaging,* vol. 10, no. 1, pp. 64-69, 1974.

[120] Volinsky A, Moody N, Gerberich W, "Nanoindention of Au and Pt/Cu thin films at elevated temperatures," *J. Mater. Res.,* vol. 19, no. 9, pp. 2650-2657, 2004.

1. REPORT DATE (DD-MM-YYYY) 21-03-2013	2. REPORT TYPE Master's Thesis	3. DATES COVERED (From – To) Aug 2011 - Mar 2013

4. TITLE AND SUBTITLE Novel Test Fixture For Characterizing Microcontacts: Performance And Reliability	5a. CONTRACT NUMBER
	5b. GRANT NUMBER
	5c. PROGRAM ELEMENT NUMBER
6. AUTHOR(S) Toler, Benjamin F., 1st Lieutenant, USAF	5d. PROJECT NUMBER If sponsor, write JON# here, or N/A if no $$.
	5e. TASK NUMBER
	5f. WORK UNIT NUMBER

7. PERFORMING ORGANIZATION NAMES(S) AND ADDRESS(S) Air Force Institute of Technology Graduate School of Engineering and Management (AFIT/EN) 2950 Hobson Way, Building 640 WPAFB OH 45433	8. PERFORMING ORGANIZATION REPORT NUMBER AFIT-ENG-13-M-47
9. SPONSORING/MONITORING AGENCY NAME(S) AND ADDRESS(ES) Intentionally Left Blank	10. SPONSOR/MONITOR'S ACRONYM(S)
	11. SPONSOR/MONITOR'S REPORT NUMBER(S)

12. DISTRIBUTION/AVAILABILITY STATEMENT
DISTRUBUTION STATEMENT A. APPROVED FOR PUBLIC RELEASE; DISTRIBUTION UNLIMITED

13. SUPPLEMENTARY NOTES

14. ABSTRACT
Engineers have attempted to improve reliability and lifecycle performance using novel micro-contact metals, unique mechanical designs and packaging. Contact resistance can evolve over the lifetime of the micro-switch by increasing until failure. This work shows the fabrication of micro-contact support structures and test fixture which allow for micro-contact testing, with an emphasis on the fixture's design to allow the determination and analysis of the appropriate failure mode. The other effort of this investigation is the development of a micro-contact test fixture which can measure contact force and resistance directly and perform initial micro-contact characterization, and two forms of lifecycle testing for micro-contacts at rates up to 3kHz. In this work, two different designs of micro-contact structures are fabricated and tested, with each providing advantages for studying micro-contact physics. After fabrication was refined, three functioning fixed-fixed Au micro-contact support structures with contact radii of 4, 6, and 10 µm and two functioning fixed-fixed Ag micro-contacts were tested using the µN force sensor at cycle rates up to 3 kHz. Comparing the PolyMUMPs micro-contact support structure to the fixed-fixed micro-contact support structure, it was determined that the fixed-fixed micro-contact support structure is the best structure for studying the evolution of micro-contact resistance.

15. SUBJECT TERMS
 Micro-Contacts, Micro-Switches, Micro-Contact performance and reliability, contact evolution, micro-contact resistance

16. SECURITY CLASSIFICATION OF:			17. LIMITATION OF ABSTRACT	18. NUMBER OF PAGES	19a. NAME OF RESPONSIBLE PERSON Ronald A. Coutu, Jr., Ph.D., P.E.
a. REPORT U	b. ABSTRACT U	c. THIS PAGE U	UU	176	19b. TELEPHONE NUMBER (Include area code) (937) 255-6565, x 7230 (ronald.coutu@afit.edu)